

**SOLID STATE (CHEMICAL) SYNTHESIS  
AND ELECTRICAL CHARACTERIZATION  
OF ZINC OXIDE (ZnO) BASED  
ELECTRONIC CERAMIC SENSORS**

A Thesis Submitted to  
THE UNIVERSITY OF POONA

For The Degree of  
Doctor of Philosophy  
In Physics

By

**DINKAR KISANRAO KHARAT, M.Sc.**

Physical Chemistry Division  
National Chemical Laboratory  
Pune-411008 (INDIA)

JULY 1993

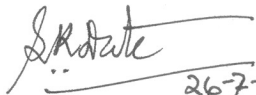
COMPUTERISED

CERTIFICATE

*This is to certify that the thesis entitled, "Solid State (Chemical) Synthesis and Electrical Characterization of Zinc Oxide (ZnO) Based Electronic Ceramic Sensors" describes the original research work done by Mr. Dinkar Kisanrao Kharat under my supervision for the Degree of Doctor of Philosophy in Physics of the University of Poona. Such material as has been obtained from other sources has been duly acknowledged in the thesis.*

Place: NCL, Pune-8.

Date : July 1993

  
26-7-93  
(Dr. S.K. Date)  
Scientist 'F'  
Deputy Director  
Research Guide



# C O N T E N T S

## **CHAPTER-1**

### INTRODUCTION

	<i>Page No .</i>
1.1 High – Tech ceramics	1
1.2 Electronic ceramic Ceramic sensors	3
1.3 Voltage sensors	5
1.4 zinc oxide (Zno) Based Voltage sensors	7
1.5 Review of Present status of Research and Development of Zno varistors	10
1.6 Scope and objective of the Present Work	11
1.7 Subject Matter Presented in the thesis	12
1.8 Crystal Structure and Band Structure of Zno	13
1.9 Basic Concept of Zno Varistor	16
1.10 Different Types of Varistors	17
1.11 Physics of a Varistor	18
1.12 Chemistry of a Varistor	22
1.13 Microstructure of a Varistor	27
1.14 Various conduction Models	30
1.15 Applications of Varistors	32
1.16 Fabrication /Development Methods of Zno Varistor	34
1.17 Future Trends of Zno Varistore	35

## CHAPTER-2

### EXPERIMENTAL TECHNIQUES

		Page <i>No.</i>
2.1	Introduction	40
2.2	Solid state synthesis of Active powders	40
2.3	Sintering	42
2.4	Physico Chemical Characterization	42
	2.4 (a) Density	42
	2.4 (b) phase Analysis	43
	2.4 (c) Microstructural Analysis	43
	2.4 (d) Surface Analysis	44
	2.4 (e) Electroding	44
	2.4 (f) DC Room Temperature Current –voltage (I-V) Characteristics	44
	2.4 (g) Ac Impedance Characterization	45
2.5	Modification of ZBCM varistor system	46

## CHAPTER-3

### RESULTS AND DISCUSSION

3.1	Introduction	47
3.2	Current- voltage ( I-V ) characteristics	48
3.3	Current –voltage (I-V) characteristics of ZBCM Varistor System	50
	3.3 (a) Density Analysis	52
	3.3 (b) Phase Analysis by XRD	54
	3.3 (c) Microstructural Analysis by SEM	56
	3.3 (d) Surface Analysis by XPS	60

	<i>Page No.</i>
3.4 Current –Voltage ( I-V ) Characteristics of ZBCM-10MgO Varistor System	63
3.4 (a) Density Analysis	66
3.4 (b) Phase Analysis by XRD	67
3.4 (c) Microstructural Analysis by SEM	68
3.4 (d) Surface Analysis by XPS	
3.5 Improvement in the performance parameter of ZBCM Varistor with 10mo1% MgO	73
References ( chapter 1 – 3)	76

## CHAPTER-4

### AC IMPEDANCE MEASUREMENT AND ANALYSIS

4.1 Impedance spectroscopy	95
4.2 AC Impedance Measurement Techniques	96
4.3 Complex plane Analysis	97
4.4 Electrical characterization of 10mo 1% Doped ZnO Based Varistore	102
4.5 Results and Discussion	104
References	113
<b>SUMMARY AND CONCLUSIONS</b>	117
List of publications	125
Acknowledgements	126

*Dedicated to.....*

My wife Madhavi and my daughters Priyanka  
and Piyusha who have all given so much help  
and encouragement to me.

*CHAPTER - 1*

**I N T R O D U C T I O N**

## 1.1 High-Tech Ceramics

We are approaching the twenty-first century with mixed feelings. Scientific and technological progress has launched us in high-tech era, but at the same time the ever-increasing demand on natural resources have put them dwindling to exhaustion. These facts have set the scientific and engineering community in frantic efforts to develop new novel materials. With the emergence of new era of electronic developments, electronic ceramic materials created a great deal of interest. The possible usages of these materials have driven the attention of the scientists/engineers towards the unexplored secrets of this field.

Ceramics, by definition, are the nonmetallic materials processed at high temperatures. High-tech ceramics differ from the conventional ceramics by virtue of their novelty of preparations and superior properties useful for high technological applications. Fig.1.1 depicts the detailed myriad functions, properties and applications of high-tech ceramics [1].

To synthesize high-tech ceramics, the focus of research must be on property control, structural development at the microstructural level and densification through emphasis on the use of fabrication methods (dispersing agents, emulsifications, dopants) and controlled temperatures. It is also known that controlled

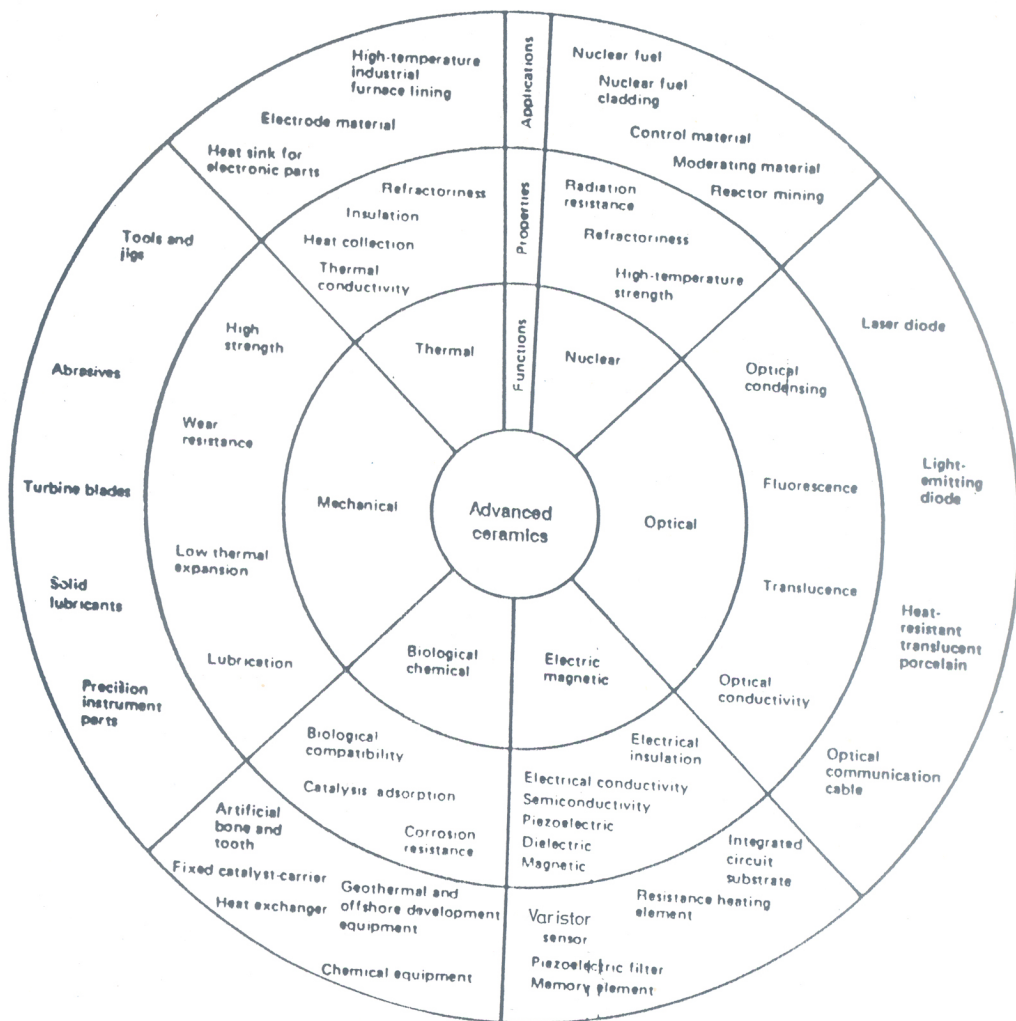


Fig. 1.1 Detailed myriad functions, properties and applications of High-Tech Ceramics (1).

powder geometry and chemistry leads to the structural integrity of ceramics. Consequently the properties of the dense ceramics with extremely good control over the grain size and its distribution, stoichiometry, texture etc. will match the theoretical upper limit known for single crystals. Fig.1.2(a) shows the ultrastructure processing chemistry approach to obtain high performance ceramics [2]. Many advantages are known in the preparation of powder forming and methods of densifications e.g. the powder required in electronic ceramics will necessarily have a crystal chemistry control to produce the specific physical properties. The term ultrastructure processing actually refers to the manipulation and control of surfaces and interfaces in the early stage of formation of crystallites at scales of 100-1000Å. Fig.1.2(b) shows the historical developments in improving the performance through controlled processing during the last fifteen years [2]. The emphasis lies on limiting and controlling the (i) physical, chemical homogeneous structures, (ii) extremely fine scale second phases, (iii) controlled surface gradients and ; (iv) unique combination of physical properties [2-9]. In ultrastructure processing, interdisciplinary concepts among the physics-chemistry-Materials Science-Engineering and micromechanics are integrated to get ceramics suitable for specific applications. Fig.1.3 shows the process control model of high performance ceramics through which the microstructures and ultrastructures are controlled by proper temperature-



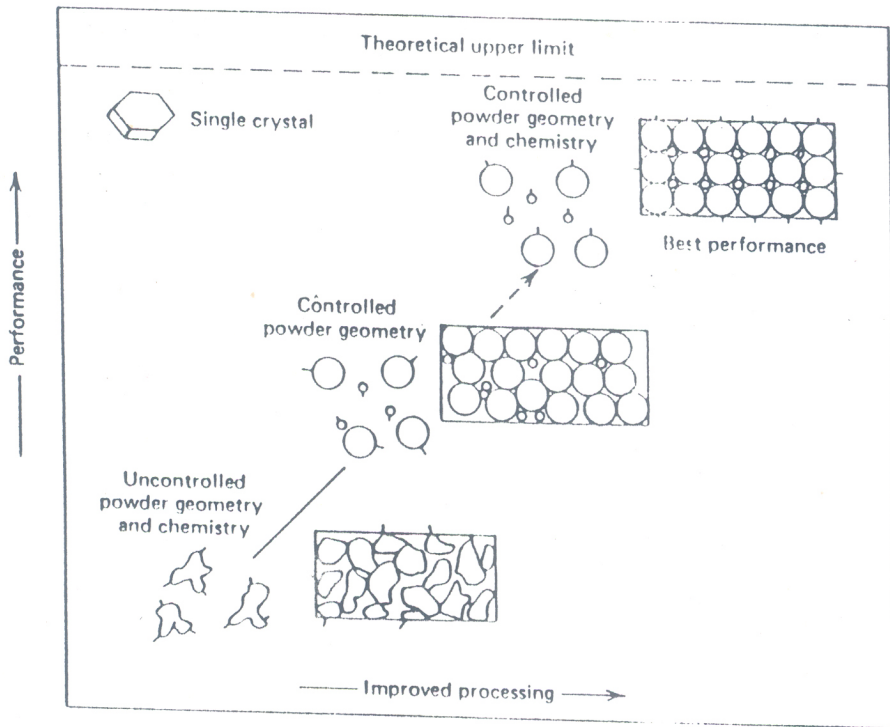


Fig. 1.2 (a) Ultrastructure processing chemistry approach for high performance ceramics (2)

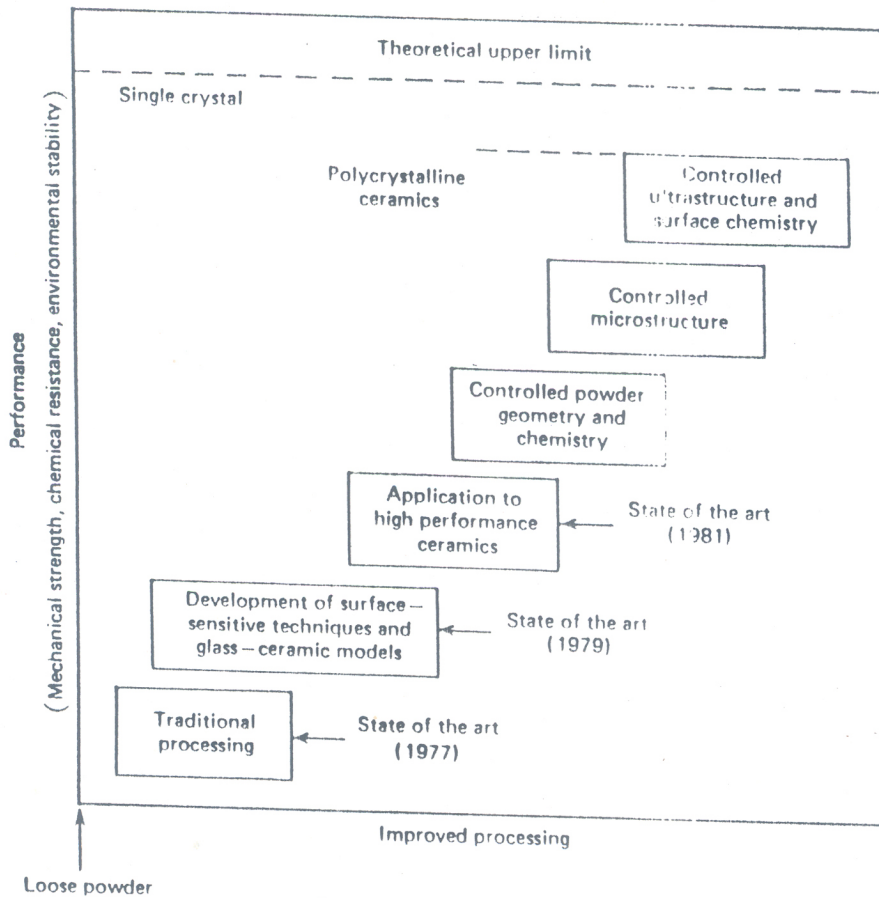
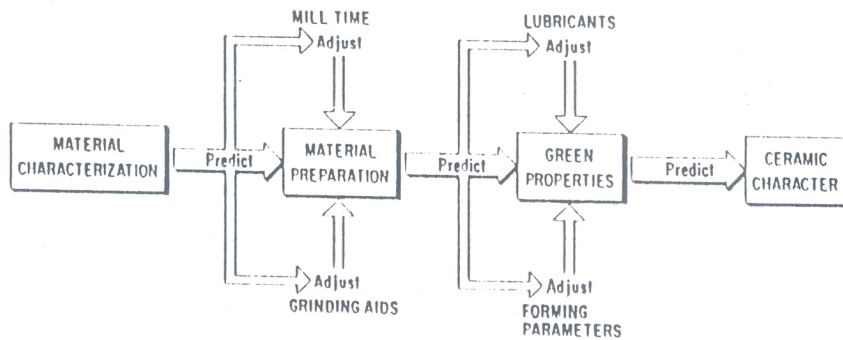
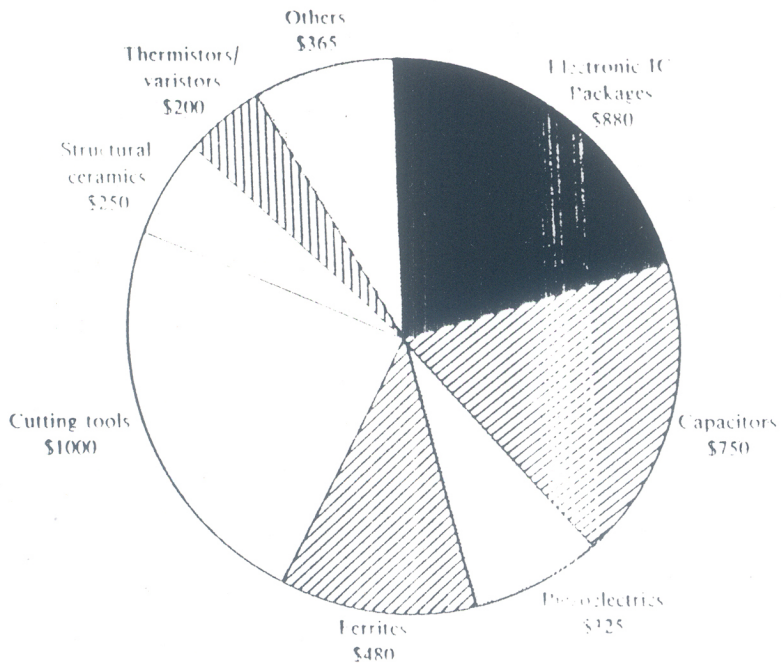


Fig. 1.2 (b) Historical developments in Ultrastructure proceedings (2)



**Fig. 1.3** Process control model of high performance Ceramics (10)



**Fig. 1.4** High technology ceramic market. Product and world sales (million \$). Total market in : 1980, \$ 4250 million; 1985, \$ 5500 million; 2000, \$ 15,000 million (15)

time correlations [10]. To get the outstanding performance parameters, the processing, synthesis and characterization play an important role [11-14]. In short, understanding the principles of processing of electronic ceramics are not only exciting but also of significant commercial value. The application range of the high performance (High-tech) ceramics are increasing at explosive rate. Fig.1.4 shows the enormous size of the market potential for these high technological materials in 1980, 1985 and 300% projected growth by the year 2000. The projected growth is one of the largest of any field of technology [15].

## 1.2 Electronic Ceramic Sensors

The operation of industrial world largely depends on the ability to measure, monitor and control the variety of physical, chemical and electrical parameters. The process requires sensing devices capable to perform these duties with high degree of reliability. The word "Sensor" means to sense and detect the required parameter or simply it is considered as "detecting element". Ceramic and semiconducting materials are useful as components for sensors and are currently in use. They are classified as follows [16]:

- (i) Those that utilize the physical properties of the grain itself.
- (ii) Those that utilize the properties of the grain

boundary.

- (iii) Those that utilize surface effects.

Ceramic sensors have currently become an integral part of the society and are being used in a variety of fields like industry, defence and various household gadgets [17-21]. The development of electronic and especially functional ceramics has supported the unbelievable progress of the electronics in the field of sensor technology. The marvels of these small and relatively inexpensive sensors both protect us from hazardous situations and make our lives more comfortable. The specific classification of ceramic sensor material is given in Table 1.1 [20].

**Table 1.1 : Classification of Ceramic Sensor Materials**

Exploited attribute	General application	Functional property	Material
Bulk properties	Temperature sensor	NTC thermistor	NiO, Fe <sub>2</sub> O <sub>3</sub>
	Oxygen gas sensor	Solid electrolyte	ZrO <sub>2</sub>
	Oxygen gas sensor	Semiconductor	TiO <sub>2</sub> , SrTiO <sub>3</sub>
	Pressure sensor	Piezoelectric	Pb(Zr, Ti)O <sub>3</sub>
	Radiation sensor	Pyroelectric	PZT Type
Grain Boundary properties	Temperature sensor	PTC thermistor	Doped BaTiO <sub>3</sub>
	Voltage sensor/ electronic sensor	Semiconducting varistor	ZnO, SrTiO <sub>3</sub>
Surface effect properties	Humidity sensor Electronic sensor	Catalyst/Varistor	ZnO-Cr <sub>2</sub> O <sub>3</sub> , MgCr <sub>2</sub> O <sub>4</sub> , BaTiO <sub>3</sub>

In addition to the above classification, Ichinose [16] has compiled the exhaustive list of ceramics which are being currently in use as ceramic sensors in a variety of field. Table 1.2 gives a typical listing of ceramic materials which are applicable for sensors.

### 1.3 Voltage Sensors

Most of the time, electrical/electronic devices suffer with the over-voltages developed due to natural lightning or an inevitable switching operations. During operation, the devices are seriously damaged and crept the economical losses. It is essential to suppress/bypass or eliminate the over-voltages to protect the sensitive devices/components. A device which performs these duties is known as voltage sensor or voltage suppressor. Voltage sensors offer the circuit protection to the sensitive devices during operations when voltages exceed dangerous levels [22].

In early stages i.e. prior to 1900, the spark gaps were used for over-voltage protections and guarding the sensitive devices. They were suffering from the following serious disadvantages:

1. On spark over, it remains as a short-circuit in the system, defeating the purpose of its usage.
2. The sparkover characteristics are statistical in nature and varies with ambient conditions.

Innovation of impulse gaps in 1918 [23] and

	Output	Effect	Material (form)	Remarks
Temperature sensor	Change in resistance	Temperature changes carrier density	(NIC) NiO, FeO, CoO, MnO, CoO Al <sub>2</sub> O <sub>3</sub> , SiC, (Bulk, thick film, thin film)	Thermometer, bolometer
		Semiconductor-metal phase transition	(PTC) Semiconductive BaTiO <sub>3</sub> (sintered body)	Overheat protection sensor
	Change in magnetism	Ferrimagnetism-paramagnetism transition	VO <sub>2</sub> , V <sub>2</sub> O <sub>5</sub>	Thermal switch
		Concentrated oxygen cell	Mn-Zn based ferrite	Thermal switch
Electromotive force		Stabilized zirconia	High-temperature corrosion-resistance thermometer	
Positron/speed sensor	Change in waveform of reflected wave	Piezoelectric effect	PZT: (PbTiO <sub>3</sub> , PbZrO <sub>3</sub> )	Fish finder, flaw detector, blood flow meter
Opto sensor	Electromotive force	Collecting effect	LiNbO <sub>3</sub> , LiTaO <sub>3</sub> , PZT, SrTiO <sub>3</sub>	Infrared ray detection
		Anti-stoke measurement	LaF <sub>3</sub> (Yb, Er)	
	Visible light	Progressive wave doubling effect	Piezoelectrics Ba <sub>2</sub> NbNb <sub>5</sub> O <sub>15</sub> (BNN), LiNbO <sub>3</sub>	Infrared ray detection
		Fluorescence	ZnS (Cu, Al), Y <sub>2</sub> O <sub>3</sub> S (Eu)	Color TV CRT
		Thermal fluorescence	ZnS (Cu, Al)	X-ray monitor
		CaF <sub>2</sub>	Thermal fluorescence dosimeter	
Gas sensor	Change in resistance	Inflammable gas contact combustion reaction heat	Pt catalyst/ alumina Pt line	Inflammable gas thermometer and alarm
		Migration of charge due to adsorption and desorption of gas from an oxidized semiconductor	SnO <sub>2</sub> , In <sub>2</sub> O <sub>3</sub> , ZnO, WO <sub>3</sub> , γ-Fe <sub>2</sub> O <sub>3</sub> , NiO, CoO, Cr <sub>2</sub> O <sub>3</sub> , TiO <sub>2</sub> , LaNiO <sub>3</sub> , (La, Sr) CoO <sub>3</sub> , (Ba, La) TiO <sub>3</sub> , etc.	Gas alarm
		Temperature changes in a thermistor due to gas heat conductive dissipation	Thermistor	High-density gas sensor
		Stoichiometric change in oxide semiconductors	TiO <sub>2</sub> , CoO MgO	Automobile exhaust gas sensor
	Electromotive force	High temperature solid electrolytic concentrated oxygen cell	Stabilized zirconia (ZrO <sub>2</sub> , CaO, ZrO <sub>2</sub> , Y <sub>2</sub> O <sub>3</sub> , La <sub>2</sub> O <sub>3</sub> ) Thoria (ThO <sub>2</sub> , Y <sub>2</sub> O <sub>3</sub> )	Exhaust gas sensor (random sensor) Molten steel and molten steel oxygen content analyzer
Amount of electricity	Coulomb titration	Stabilized zirconia	Lean combustion oxygen sensor	
Humidity sensor	Change in resistance	Moisture absorption in conductivity	LiCl, P <sub>2</sub> O <sub>5</sub> , ZnO, Li <sub>2</sub> O	Hygrometer
		Oxide semiconductor	TiO <sub>2</sub> , NiFe <sub>2</sub> O <sub>4</sub> , MgCr <sub>2</sub> O <sub>4</sub> , MgCr <sub>2</sub> O <sub>4</sub> + TiO <sub>2</sub> , ZnO Ni ferrite, Fe <sub>2</sub> O <sub>4</sub> , Colloid	Hygrometer
	Permittivity	Change in permittivity due to moisture absorption	Al <sub>2</sub> O <sub>3</sub>	Hygrometer
Ion sensor	Electromotive force	Solid electrolytic film concentrated cell	AgX, LaF <sub>3</sub> , Ag <sub>2</sub> S <sub>3</sub> , Thin glass film, CdS, AgI	Ion concentration sensor
	Resistance	Gate adsorption effect MOSFET	Si (Gate material H <sup>+</sup> for Si <sub>3</sub> N <sub>4</sub> /SiO <sub>2</sub> , S <sup>2-</sup> for Ag <sub>2</sub> S, X <sup>-</sup> for AgX, PbO)	Ion sensitivity FET (ISET)

Table 1.2 Typical listing of ceramic materials which are applicable for sensors.

development of silicon carbide (SiC) based voltage sensors around 1930 [24], set the stage for the emergence of the classical type of voltage sensors which reigned supreme from 1930 to almost 1970/80. These voltage sensors use a set of gaps in series with SiC based voltage sensors. All these components are hermetically sealed in an insulating housing, invariably a porcelain bushing. However, the presence of series gaps in this type of voltage sensors and the limited nonlinearity of the SiC based voltage sensors restricted the protective actions when deployed in the circuit elements.

In 1969, Matsuoka et. al. of Matsushita Electric Co., Japan, developed a new type of nonlinear resistance material based on zinc oxide (ZnO) which has superior nonlinear properties [25-26].

#### 1.4 Zinc Oxide (ZnO) Based Voltage Sensors

Zinc Oxide (ZnO) based voltage sensor belongs to a new class of electronic materials based on grain boundary properties. Its primary function is to sense and limit transient voltage surges and to do so repeatedly without being destroyed. In particular, sintered zinc oxide ceramics containing a variety of selective additives (dopants such as Bismuth oxide and other transient metal oxides) have shown excellent nonlinear current-voltage (I-V) characteristics [27-30] through controlled ultrastructural processings [31-33]. These unique

electrical properties make them suitable for the use as surge arrestors or voltage limitors in the electrical circuit/devices. Their function includes the following:

(i) Under low applied voltages, it acts as an open circuit element which satisfies Ohm's law (linear behaviour) and the current flowing is governed by the equation  $I \propto V$ .

(ii) At voltages above the preset (certain critical) value, its resistance decreases, enabling the large amount of current to flow through them and acts as short circuit element which does not obey Ohm's law (nonlinear behaviour) and the current flowing is governed by the equation  $I \propto V^\alpha$  where  $\alpha$  is a nonlinearity coefficient. In this mode, it offers the protection to the sensitive devices/components elsewhere present in the circuit. Because of these extraordinary property, these sensors are popularly known as nonlinear resistors, voltage dependent resistors, surge suppressors, surge protectors, varistors and voltage limitors, etc. The nonlinear behaviour appearing at high voltages is similar to back-to-back zener diode but with greater current and energy handling capabilities [34-42].

Nowadays, the varistors have been used in diverse field of applications such as voltage stabilization, transient surge suppression in electronic circuits and electronic power systems. In military electronics such as air craft, Nuclear Electromagnetic Pulses (NEMPs), ships and tanks, high performance varistors are being widely used



[43-65]. The study and usages of these not so costly materials, represent a continuously developing field in the area of science and technology of electronic ceramic sensors.

The fabrication of these high tech ceramic sensors with reproducible properties demands an improved processing of mixed precursors. There are many intriguing problems. It is well known that in the case of sintered compacts, structural flaws or defects, voids, cracks, inclusions, etc. must be avoided [66-67]. Control of physical and chemical homogeneity on a microscopic scale during powder synthesis, powder processing, powder consolidation and sintering is required. In addition, uncontrolled agglomerate formation during the synthesis and processing of ceramic powders (green compacts) results in a very poor microstructure. To overcome these drawbacks, many researchers have extensively studied the physics and chemistry of varistor technology and evolved excellent solutions to these problems [68-80]. The growing demand of zinc oxide varistors with better performance parameters has directed our attention to continue research in this field. The present work introduces the sensor community to the yet unsolved problems in ceramic synthesis and the fabrication of zinc oxide varistors. There are some excellent articles and reviews available in the literature on the various aspects of science and technology of varistors [25-26,28-29,62,81-86].

The increased application range of ZnO varistors is reflected by high level of worldwide research and development activity. The intense interest in this electronic ceramics is an indication of the growing range of applications and importance of ZnO varistor technology. It appears that quite likely, the usage of this material will grow and application scope broaden as the technology continues to mature. It is hoped that in the coming years, the research efforts in this area are likely to have a pathbreaking impacts in the design and development of better devices produced by controlling the structure-property correlations so as to make them most cost effective.

#### 1.5 Review of Present Status of Research & Development of ZnO Varistors

##### a) International status:

Considering the high potential applications of the ZnO based varistors, extensive work has been carried out for the past two decades. Major companies like TDK, General Electric (GE), Mitsubishi, Siemens etc. are manufacturing ZnO based varistors for the wide range of applications.

##### b) National status:

In spite of its potential applications in India there are only few institutions like I.I.Sc., Bangalore, R.R.L., Trivandrum, N.C.L., Pune working in this field.

Extensive studies on the characterization and optimization of ZnO based varistors with specific applications in mind have not yet been attempted. The only company producing varistor in India is M/s. Elpro International, Pune, with the technical collaboration of G.E., USA.. There is no manufacturer of ZnO based varistors in India who can meet the requirements of the various applications. As per the latest survey carried out, the projected requirement of varistors in India is 7 million pieces in 1995. Table 1.3 gives the market potentials of ceramic sensors in India [87-88].

**Table 1.3: Market Potential of Ceramic Sensors in India**

Year	1990		1995	
	Nos. in million	Value in Rs. million	Nos. in million	Value in Rs. million
Thermistor	4.2	42	6.8	68
Varistors	5.2	50	7.0	70
Humidity Sensors	Small	Small	Small	Small
Gas Sensors	Small	Small	Small	Small
Total	9.2	92	13.8	138

### 1.6 Scope and Objective of the Present Work

It is known that fundamental exploratory research regularly produces unexpected and useful results. The incentive for the present work lies in the vast scope for R&D in exploitation of the well established materials

through novel routes of preparation and processing as well as characterizing them with the modern techniques like XRD, SEM, ESCA, I-V measurements and ac impedance analysis, etc.

The basic framework of the thesis is therefore constrained into, (i) the development of simple ZnO based varistors comprising of 97 mol% ZnO and 1 mol% each of  $\text{Bi}_2\text{O}_3$ ,  $\text{Co}_2\text{O}_3$  and  $\text{MnO}_2$ , their synthesis and characterization etc., (ii) modification in the basic system, using MgO as a grain growth inhibitor to get improved performance parameters, their synthesis and characterization; (iii) to conduct series of well-documented experiments to establish the processing parameters and its optimization, (iv) to achieve a good functional microstructure through process-property correlations, (v) physico-chemical characterizations of the active powders/samples/specimens by means of specialised techniques like XRD, SEM, ESCA, I-V measurement and AC impedance analysis for establishing correlation between functional and electrical microstructures.

### 1.7 Subject Matter Presented in the Thesis

The thesis is divided into four chapters. Chapter-1 includes, the general introduction on High-Tech Ceramics with special emphasis on ZnO based varistors, their principle of operation, various developmental methods and application potentials. The review on physics, chemistry, microstructure and various conduction models are broadly

presented.

Chapter-2 includes, the experimental techniques used in the synthesis of the active powders and their physico-chemical characterizations.

Chapter-3 includes, the results and discussion on (i) DC current-voltage (I-V) characteristics measured at room temperature as a function of sintering temperatures and, (ii) Density, phase (XRD), microstructure (SEM), surface (XPS) analysis studies.

Chapter-4 includes, the results and discussion on ac impedance measurements on the selected samples/pellets.

At the end of the thesis, a critical summary and conclusions along with exhaustive list of bibliographical references on the subject are presented.

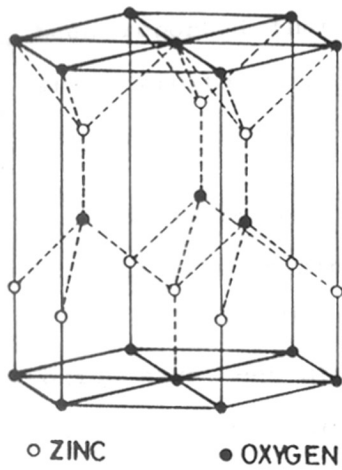
## 1.8 Crystal Structure and Band Structure of ZnO

ZnO has a wurtzite structure in which the oxygen atoms are arranged in a hexagonal close-packed type of lattice with zinc atoms occupying half the tetrahedral sites [62,89-90]. The two types of atoms, Zn and O are tetrahedrally coordinated to each other and are, therefore, equivalent in position. The ZnO structure is thus relatively open with all the octahedral and half the tetrahedral sites empty. It is, therefore, relatively easy to incorporate external dopants into the ZnO lattice as is

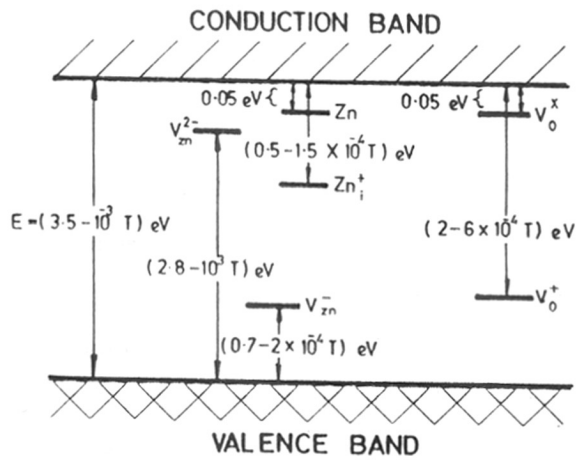
observed in a varistor. The open structure has also a bearing on the nature of defects and the mechanism of diffusion. The most common defect in ZnO is the metal atom in the open interstitial sites leading to a nonstoichiometric metal excess of n-type semiconductor. The band gap of ZnO has been determined to be 3.3 eV from the optical studies, and thermodynamically formed natural defects occupy the donor and acceptor levels within the band gap. The interstitial Zn( $\text{I}$ ) has the fastest diffusion rate among the natural defects and plays a significant role in varistor stability. Figs.1.5(a)-1.5(b) depict the crystal structure and band structure of ZnO.

The resistivity of ZnO is typically 1-2  $\Omega\text{-cm}$  at 25°C and can be decreased by quenching from high temperature. Doping with  $\text{Na}^+$  ions introduces electron traps into the material, increasing the resistivity to the point where space charge limited current can be observed [91]. Nonlinear conduction has also been reported for surface barriers formed on ZnO by Au and Pd contacts [92]. In general, monovalent ions (e.g.  $\text{Li}^+$ ) tend to increase the resistivity of doped sintered polycrystalline ZnO by creating electron traps and trivalent ions (e.g.  $\text{Al}^{3+}$  and  $\text{Cr}^{3+}$ ) tend to decrease it by supplying extra conduction electrons [93].

The effects of ambient atmosphere on the ZnO can also be interpreted in terms of interstitial Zn diffusion as the rate controlling steps [94-95]. The addition of a trivalent



(a)



(b)

Fig. 1.5 (a) Crystal Structure and

(b) Band structure of ZnO (62)

When ZnO pellets without or with bed of ...

dopant increases the concentration of conduction electrons and simultaneously reduces the equilibrium concentration of Zn interstitials, so that the increase in electrical conductivity is accompanied by a decrease in the Zn diffusion coefficient. Thus, the effect of mono and trivalent dopants can be seen in sintering kinetics [96] as well as surface catalytic activity [97]. However, it has been reported that small additions of  $K_2O$  to ZnO inhibit grain growth, just the opposite of what is expected for monovalent dopants [98].

Matsuoka et al. [25-26] first found the voltage nonlinearity in zinc oxide ceramics doped with alkali earth metal oxides. The usual semiconducting properties of zinc oxide have been studied by Hahn [99] and Harison [100]. The cold pressed bodies of zinc oxide powder with 0.5 mol% of alkali earth metal oxide additives (e.g. CaO, SrO, BaO, BeO, MgO) have been sintered in air at various temperatures from 950° to 1450°C for one hour. The current-voltage (I-V) nonlinearity coefficient ' $\alpha$ ' has been measured in accordance with the method described by Masuyama et al. [101].

The sintered ZnO pellets without or with BeO or MgO additives have  $\alpha = 1$ . Those with CaO, SrO or BaO additives however produce  $\alpha > 1$ . When the ionic radius of the dopant e.g.  $Be^{2+}$  and  $Mg^{2+}$  is smaller than that of  $Zn^{2+}$  then the product shows a linear current voltage characteristics. On



the other hand, additives having the ionic radius larger than that of  $Zn^{2+}$  produce non-linear current-voltage characteristics.

Electron photomicrographs have shown that the sintered body with linear voltage-current characteristic has apparently no second phase segregated, whereas the sintered body with  $\alpha > 1$  has a second phase segregated at the grain boundaries. In view of the general rule [102] that the solubility depends on the ionic radius, the added CaO, SrO or BaO should not dissolve in the ZnO lattice but should form a segregated phase. It is believed that this segregated phase may be responsible for the observed non-linear characteristics.

### 1.9 Basic Concept of ZnO Varistors

The word varistor is a variable resistor whose resistance is a function of the applied voltage. The current-voltage behaviour can be divided into three groups [25-26,62,81-83].

i) Under the low applied voltages, the varistor functions as an open circuit, which satisfies Ohm's law (linear behaviour).

(ii) At voltages, above certain critical value, its resistance (changes) decreases, enabling a large current to flow through the varistor, indicating that the varistor becomes short-circuited and does not obey Ohm's law

(nonlinear behaviour).

(iii) If the voltage is further increased beyond the critical value, the varistor again behaves like an open circuit and follows Ohm's law (linear behaviour). Fig.1.6 shows schematic nonlinear behaviour of a varistor.

#### 1.10 Different Types of Varistors

There are different classes of varistors developed from sintering of different raw materials during the last four decades. A comparison of characteristics of three types of varistors are given in Table-1.4.

**Table-1.4:** Comparative Evaluation of Different Types of Varistors [85-86,103]

Property	SiC	Zner	ZnO
Raw material	Sintered SiC	P-n junction	Sintered ZnO
Mechanism	Barrier at grain boundaries	P-n junction	Barrier at grain boundaries
I-V behaviour	Rise voltage 5-100V	2-30V	5-1 MeV
Nonlinear index ( $\alpha$ )	3 ~ 7	6 ~ 150	20-100

As evident from the table, zinc oxide varistor shows better nonlinear performance at high applied voltages. In addition ZnO varistor offers the advantage of nanosecond switching speeds. They are very small in size and are able to handle current surges of the order of hundreds of

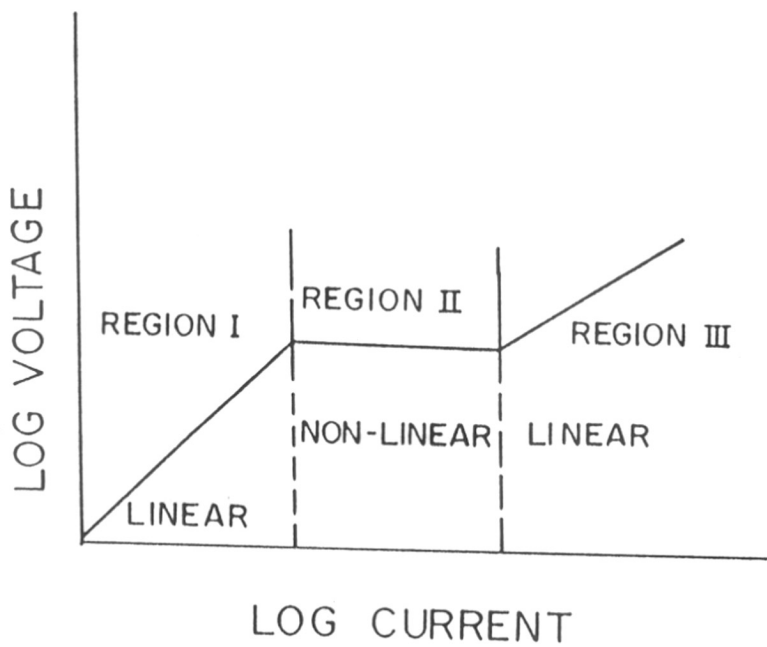


Fig. 1.6 Schematic non-linear behaviour of ZnO based varistor (26, 62, 81-83)

amperes. They have steep nonlinear voltage current characteristics with large nonlinearity index ( $\alpha$ ) values. Further it can also pass widely varying current over a narrow voltage range. They require very little stand by power, making it useful for guarding semiconductor devices. The steady state power dissipation of the zinc oxide based varistor is typically a fraction of milliwatt as compared to the few tens of watts dissipated by some other power varistors. In the recent years the performance of zinc oxide varistors has been continuously improved as indicated by the increasing trends in their performance parameters. It is further expected that the superior characteristics of ZnO based varistors will increase system reliability and will eventually result in reduction in equipments cost.

#### 1.11 Physics of a Varistor [104-125]

The important property of a zinc oxide varistor is its nonlinear current voltage characteristics. It is seen from the typical I-V curve (Fig.1.7) that varistor acts as an insulator (resistor) before reaching a voltage known as the breakdown or threshold voltage. After it passes the breakdown voltage, it acts as a conductor. The only characteristics which attract the designer are the nonlinear or nonohmic property in the conductive mode and the low leakage at the steady operating voltage in the resistive mode. The I-V characteristics can be divided into three regions as given below:

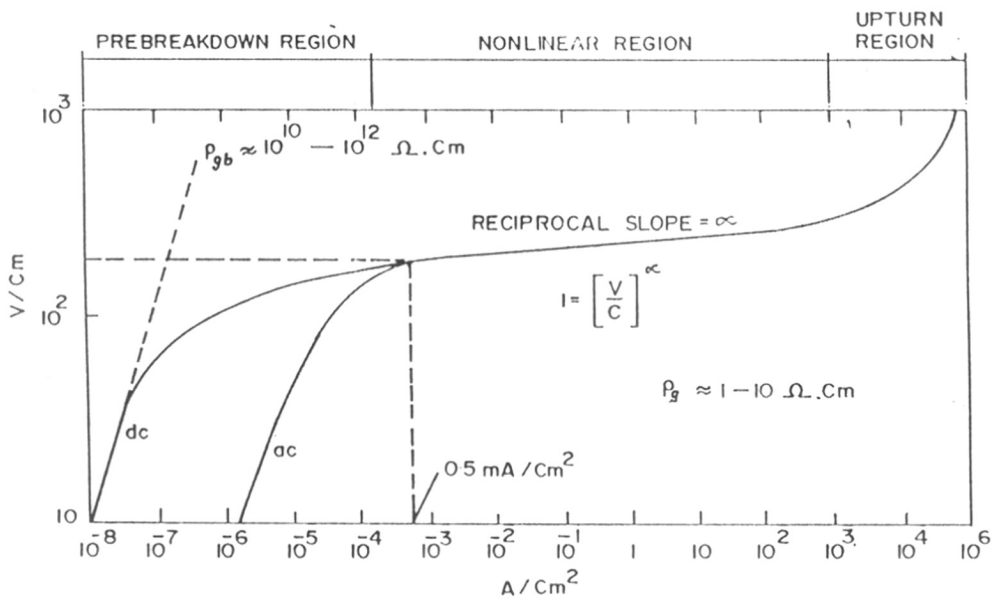


Fig. 1.7 Typical current voltage (I-V) characteristics of a ZnO based varistor (62).

(a) Low Current Region

This region is called the prebreakdown region, in which the current-voltage relationship follows the Ohm's law. The ac current is about two orders of magnitude higher than the dc current for a given operating voltage. This difference arises due to two contributing factors: (i) the total ac current is composed of capacitive current ( $I_C$ ) and resistive current ( $I_R$ ) and; (ii) impedance of the ZnO grains.

(b) Intermediate Region

This region is called the nonlinear region. It is a signature of ZnO varistor, where the device conducts increasingly large amount of current for a small increase in voltage. Under the optimal operating conditions, it extends to 6-7 orders of magnitude of current. In this region, the degree of nonlinearity is expressed by the empirical equation.

$$J = (E/C)^\alpha \quad \dots\dots (1.1)$$

Where  $J$  = current density,  $E$  = electric field,  $C$  = constant related to the nonlinear resistance and  $\alpha$  = nonlinearity coefficient. The nonlinearity coefficient  $\alpha$  is usually calculated from the I-V plots, plotted in the logarithmic scales:

$$\alpha = \frac{dI/I}{dV/V} = \frac{d(\log I)}{d(\log V)} \approx \frac{\log_{10} I_2 - \log_{10} I_1}{\log_{10} V_2 - \log_{10} V_1} \quad \dots\dots (1.2)$$

where  $V_1$  and  $V_2$  are the appropriate voltages at the currents  $I_1$  and  $I_2$  respectively. The breakdown electrical field  $E_b$  is also calculated from equation (1.1) and (1.2) as,

$$E_b = C.J^{1/\alpha} \text{ V/mm at } 1 \text{ mA/cm}^2 \quad \dots\dots (1.3)$$

(defined as the voltage observed at  $1 \text{ mA/cm}^2$  and expressed in V/mm).

Equation (1.1) can be further written as,

$$J = KE^\alpha \text{ or } E = C J^\beta \text{ where } K = (1/C)^\alpha$$

$$\text{and } \alpha = 1/\beta = \implies \beta = 1/\alpha$$

The power dissipation in a varistor is given by equation,

$$W = E.J = E K E^\alpha = K E^{\alpha+1} \quad \dots\dots (1.4)$$

The resistance of a varistor can be calculated from the Ohm's law

$$R = \frac{E}{J} = \frac{E}{KE^\alpha} = \frac{1}{KE^{\alpha-1}} \quad \dots\dots (1.5)$$

Using equation (1.4) one can get the resistance from eqn.(1.5)

$$R = E/J = C. \frac{J^\beta}{J} = \frac{C}{I^{1-\beta}} \quad \dots\dots (1.6)$$

Equation (1.6) shows that the value of the resistance of a varistor is not constant but depends on the value of the

current flowing through the device. The degree of nonlinearity is determined by the flatness of the nonlinear region, i.e. flatter the I-V curve signifies higher nonlinear coefficient  $\alpha$  and therefore better the device. The controlling parameters, for this important region are understood only qualitatively till today. The simplified picture of our understanding can be depicted as follows. The zinc oxide and various dopants form a tailored microstructure comprising large semiconducting zinc oxide grains separated from each other by highly insulating grain boundaries. The addition of  $\text{Bi}_2\text{O}_3$  and other dopants has been found essential for forming grain boundaries. The addition of other transient metal oxides like  $\text{CO}_2\text{O}_3$  and  $\text{MnO}_2$  enhances the nonlinearity coefficient. The highly insulating intragranular layers/boundaries and conducting grains are necessary for high degree performance of the varistor.

(c) The upturn region

This region is called high current region. In this region, the current-voltage characteristic again follows Ohm's law similar to low current region. These two regions, namely prebreakdown and upturn regions are not useful in the functioning of the device. The high current density in the upturn region is mainly limited by grain resistivity of ZnO crystals and not by the effect of potential barriers localized at grain boundaries. The relationship between current and voltage is given by,



$$V = R_g \cdot I \quad \dots \quad (1.7)$$

where  $R_g$  is the equivalent grain resistance. In other words, lower grain resistance signifies lower voltage and hence, offers better protection against transient surges.

### 1.12 Chemistry of a Varistor

In practice, zinc oxide varistors are mostly produced via conventional solid state (chemical) route. It involves thorough mixing of the high purity oxide powders and processing the resulting mixture in a controlled fashion. Temperature, pressure, time, etc. are the most important processing parameters. By following very stringent experimental conditions, various researchers have obtained excellent performance parameters. However, reproducibility was not satisfactory. As mentioned earlier, there are many microstructural defects (chemical and physical) responsible for nonreproducibility. Considerable amount of work is being carried out to improve the non-ohmic behaviour of zinc oxide varistor with small amount of other oxide additives. To obtain better non-ohmic properties, different methods have been tried to change the experimental conditions by adding one or more additives [126-151]. Attempts have also been made to sinter the materials under different atmospheres. However, it was observed that in all these attempts, approximately the same preparation techniques are being followed, i.e. conventional ceramic techniques. This method suffers from

many shortcomings which considerably affect the performance of the ceramic product. It is possible to indicate these shortcomings as: (i) the product loses the uniformity and homogeneity, and; (ii) the lattice defects are being introduced because of ball-milling techniques which considerably affect the electrical and mechanical properties.

In our laboratory, novel chemical methods are being developed as an alternative route to achieve highly uniform monosized/monodispersed particles. One of the methods is known as "Liquid Mixed Technique" (LMT). Full details of this method have been discussed in a series of papers published from our group [152-158]. However, a brief outline is shown in the schematic diagram (Fig.1.8).

The first step is the formation of an aqueous solution containing both cation complexed in citric acid. Usually metal carbonates are taken as precursors because they dissolve in citric acid solution via a simple acid base reaction. The second step involves slow heating of the solution to remove the solvent and to form a solution with increasing viscosity. The resultant glassy product is a homogeneous and mixed at atomic levels. Finally, the product is calcined at about 900°C to oxidize the remaining part of the organics. No precipitation should be allowed during the slurry formation as it would lead to drastic inhomogeneities. The fine grain powder of uniform

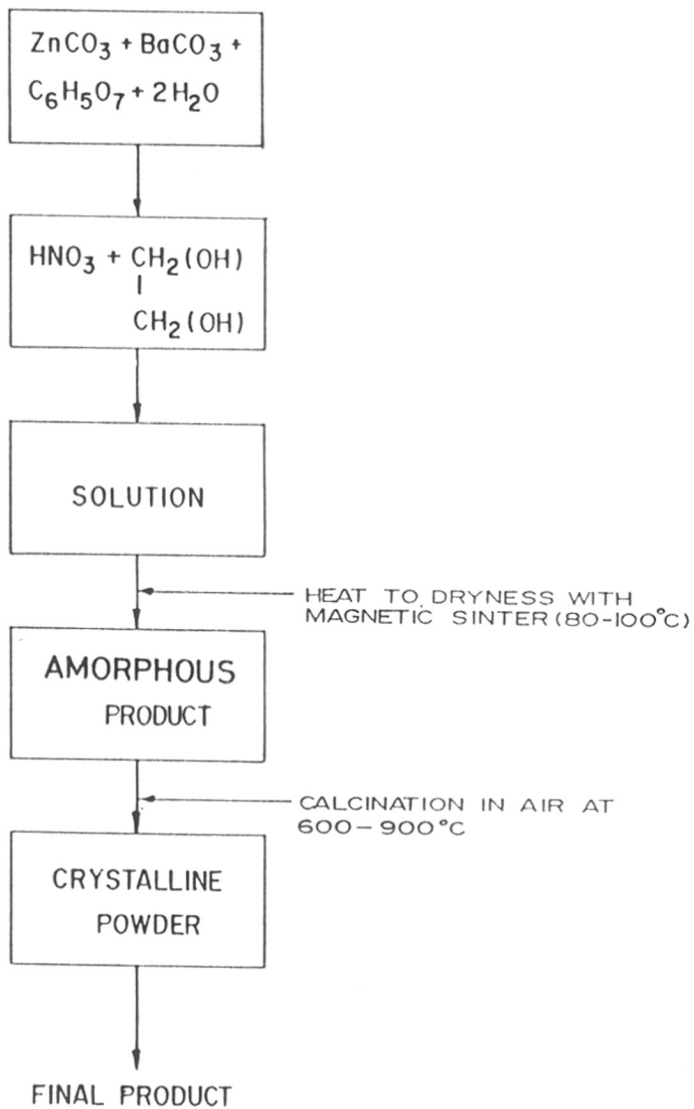
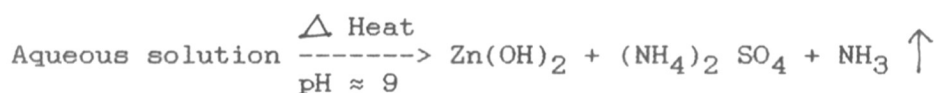


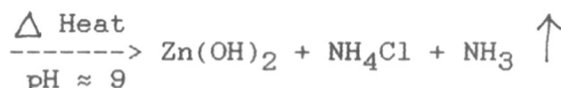
Fig. 1.8 Schematic diagram of Liquid Mixed Technique (LMT) (152 - 158)

particle size can be further processed under controlled oxygen partial pressure. For example, ZnO-BaO composition synthesized using Liquid Mix Technique (LMT) have exhibited the non-ohmic behaviour with a nonlinearity coefficient  $\alpha=6$ .

Recently a new chemical processing route has been reported to precipitate spherical zinc oxide powders for varistor applications [159-172]. The two step reaction is illustrated with either zinc sulphate or zinc chloride.



Or,



Unfortunately, high purity zinc oxide cannot be prepared by calcining either of these zinc hydroxy salt precursors. However,  $\text{Zn}(\text{OH})_2$  can be obtained from any of the basic zinc salts by first dissolving the salt in concentrated  $\text{NH}_4(\text{OH})$  and then allowing the pH to fall slowly with the evaporation of ammonia. In this method, the processing parameters are precursor concentration, precursor material, temperature and pH. It has also been found that methanol and ethanol are the best dispersing agents and can be used along with other suitable solvents.

Another novel chemical processing method is based on sol-gel principle [167] for the preparation of ZnO powders, using inexpensive source materials such as acetate and nitrates. It yields powders with a more homogeneous distribution of dopants compared to the commercially used mixed oxide technique. Varistor ceramics made from sol-gel powders can be sintered at lower temperatures and show improved electrical behaviour. Fig.1.9 gives the schematic block diagram of the sol-gel method. Table 1.5 gives the comparative evaluation of the varistors produced by conventional and sol-gel method.

Recently, Sandia-National Laboratory, USA, has developed a new ceramic production technique yielding highfield varistors of 20-100 kV/cm switching voltages [173].

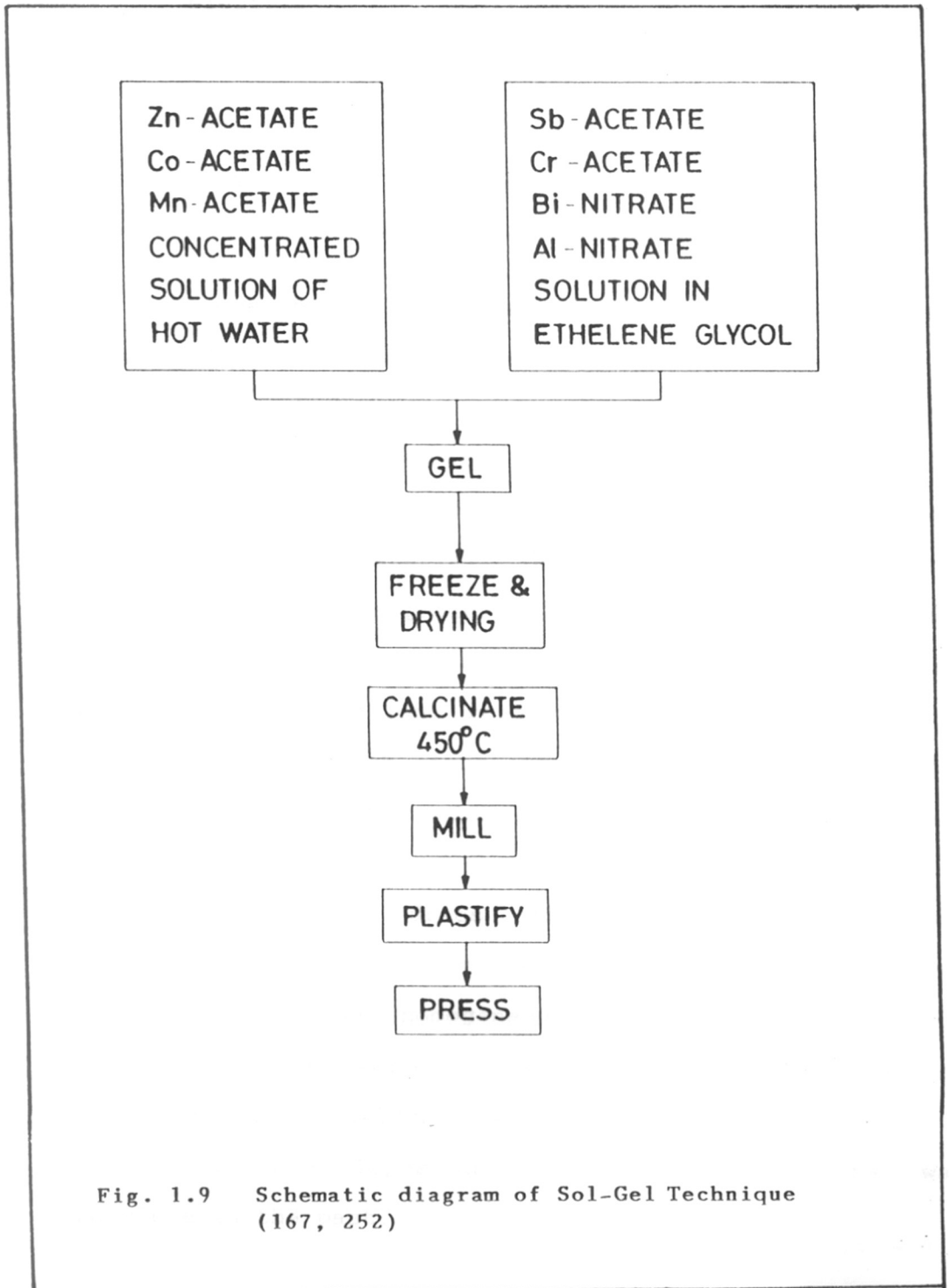


Fig. 1.9 Schematic diagram of Sol-Gel Technique (167, 252)

**Table-1.5:** Comparative evaluation of ZnO varistors produced by conventional and sol-gel methods

Method	Breakdown electric field $E_b$ (V/mm)	Nonlinear coefficient $\alpha$	Leakage current $I_L$ ( $\mu A$ )
Sol-Gel	375	55-60	0.9
Conventional	225	45-50	7-70

The process begins by dissolving zinc, manganese and cobalt chlorides in an aqueous solution and reacting it with sodium hydroxides under controlled condition of precipitation. The precipitated hydroxide powder is reacted with oxalic acid and calcined at 600°C to drive off the volatile material. The end result is a uniform powder mixture with grains of a predetermined shape and size which is controlled by the exact time and temperature of the precipitation reaction. Subsequently, acidic solution of bismuth ions is poured over the powder allowing the bismuth ions to react with the grain surfaces, leaving a very thin coating. A calcination operation at 400°C dries off excess water and other volatile materials to produce a well defined mixture. After pressing the homogeneous powder into a suitable shape, the final sintering operation is performed around 750°C. A ceramic varistor with only 10% porosity results in regulating voltages upto 100 times higher than was possible in the past.

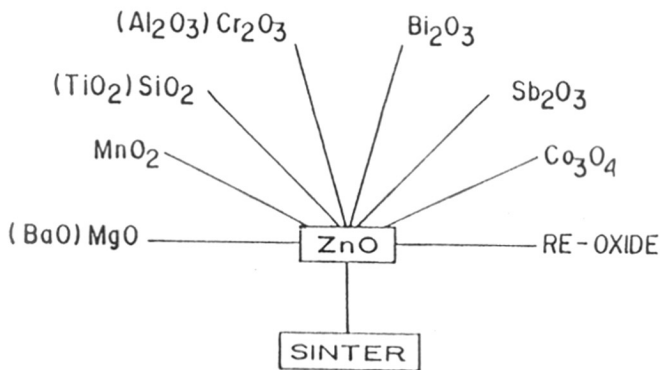
### 1.13 Microstructure of a Varistor

The microstructure of a varistor is considered as a means of interwound transportation network through which all the properties are manifested [62,81-83]. It is also considered as a building block of zinc oxide varistor. Therefore, microstructure must be considered as a most important signature of a varistor. The major findings of a microstructural analysis are summarised in Fig.1.10. The typical average grain-size in a commercial ZnO varistor is of the order of few  $\mu\text{m}$ , and the grains are always accompanied by twins. The presence of  $\text{SiO}_2$ ,  $\text{MgO}$  and  $\text{Al}_2\text{O}_3$  inhibits the grain growth whereas  $\text{TiO}_2$  and  $\text{BaO}$  accelerates the grain growth.

The properties of ZnO varistor very strongly depend on the microstructure of the sintered compacts [174-188]. The word microstructure can be well understood by analysing the scanning electron micrograph given in Fig.1.11. From this micrograph, the important qualities about the grain size, shape, distribution, voids, cracks, pores and homogeneity, etc. can be studied. This analysis is usually carried out by Scanning electron microscopy (SEM), X-ray photoelectron spectroscopy (XPS) and X-ray diffraction studies [26-29,62,137,174-175,189-201]. The major findings about the microstructure of ZnO varistor can be summarised as:

(i) Depending upon the processing parameters at high temperatures, four separate phases are formed. These are -





<u>COMPOUND</u>	<u>CHEMICAL FORMULATION</u>	<u>DOPING ELEMENT</u>	<u>LOCATION</u>
ZnO	ZnO	Co, Mn	GRAJNS
SPINEL	$Zn_7Sb_2O_{12}$	Co, Mn, Cr	INTERGRANULAR PHASE
PYROCHLORE	$Bi_2(Zn_{4/3}Sb_{2/3})_6$	Co, Mn, Cr	INTERGRANULAR PHASE
Bi-RICH PHASES	$12Bi_2O_3 \cdot Cr_2O_3$	Zn, Sb	TRIPLE POINT
	$14Bi_2O_3 \cdot Cr_2O_3$	Mg, Al	
	$\beta - Bi_2O_3$		
	$\delta - Bi_2O_3$		
	$12Bi_2O_3 SiO_2$		

Fig. 1.10 Major findings of Micro-structural analysis (62).

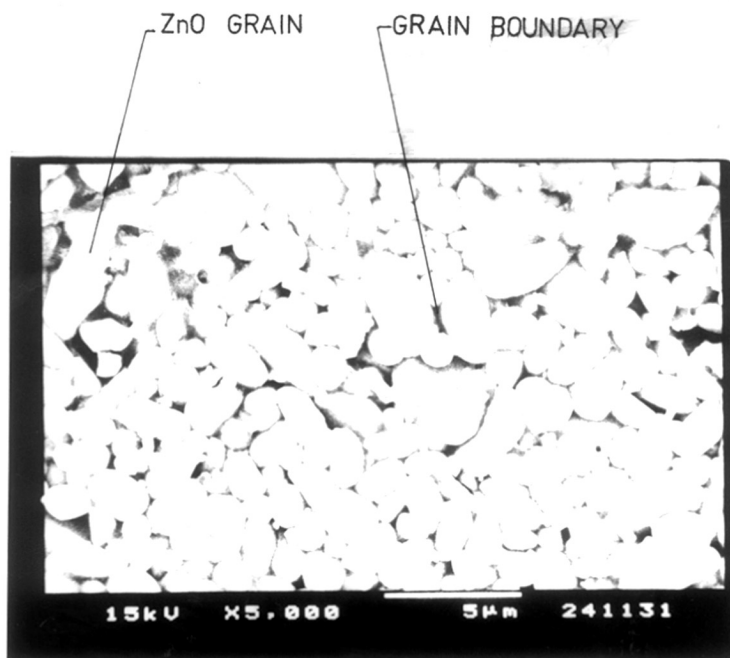


Fig. 1.11 Typical scanning Photomicrograph of a ZnO based varistor.

zinc oxide, spinel, pyrochlore and several bismuth rich phases.

(ii) These phases are formed at different locations such as grain, intergranular layer/phase and triple point. In addition, there are many minor phases which cannot be detected easily by usual analytical techniques.

(iii) The chemical formulation of the final dense compacts is complex due to the nature of the doping elements.

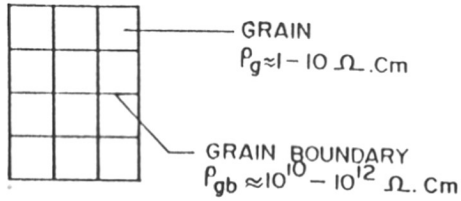
(iv) It is observed that a pyrochlore phase is formed during the low temperature processing, whereas the spinel phase is formed during high temperature processing.

(v) There are few grain growth inhibitors added during the processing of the varistors. The exact role of these inhibitors is understood only by trial and error method, and has not been established.

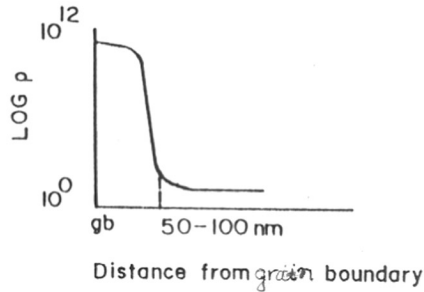
There are only few experiments performed to understand the relationship between the microstructure and varistor mechanism by SEM, EDAX, XPS and XRD techniques. In case of two component ( $\text{ZnO-Bi}_2\text{O}_3$ ) varistor system, the formation of four different constituents have been observed in our laboratory [189-191]. The basic building block of a ZnO varistor are the ZnO grains formed as a result of sintering process. Various chemical elements (dopants) are distributed in the microstructure and form

grain and grain boundaries. The role of grain and grain boundaries are discussed excellently in a recent review article by Levinson and Philipp [81].

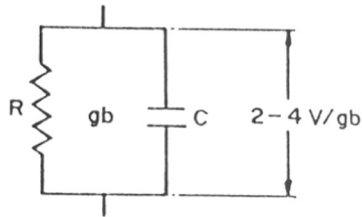
Fig.1.12(a) is the schematic diagram of the apparent grain and grain boundary resistivities. A sharp drop in the resistivity from grain boundary to grain as shown in Fig.1.12(b) occurs within a distance of about 50-100 nm. The spatial distance is known as the depletion layer. In this way, at each grain boundary, there exists a depletion layer on both sides of the grain boundary extending into the adjacent grains. As the region near the grain boundary is depleted of electrons, a voltage drop appears across the grain boundary, due to the application of an external voltage known as barrier voltage. Typically, it is of the order of 2-4 volts/grain boundary. This voltage is the sum of the resistive (R) and capacitive (C) components. The equivalent circuit is shown in Fig.1.12(c). When a voltage stress is applied to a ZnO varistor in the breakdown region, the leakage current that flows through the device is entirely of the grain boundary origin. The nonlinear behaviour of a varistor is indirectly controlled by the resistivity difference between the grain and the grain boundary. The comparative evaluation of current-voltage curve with the microstructure of ZnO varistor provides an important tool to adjust the electrical property of the grain boundary as well as that of the grains so as to meet the requirement for a given technological



(a)



(b)



(c)

Fig. 1.12 Schematics of microstructure and electrical characteristics of a ZnO varistor (62)

- a) Grain versus grain boundary resistivity
- b) Resistivity profile at the depletion layer.
- c) Equivalent electrical circuit at the grain boundary

applications[202-233].

#### 1.14 Various Conduction Models

The mechanism of the electrical conduction in the non-ohmic region of zinc oxide varistor ceramics is not yet completely understood and still remains a difficult problem to be solved. Since 1971, various researchers have proposed different models to explain their experimental results [26-27,60,70,81,83,234-246]. Eda [83] has summarised various models to explain the electrical conduction in ZnO varistors as given in Table-1.6. It is clearly seen that all these models can be grouped according to the three different physical concepts:

- (i) Space charge limited current (SCLC),
- (ii) Tunneling across the barrier, and
- (iii) Space charge induced current (SCIC).

Depending upon the nature of intergranular layer, these models are operative to control current-voltage and capacitive-voltage characteristics. The common underlying requirement of these models are:

- (a) Extremely homogeneous microstructure of zinc oxide grains.
- (b) Highly insulating bismuth oxide rich intergranular layers separating the semiconducting zinc oxide grains.
- (c) The applied electrical stresses induce the profound changes in the microstructure of the varistor which, in turn, influence the nonlinear behaviour.

Table-1.6: Theoretical models developed during last twenty years to explain the non-linear behaviour

<i>S.No.</i>	<i>Model</i>	<i>Year</i>
1.	Invention of ZnO varistors (Matsuoka et al.)	1968
2.	Discovery of various kinds of additives	1968-75
3.	Space charge - limited current (Matsuoka)	1971
4.	Tunneling through a thin layer (Levenson & Philipp)	1975
	Tunneling through Schottky barriers (Levine)	
5.	Tunneling through Schottky barriers Morris, Bernascone et al.	1976
6.	Tunneling through Schottky barriers with heterojunctions (Emtage)	1977
7.	Tunneling through Schottky barrier with heterojunctions (Eda)	1978
8.	Tunneling through homojunctions (Einzinger)	1978
9.	Tunneling through Schottky barriers (Hower and Gupta)	1979
10.	Bypass effect at heterojunctions (Eda)	1982
11.	Hole induced breakdown (Pike)	1984
12.	Bypass effect at heterojunctions (Levenson and Philipp)	1986
13.	Hole induced breakdown (Blatter and Greuter)	1986
14.	Space charge induced current (Suzuki et al.)	1987

### 1.15 Applications of Varistors

The varistors are in use for the last 40 years in one or the other form so as to regulate the transient voltages of unwanted magnitudes. The oldest of the devices are based on selenium rectifiers, used extensively in older telephone systems and other surge suppressor applications. With the advent of modern technology, they have been replaced by the single crystal silicon devices for low voltage applications and by polycrystalline ceramic nonlinear devices of SiC and ZnO for high voltage and power related applications. As a result of vast improvement in performance, ZnO devices are systematically replacing the silicon carbide devices in most areas of power applications. As the devices are available in a considerable smaller size (micro) their range of applications in the field of automotive and telephone industries are continuously increasing. The exhaustive list of these devices is indicated by huge tree shown in Fig.1.13. The potential applications of these devices are in the following areas [43-45,47,113].

- 1) Consumer electronics : TVs, micro ovens, stereos,  
power outlets.
- 2) Industrial protections: Motors, thyristors, relays.
- 3) Communications : Telephones, relays.
- 4) Military electronics : Aircrafts, nuclear electro-  
magnetic pulses (NEMPs),  
ships, tanks etc.



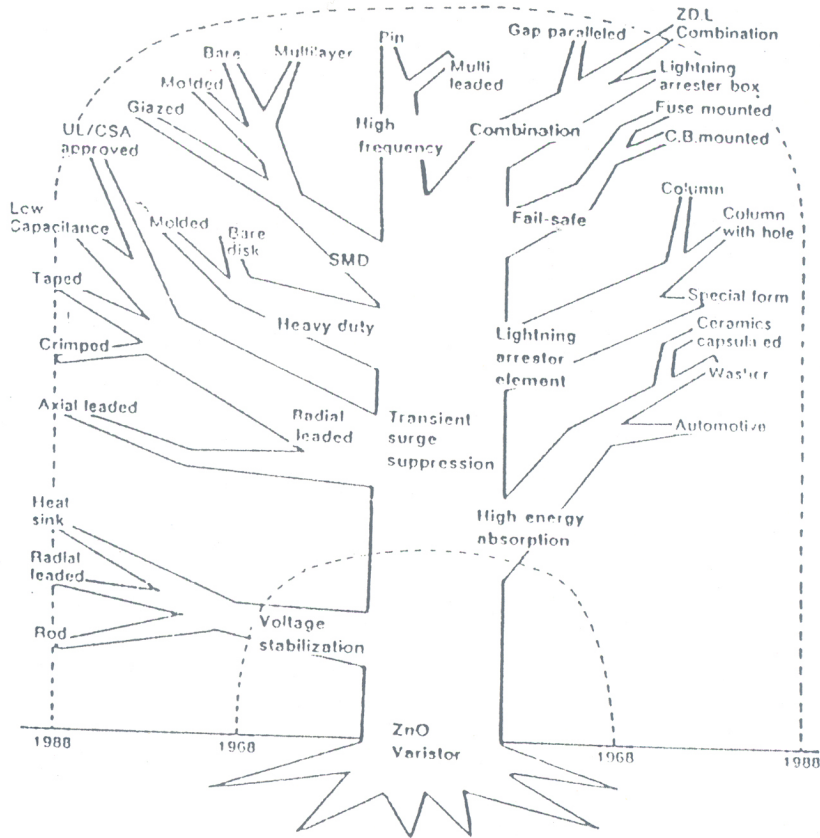


Fig. 1.13 Different application areas of a ZnO Varistor (47).

- 5) Power transmission : Station arrestors, capacitors, transmission lines.
- 6) Transportation : Automotive, Railway power signals etc.
- 7) Data processing : Computer, remote controls etc.

The exhaustive list of applications indicates that ZnO varistor can be utilized practically in every field of electrical devices that require absorption of abnormal voltages. Using the zinc oxide varistor, designers are able to increase the reliability of their circuit and at the same time reduce the consumer cost with more moderate power ratings. Considering the wide range of applications of these devices, there exists a tremendous market demand for this product. As per the world wide survey carried by Matsuoka [84], it is possible to indicate the yearwise requirement of these devices. Fig.1.14 gives an outline of this requirement during the last four decades.

To explain the functioning and the characteristics of these devices, many agencies and scientific organisations are contributing through publishing technical books and conducting workshops, seminars and symposia. Nationwide R&D projects are being undertaken to understand and develop these devices. The list of publications and various projects being undertaken at various levels are schematically outlined in Fig.1.15. This clearly indicates that to meet the ever increasing demand for these devices, tremendous efforts (money!) are

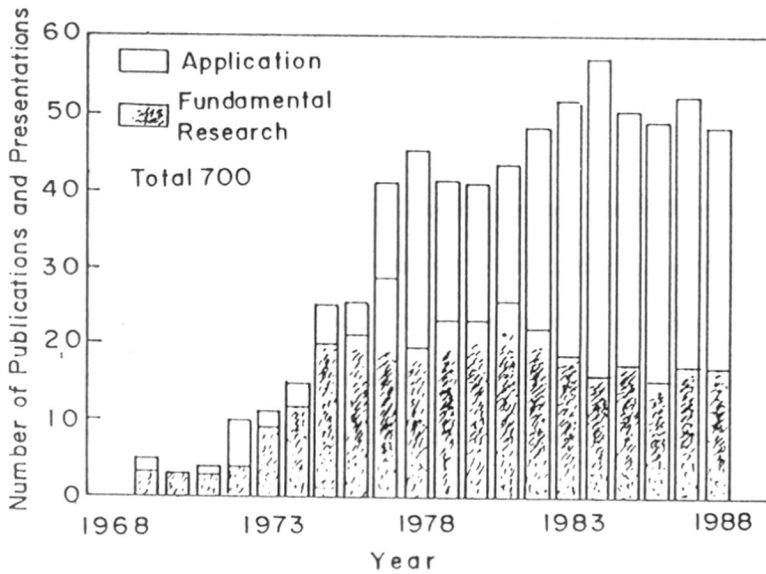


Fig. 1.14 List of publications and various projects being undertaken at various levels (84)

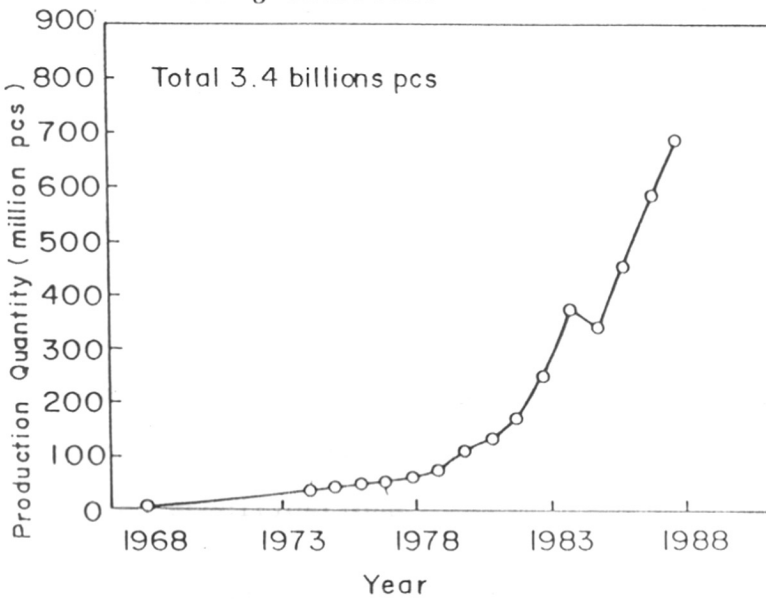


Fig. 1.1 Yearwise requirement of ZnO varistors (84)

being made all over the world during last 2-3 years. Hundreds of technical/research papers are reported including the proceedings of second international varistor conference held at General Electric Corporation Research & Development Centre, Schenectady, New York, in 1988.

#### 1.16 **Fabrication/Developmental Methods of ZnO Varistors**

Zinc oxide (ZnO) based varistors are being widely manufactured/fabricated by mixed oxide solid state (chemical) route through sintering ceramic process, involving very minutely monitored steps [25,26,44,84] like:

- (1) High purity zinc oxide and other constituents are mixed thoroughly by milling in wet ball mill.
- (2) The mixed powder is dried and pressed to the desired shape (green compacts).
- (3) The resulting pellets are sintered at high temperatures in a controlled atmosphere.
- (4) The sintered compacts are electroded often with a fired silver contacts.
- (5) Leads are attached by solder and the finished device is encapsulated in a polymeric material and tested to meet the desired specifications.

In addition to the above method many researchers have carried out experimental work on other methods like (i) coprecipitation, evaporation, suspension and solution;

(ii) chemical route of precursor powders and; (iii) sol-gel processing etc. All these methods have their own advantages and disadvantages over the other and are discussed earlier. Considering the wider requirements of these devices, the progress in fabrication of these devices are increasing rapidly. The progress in fabrication technology for the last two decades is summarised by Eda [247] as given in Table-1.7. It is possible to classify the progress in three groups: (i) surface type, (ii) a bulk type and (iii) a junction type. In addition to the above methods Eda and his group [247] had studied some of the novel fabrication methods for the fabrication of the varistors. These methods along with their comparative performance parameters are given in Table-1.8. It is clear from the table that the Host-Guest method gives the better performance properties and this method is supposed to be an example to assess the controlled nanometer varistor compositions.

#### 1.17 Future Trends of ZnO Varistors

The overview has shown the widespread applications of ZnO varistors. There is no theoretical argument to affirm that ultimate characteristics have been activated. At present, much work is being actively carried out in the field of powder technology and configuration of the components.

Table-1.7

Year	Surface Type	Bulk Type	Junction Type
1968	•Sint. ZnO with Ag electrode (Matsuoka)	•ZnO-Bi,Co,Mn,Sb (Matsuoka)	
1969-75		•Discovery of additives:Ba,Sr,B,Cr,Si,Sn, Ti,Be,Ni,B,F,Al,Ga,Ag,glass frit (Matsuoka)	
1973		•ZnO-Pr (Mukae)	
1974-75		•Heat-treatment (Iga)	
1976		• <u>Seed grain method (Eda)</u>	
1977		•Cold-isostatic-pressing (CIP)(Eda)	
1978		•Thick film with glass (Eda)	
1979		•Stacked-type (Shohata)	
1980	•Surface diffusion (Selin)		*MO sandwiched bet. single
1981	•Hot-pressing (Snow)		crystal ZnO (Schwing)
1981	•Microwave sintering (Brooks)		
1982		• <u>Thin film bulk type (Eda)</u>	
1983			* <u>Sput. MO on sint. ZnO(Eda)</u>
1984	•Sol-gel (Lauf)	•HIP (Takada)	
1984	• <u>Thick film by plasma-spray (Eda)</u>		*MO sandwiched bet. sint. ZnO(Eda)
1985	•Laser fabrication of electrodes (Modine)		
1985	•Thick film with glass (Chiou)		
1986	•Ion implantation (Sonder)		
1986	•Urea processing (Sonder)	•HIP (Kostic)	
1987	•EDS method (Ivers-Tiffée)		
1987	•Vapor phase oxidation of Zn metal (Suyama)		*Sput. ZnO-Bi <sub>2</sub> O <sub>3</sub> (Suzuoki)
1988	• <u>Host-guest (Eda)</u>		

- 1) Names of a main contributor are shown.
- 2) Sint.: sintered, MO: metal oxide, sput.: sputtered, bet. : between.

**Table-1.8: Comparative Parameters Achieved by Different Fabrication Methods [247]**

Name of the Method	Nonlinear coeff. ( $\alpha$ )	Breakdown electric field (V/mm)
Seed Grain Method	> 30	8
Thin Film Method	15	830
Thick Film Method	40	600
Host Guest Method	52	100-1000

(a) New Powder Technology

ZnO varistor exhibits highly nonlinear current-voltage (I-V) characteristic owing to electrostatic barriers located at the grain boundaries. Electrical characteristics are correlated with distribution of these barriers in the volume of the ceramic and the homogeneity of the grain size. The better homogeneity of the barrier distribution signifies better performance of the ZnO varistor. The ideal case corresponds to the localization of a potential barrier for each boundary which is not the reality under conditions prevailing in the preparation of powder by the conventional steps of mixing and milling of the elements.

In order to improve homogeneity of the barrier distribution it is believed that on an atomic scale, powder preparation by a chemical method will provide a better homogeneity of additives at the ZnO/ZnO grain

boundary and a better grain growth control. Moreover, reproducibility from batch to batch should be improved and the yield consequently increased. The main advantage of chemical preparation techniques are the high degree of chemical homogeneity, chemically pure powders and well defined and uniform grain size. However, these methods possess certain disadvantages like, (i) particle aggregation in the case of extremely fine powder and; (ii) the cost of these methods.

Several chemical methods have been reported in the literature. Dosch et al. have developed a method of producing ZnO varistors with fine grains for high voltage applications [249]. The elements are coprecipitated as hydrous oxides, converted to oxalates which are calcined and Bi is precipitated on the surfaces of the oxides by a localized hydrolysis reaction.

Djega-Mariadasson from Paris University used simultaneous coprecipitation of all elements in a defined ratio throughout the process. The precursors are nitrate or tartrate solutions introduced into a presaturated solutions [250].

Seitz et al. from Siemens used the technique of evaporative decomposition of solutions. Powders were prepared from acetate or nitrate solutions [251]. Recently Hohenberger et al. [252] have reported sol-gel method for the preparation of ZnO varistor using acetate solution of



Zn, Co, Mn, Sb, Cr and Bi nitrates and shown that the method gives better homogeneity in the functional microstructure.

Electrical characteristics of ZnO varistors obtained with these methods are at the moment not really better than those corresponding to the conventional method. Moreover, the reproducibility and yield aspects are not yet well known.

At present, it is too early to say whether the chemical method will give better results than the conventional method. If this is the case, the cost of the precursors and the process parameters must remain compatible with the cost of varistor manufacture [86].

*CHAPTER-2*

**EXPERIMENTAL TECHNIQUES**

## 2.1 Introduction

This chapter describes the various experimental techniques employed for synthesis, physico-chemical and electrical characterization of the ZnO based electronic ceramic sensors. The experimental work was divided into three parts:

- (1) Synthesis of active powders comprising of selection of high purity raw materials, mixing, wet ball milling, compacting and sintering, etc. [253-255].
- (2) Physico-chemical characterizations comprising of density, phase, microstructure and surface analysis, etc. [256-259].
- (3) Electrical characterizations comprising of current-voltage (I-V) measurements at room temperatures and AC impedance measurements at various temperatures [260-261].

## 2.2 Solid State (Chemical) Synthesis of Active Powders

A large number of varistor compositions were synthesized using solid state chemical route involving very minutely monitored steps. Fig.2.1 represents flow chart followed for the preparation of active powders of the ZnO based varistors. In order to formulate the varistor composition, high purity AR grade of ZnO (M/s May & Baker Ltd., England) was used as a major constituent. The  $\text{Bi}_2\text{O}_3$ ,  $\text{MnO}_2$  and  $\text{Co}_2\text{O}_3$  were used as dopants (M/s Loba Chem., Bombay and E. Merk A.G., Darmstadt, Germany). The basic system<sup>is</sup> comprising of 97 mol%

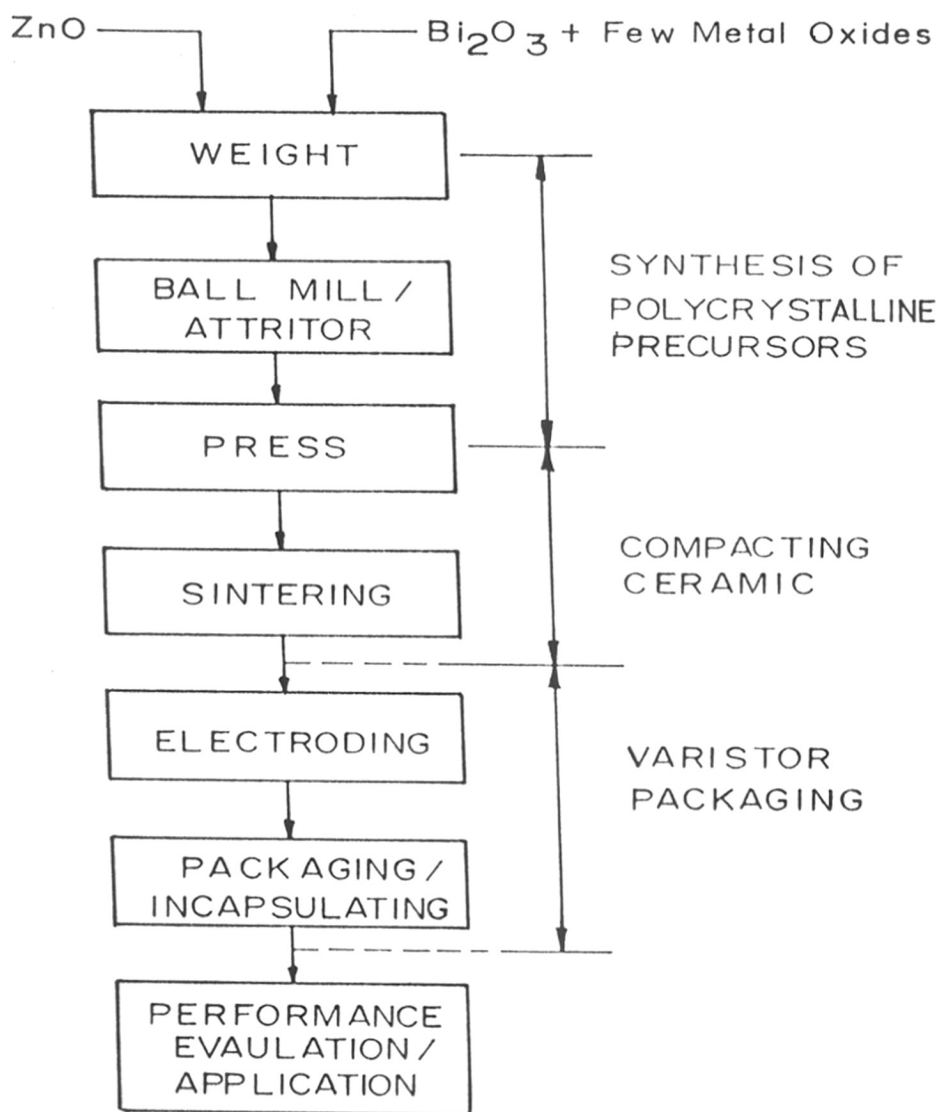


Fig. 2.1 Solid State (Chemical) Synthesis route for ZnO based varistors.

ZnO and 1 mol% each of Bi<sub>2</sub>O<sub>3</sub>, Co<sub>2</sub>O<sub>3</sub> and MnO<sub>2</sub> respectively. The composition was abbreviated as ZBCM and considered as a basic varistor system.

The powders were thoroughly mixed in a desired proportions (a batch of 300 gms) and wet ball milled in a plastic container using isopropyl alcohol for about 10-12 hours. The glass balls were used as a grinding media. A laboratory ball mill (M/s Lawkim Ltd., Bombay) of 1440 RPM (frequency) was used for this purpose. The homogeneously mixed powders were dried for 8-10 hours in a temperature controlled oven (M/s W. Memmert Schwabaih, U.K.) between 50-70°C. Few grams of homogeneously mixed powder were kept aside to record X-ray diffractograms on physical mixture. The remaining powder (mixture) was mixed with 2% Polyvinyl Alcohol (PVA) as a binder to impart sufficient green strength in a compacted sample/pellet. The mixture was then dried suitably under the IR (infra red) 230V, 250 watt lamp (M/s Philips India, Bombay). The mixture was subsequently pressed into a disc form having diameter  $\approx$  12 mm and thickness  $\approx$  1.5 mm using three tier steel die. The pellets were pressed at a pressure of 200 kg/cm<sup>2</sup> using a laboratory hydraulic press (M/s Anchor Hydraulics Ltd., Bombay). The pellet was removed from the die by applying a pressure in the reverse direction with great care. The density of the green pellets was measured from the weight, diameter and thickness of each pellet.

### 2.3 Sintering

The green pellets along with physical mixture were placed on a alumina plate. They were air sintered at different temperatures ranging from 900-1300°C (in eight steps of 50°C each) for one hour duration in a electric chamber furnace (M/s Okay Electric Furnace, Calcutta) with silicon carbide heating elements. To attain the desired sintering temperature, furnace was initially heated at a rate of 100°C/hour upto 700°C. The rate of heating was reduced to 50°C/hour between the temperature range of 700-900°C in order to prevent the possible stresses and cracks in the pellets/samples due to shrinkage. Above 900°C, samples were again heated at the rate of 100°C/hour up to desired temperature. The furnace was switched off and allowed to cool at its own rate to room temperature.

### 2.4 Physico-chemical characterization

During the synthesis, these active powders were characterized at various stages of developments like after mixing, pressing, sintering, etc. Following are the techniques used to characterize these powders.

#### (a) Density

The densities were calculated for green and dense compacts to understand the effect of sintering temperatures. To measure the density, sintered pellets were uniformly lapped using carborundum powder (400 mesh)

on both the sides. The density was then calculated from the weight and the dimension of each pellet/sample. The density was calculated on 3-4 samples of the same batch and an average value was taken. For a given batch, variation in density from sample to sample was found within  $\pm 1.5\%$ .

(b) Phase Analysis

X-ray diffractograms (XRD) of the polycrystalline active powder of a physical mixture and the powder sintered at different temperatures were recorded on Philips X-ray Diffractometer (Model PW 1730) using CuK $\alpha$  radiation ( $\lambda = 1.5403\text{\AA}$ ) with Ni filter for identification of complex phases developed during synthesis. The X-ray diffractograms so obtained were compared with XRD pattern of pure ZnO (used in composition) <sup>recorded with the same setup</sup> and with the standard ASTM data.

(c) Microstructural Analysis

Microstructural analysis studies were carried out using Cambridge Stereoscan Scanning Electron Microscope (SEM) Model-150 for the identification of grains, grain boundaries and microscopic behaviour of the sintered compacts. The grain size was calculated by counting the number of grain boundaries intercepted by a line of known length and taking the average of 6-8 such measurements randomly made across the photomicrographs.

(d) Surface Analysis

X-ray photoelectron spectroscopic (XPS) analysis/studies were carried out using Commercial Vacuum Generator ESCA-3, MK-II instrument at a base pressure of  $10^{-8}$ - $10^{-9}$  Torr with MgK $\alpha$  (1253.6 eV) radiation source for the analysis of the microscopic structure and migration of Bi<sub>2</sub>O<sub>3</sub> from ZnO grain surface of different varistor compositions sintered at various temperatures.

(e) Electroding

For electrical measurements, lapped pellets were electroded on both the sides using room temperature drying silver paint. Care was taken to maintain the electroded area  $\leq$  8 mm on both the surfaces so as to avoid electrical short circuiting effect during measurements. Final dimensions of the pellets were 0.9-1.0 mm thickness and 10 mm diameter.

(f) DC Current-Voltage Characterization

The room temperature DC current-voltage (I-V) characteristics were measured on the sintered samples using Keithley Electrometer (Model 610C) and Aplab stabilised DC power supplies (Model-7161 and 7323). The experimental set-up is shown in Fig.2.2. These measurements were carried out up to the current range of 1 mA so that the measurement was not affected by the heating (Joule effect). The breakdown electric field  $E_b(1\text{mA}/\text{cm}^2)$  and nonlinearity coefficient  $\alpha$  were



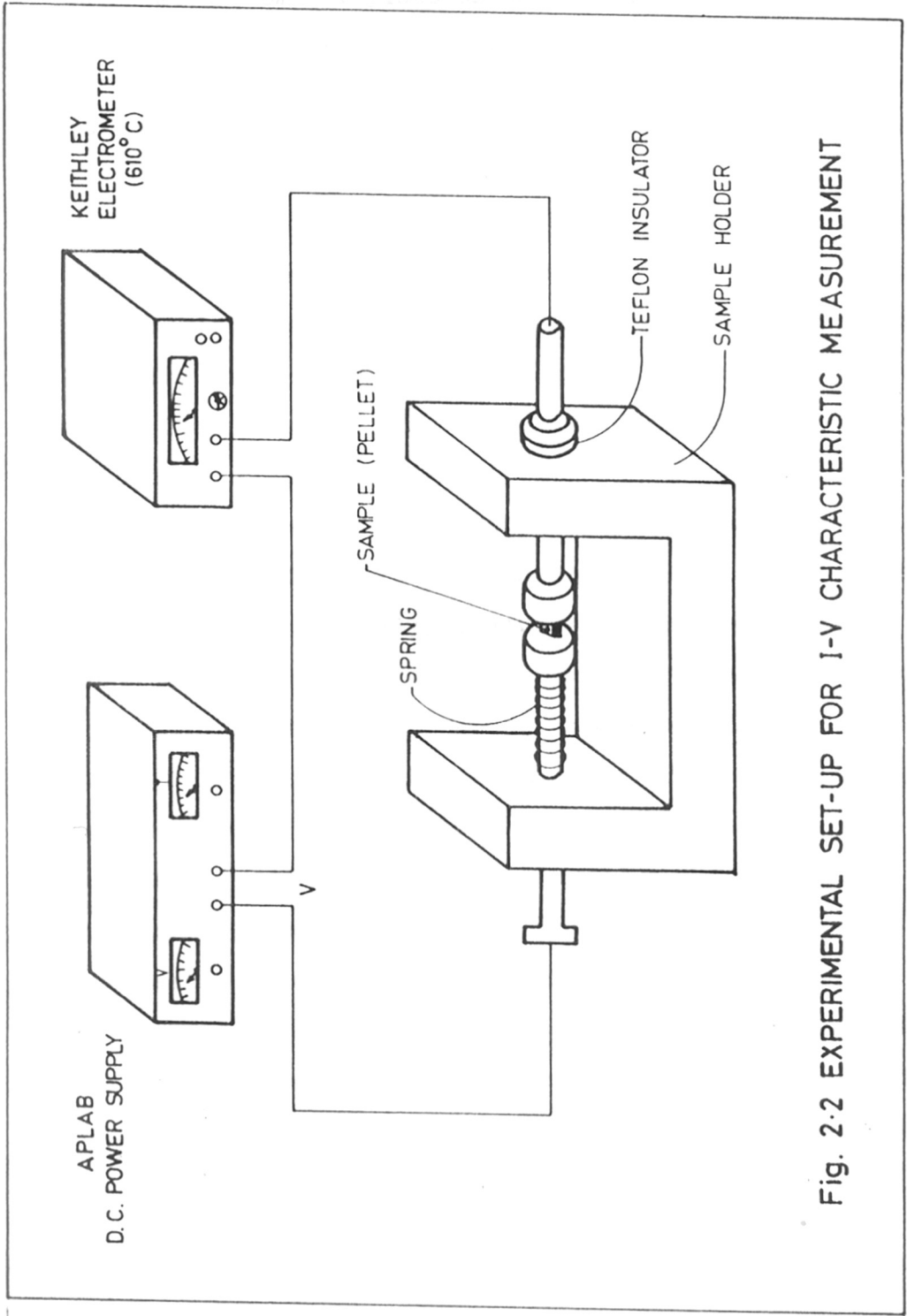


Fig. 2-2 EXPERIMENTAL SET-UP FOR I-V CHARACTERISTIC MEASUREMENT

calculated from I-V plots using the equations (1.1), (1.2) and (1.3) as given in chapter-1.

(g) AC Impedance Characterization

For AC impedance measurements, pellets of  $\approx 10$  mm diameter and  $\approx 0.9$  mm thick were used. For each measurements, a pellet was sandwiched between two spring loaded platinum electrodes provided in a specially made rig. The rig assembly was then inserted in a temperature controlled furnace ( $\pm 1^\circ\text{C}$ ). AC impedance data was recorded in the temperature range of 25-250°C over the frequency range of 1Hz-10MHz using computer controlled Solartron 1260 impedance analyser. For complex data analysis, Boukamp [262] software package was used. The maximum temperature 250°C was used for the study taking into consideration the thermal stability of rig material. Fig.2.3 gives the block diagram for AC impedance measurements. These measurements were carried out to establish the equivalence between functional and electrical microstructures developed during the synthesis. The varistor performance was modeled by electrical equivalent circuits, and lumped/immittance parameters were calculated. From the temperature studies (Arrhenius plots) activation energies across the each network (resistive) elements were calculated.

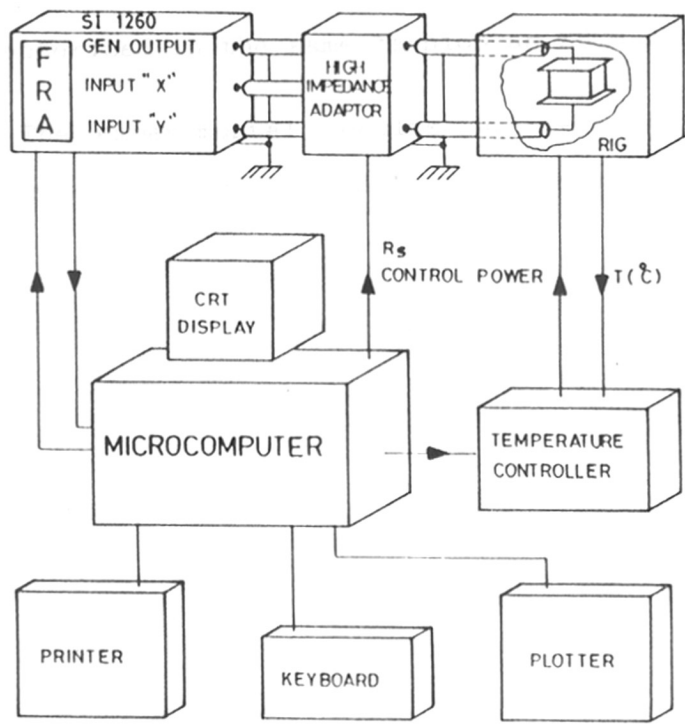


Fig. 2.3 Experimental Layout for AC impedance measurements.

## 2.5 Modification of ZBCM Varistor System

After the confirmation of varistor properties in a basic ZBCM varistor system, five batches of 300 gm each were prepared using 5,10,15 and 20 mol% of MgO. These batches were abbreviated as ZBCM-5MgO, ZBCM-10MgO, ZBCM-15MgO and ZBCM-20MgO respectively. The modified varistors were synthesized, processed and subsequently characterized in the same fashion as ZBCM varistor.

The experimental results on these varistor systems are presented and discussed in the subsequent chapters 3 and 4.

*CHAPTER-3*

**RESULTS AND DISCUSSION**

### 3.1 Introduction

Zinc oxide (ZnO) based varistors consist of (i) conductive zinc oxide grains, (ii) electrically insulating grain boundaries and intergranular network containing additives like  $\text{Bi}_2\text{O}_3$ ,  $\text{Co}_2\text{O}_3$  and  $\text{MnO}_2$  etc. The electrical properties of these devices are primarily influenced by (i) double schottky barriers located in the region of ZnO grains and intergranular layers [25,26,62,83] as discussed in chapter-1 and; (ii) are determined by their detailed "functional microstructure" developed during the processing stages and varies with processing parameters. Two important performance parameters are, (i) nonlinear coefficient ( $\alpha$ ) and; (ii) breakdown electric field ( $E_b$ ), generally specified at a current density of  $1\text{mA}/\text{cm}^2$ . Required value of ( $E_b$ ) is obtained by either optimising the varistor thickness and the grain size related microstructure of the dense compacts. To achieve the required control over the grain size, we used magnesium oxide (MgO) as a grain growth inhibitor in a basic varistor system comprising of ZnO,  $\text{Bi}_2\text{O}_3$ ,  $\text{Co}_2\text{O}_3$  and  $\text{MnO}_2$  (abbreviated as ZBCM). For example, concentrations of 5,10,15 and 20 mol% MgO (abbreviated as ZBCM-5MgO, ZBCM-10MgO, ZBCM-15MgO, ZBCM-20MgO) were used to study the effect of processing parameters in evolving the high quality functional microstructure leading to the improved performance parameters.

In this chapter, we present the results on, (i)

current-voltage (I-V) characteristics (measured at room temperature) and; (ii) the various physico-chemical characterizations, as a function of sintering temperatures.

### 3.2 Current-Voltage (I-V) Characteristics

The I-V characteristics on all the five varistor systems were measured at room temperature as a function of sintering temperatures using the experimental set-up given in chapter-2. Figs.(3.1-3.5) show the I-V characteristics plotted in a log scale for these five varistor systems. The values of nonlinearity coefficient ( $\alpha$ ) and breakdown electric field ( $E_b$ ) were calculated using empirical equations (1.1), (1.2) and (1.3) given in chapter-1. The values of ( $\alpha$ ) were calculated over the current range of  $5\mu\text{A}$ - $1\text{mA}$  and  $E_b$  at  $1\text{mA}/\text{cm}^2$ . These values are summarised in Table-3.1. It is seen that ZBCM-10MgO varistor system shows the improvement in the performance parameters e.g. higher breakdown electric field with almost same nonlinear coefficient in comparison with ZBCM varistor system under the identical processing conditions. To understand the improvement in the performance parameters, in depth I-V characteristic studies as a function of sintering temperature on these two (ZBCM & ZBCM-10MgO) varistor systems were performed and the results are presented in the following sections.

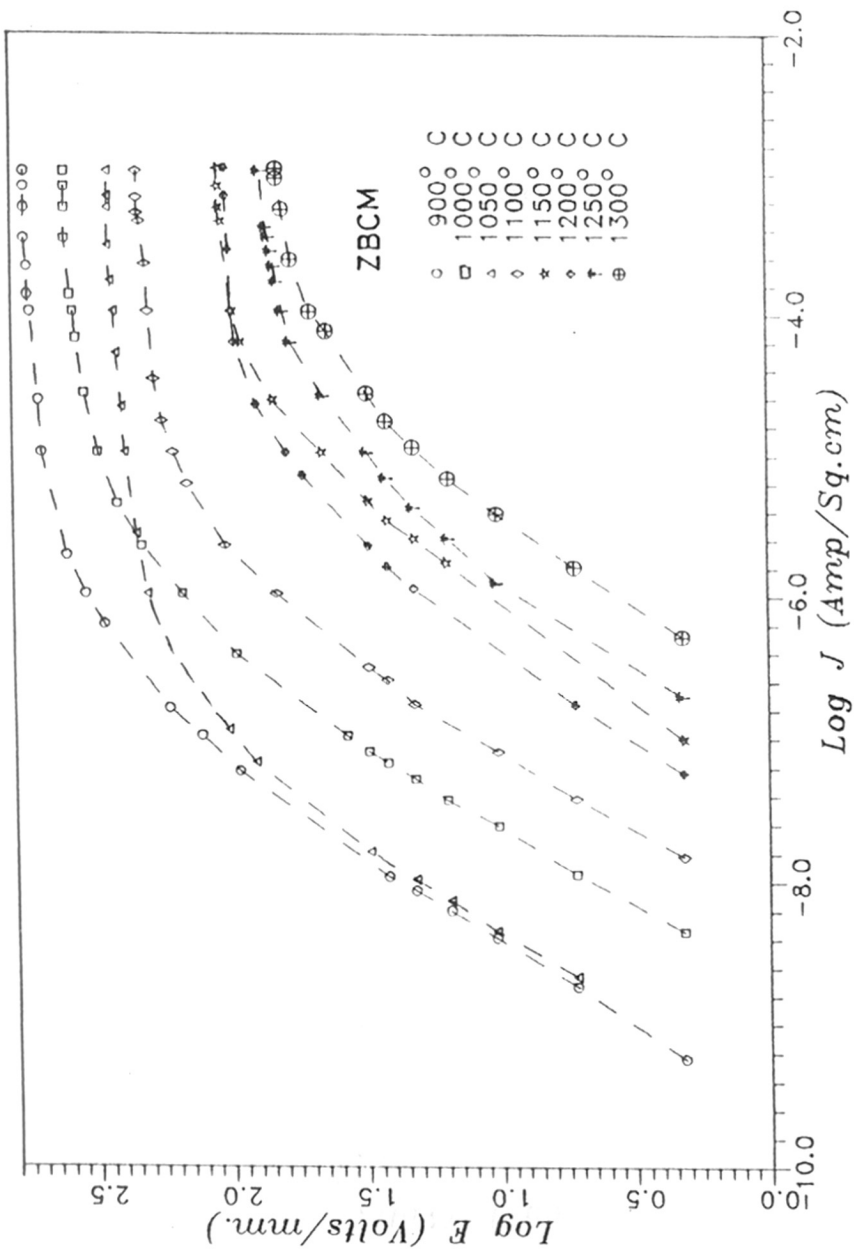


Fig. 3.1 Current-voltage (I-V) characteristics of ZBCM varistor sintered at different temperatures.



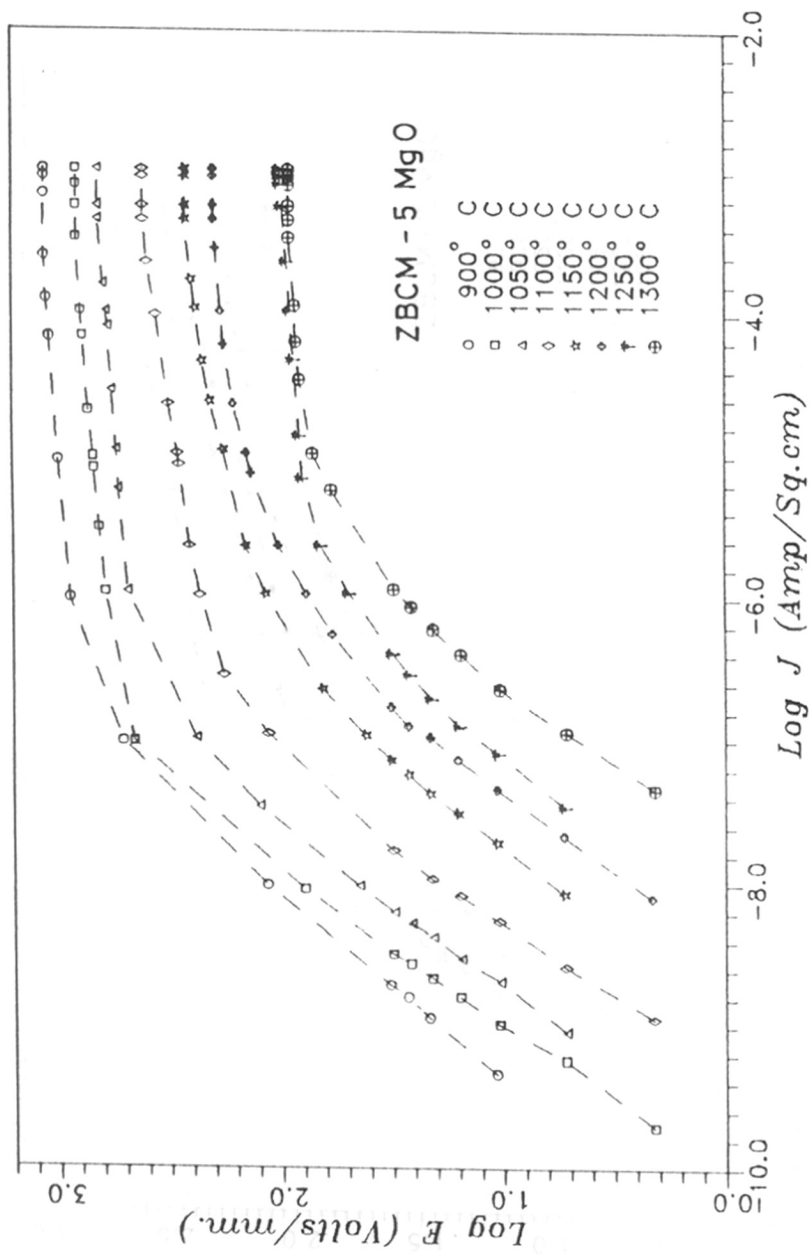


Fig. 3.2 Current-voltage (I-V) characteristics of ZBCM-5MgO varistor sintered at different temperatures.

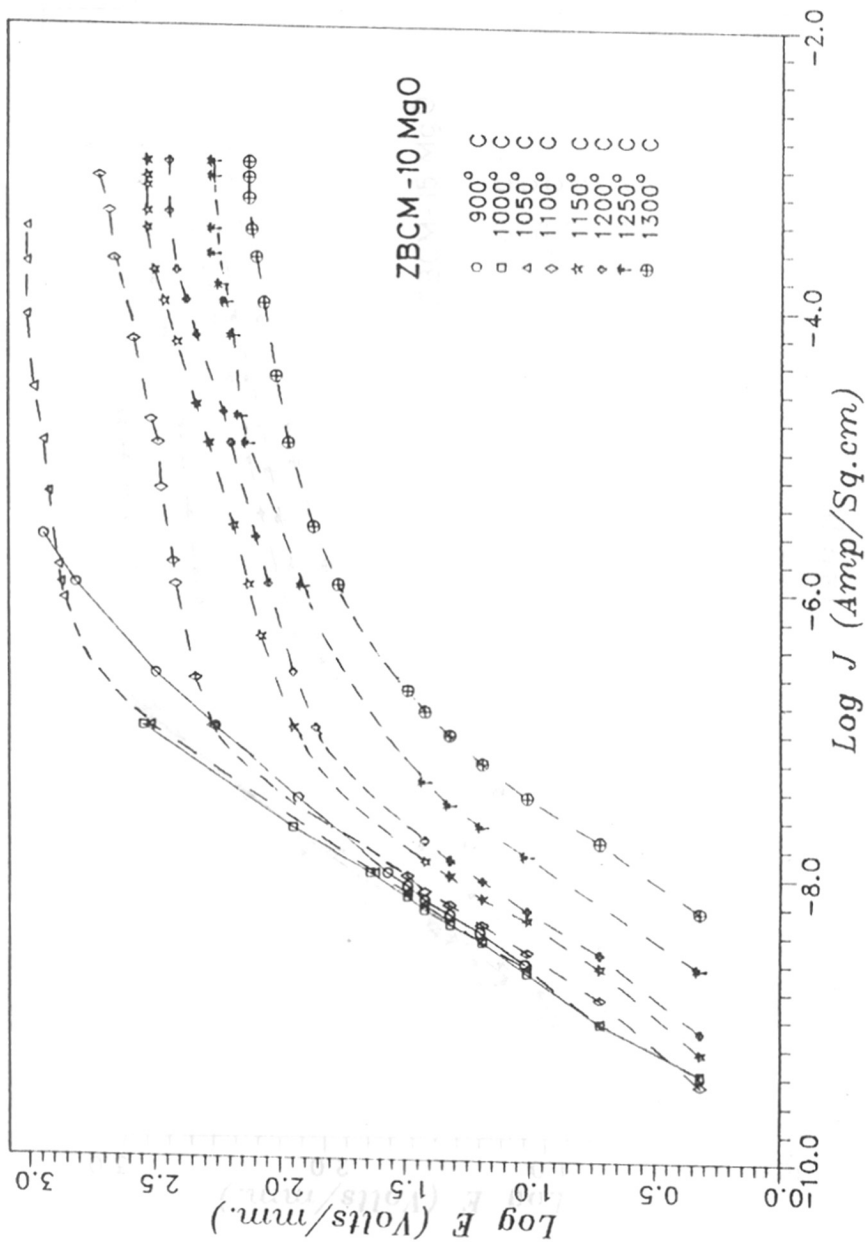


Fig. 3.3 Current-voltage (I-V) characteristics of ZBCM-10MgO varistor sintered at different temperatures.

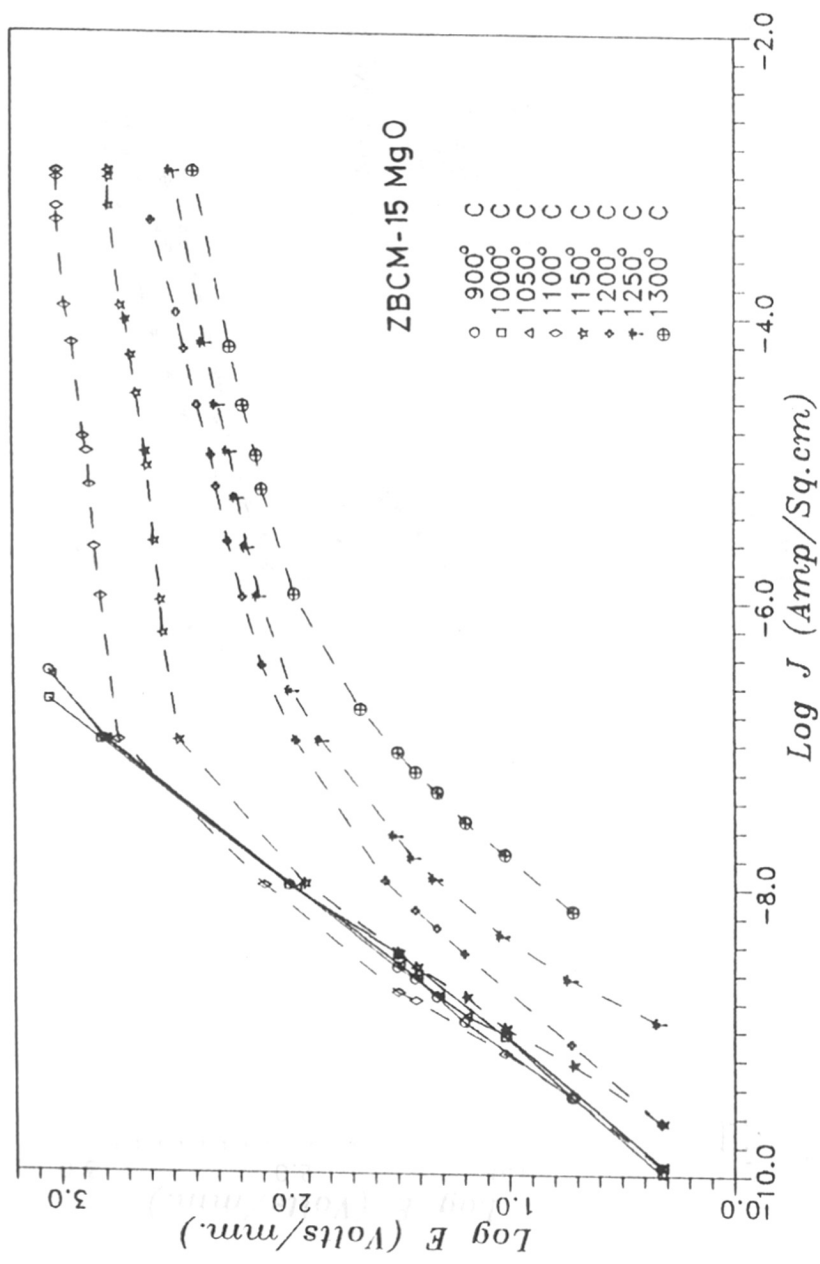


Fig. 3.4 Current-voltage (I-V) characteristics of ZBCM-15MgO varistor sintered at different temperatures.

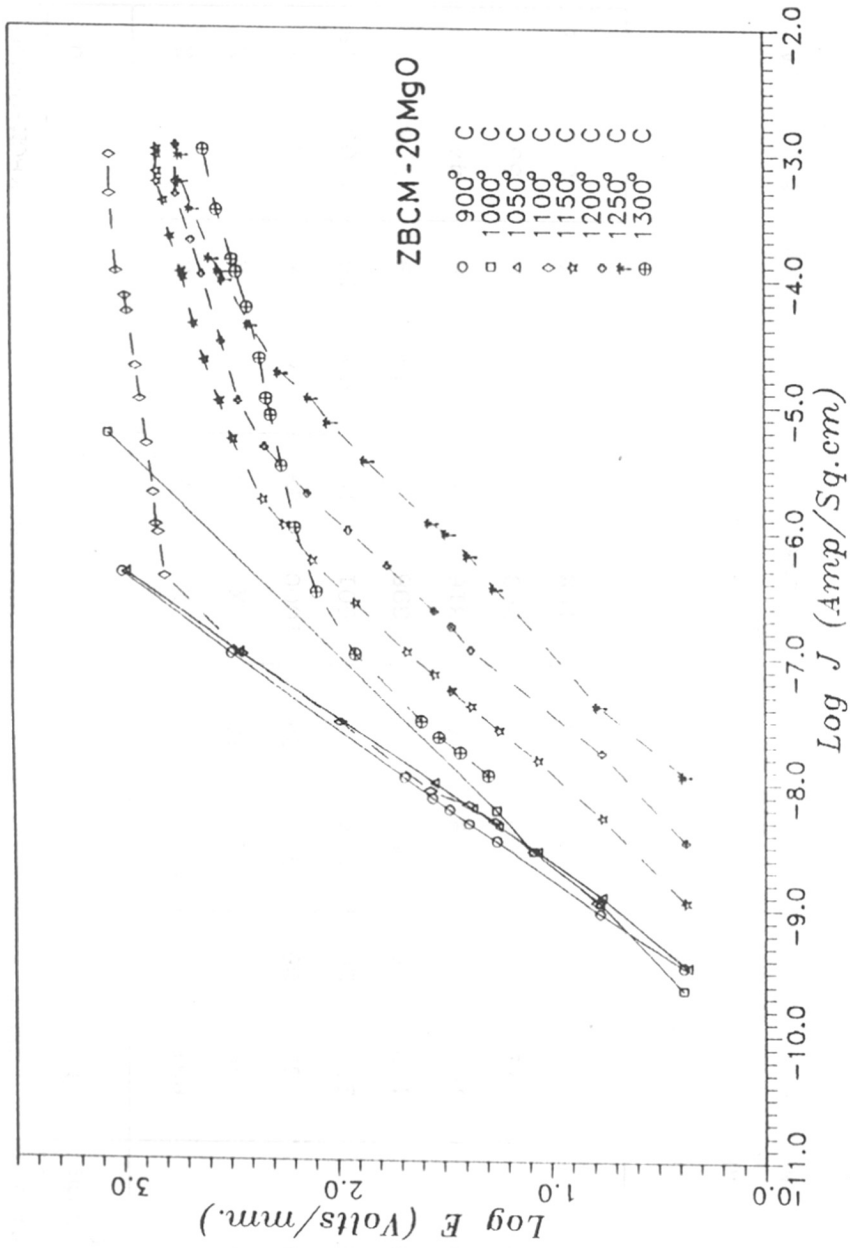


Fig. 3.5 Current-voltage (I-V) characteristics of ZBCM-20MgO varistor sintered at different temperatures.

Table 3.1: Breakdown electric field & nonlinearity coefficient of different varistor systems sintered at different temperatures

Composition Sint. temp. °C	ZBCM		ZBCM-5MgO		ZBCM-10MgO		ZBCM-15MgO		ZBCM-20MgO	
	Eb	$\alpha$	Eb	$\alpha$	Eb	$\alpha$	Eb	$\alpha$	Eb	$\alpha$
900	631	10	1258	12	X	X	X	X	X	X
1000	398	20	1122	18	X	X	X	X	X	X
1050	282	36	708	24	1000	29	X	X	X	X
1100	224	20	354	12	501	10	1000	18	1000	18
1150	119	8	282	7	398	7	630	9	708	5
1200	106	7	199	6	316	5	447	6	447	3
1250	71	6	100	6	200	3	316	5	398	2
1300	63	6	89	4	168	3	251	4	316	2

Error of measurements- Voltage: 0-30V =  $\pm 0.001V$ ; 50-1000V =  $\pm 0.2V$ .  
Current: 0.01 Amp.

- X - Absence of nonlinearity (linear behaviour).
- Eb - Breakdown electric field at  $1mA/cm^2$ .
- $\alpha$  - Nonlinearity coefficient calculated over the current range of  $5\mu A-1mA$ .

### 3.3 Current-Voltage (I-V) Characteristics of ZBCM Varistor System

Fig.3.1 shows the current-voltage (I-V) characteristics of the ZBCM varistor system sintered at different sintering temperature (900-1300°C/1hr) plotted in log-log scale. It is seen that:

(i) An ohmic/prebreakdown region having nonlinear coefficient  $\alpha \approx 1$  at low voltages and the current flowing is given by  $I \propto V$ .

(ii) A nonohmic/breakdown region having large nonlinear coefficient ( $\alpha \geq 1$ ) at higher voltages and the current flowing is given by the empirical equation  $I = (V/C)^\alpha$ .

(iii) The upturn region is not recorded as the I-V measurements were limited to 1mA current to avoid the Joule heating and electrical short circuiting of the pellets/samples.

(iv) The plots show that there is a similar behaviour as a function of sintering temperatures.

(v) In the prebreakdown region, the leakage current at constant voltage increases monotonically with the increase of sintering temperature due to decrease in the electrical resistance of the dense compacts.

(vi) In the breakdown region, the voltage at constant current decreases monotonically and region becomes narrow with the increase of sintering temperature.

The values of nonlinear coefficient and breakdown electric field were calculated as a function of sintering

temperature and are summarised in Table-3.2.

**Table-3.2:**  $E_b$  and  $\alpha$  values of ZBCM varistor system sintered at different temperatures.

Sint. temp. ( $^{\circ}\text{C}$ )	900	1000	1050	1100	1150	1200	1250	1300
$E_b$ (V/mm)	631	398	282	224	119	106	71	63
$\alpha$	10	20	36	20	8	7	6	6

The table shows that, (i) the breakdown electric field decreases as a function of increase in sintering temperature e.g.  $E_b(900) \approx 631\text{V/mm}$ ,  $E_b(1000) \approx 398\text{V/mm}$ ,  $E_b(1050) \approx 282\text{V/mm}$ ,  $E_b(1100) \approx 224\text{V/mm}$ ,  $E_b(1150) \approx 119\text{V/mm}$ ,  $E_b(1200) \approx 106\text{V/mm}$ ,  $E_b(1250) \approx 71\text{V/mm}$  and  $E_b(1300) \approx 63\text{V/mm}$  respectively. (ii) The nonlinear coefficient ( $\alpha$ ) initially increases with the increase in sintering temperature from 900-1050 $^{\circ}\text{C}$  e.g.  $\alpha(900) \approx 10$ ,  $\alpha(1000) \approx 20$ ,  $\alpha(1050) \approx 36$  respectively, and; (iii) when sintering temperature increased beyond 1050 $^{\circ}\text{C}$ , the  $\alpha$  value decreases with the increase in sintering temperature e.g.  $\alpha(1100) \approx 20$ ,  $\alpha(1150) \approx 8$ ,  $\alpha(1200) \approx 7$ ,  $\alpha(1250) \approx 6$  and  $\alpha(1300) \approx 6$  respectively. The observed variation in the breakdown electric field and nonlinearity coefficient as a function of sintering temperature agree well with the earlier observations of many researchers [25-26,42,68,81-83,85-86,13,239]. These results show that ZBCM pellets sintered at 1050 $^{\circ}\text{C}/1\text{hr}$  exhibiting highest nonlinear coefficient ( $\alpha \approx$

36) with breakdown electric field  $E_b \approx 282\text{V/mm}$ . This temperature is found to be the optimum temperature for sintering of compacts. The values of  $(\alpha)$  and  $(E_b)$  of our ZBCM system are better than the values reported by Smith et. al. [42] for an identical composition [ $\alpha_{(1100)} \approx 15$  and  $E_{b(1100)} \approx 90\text{V/mm}$ ].

To understand the improvement in the nonlinear behaviour as a function of sintering temperature, extensive physico-chemical characterizations of active and sintered powder/pellets were carried out in our laboratory.

(a) Density Analysis

The densities of the sintered compacts were calculated as a function of sintering temperatures using the method described in chapter-2. The density of the green compact was also calculated for reference purpose. The experimental results are summarised in Table-3.3.

Table-3.3: Density ( $\rho$ ) of ZBCM varistor system sintered at different temperatures.

Sint. temp. ( $^{\circ}\text{C}$ )	PM	900	1000	1050	1100	1150	1200	1250	1300
$\rho$ (gm/cc)	3.75	5.11	5.18	5.44	5.29	5.15	4.83	4.82	4.80

Error of measurement- Mass:  $\pm 0.001$  gm, Dimension:  $\pm 0.01$  mm.



The effect of sintering temperature on density can be easily seen from the table. The density of a green compact of a physical mixture is  $\rho_{(PM)} \approx 3.75 \text{ gm/cc}$ , which is  $\approx 66.96\%$  of the theoretical density of pure ZnO ( $5.606 \text{ gm/cc}$ ). The density increases with the increase of sintering temperature initially in the temperature range of  $900\text{--}1050^\circ\text{C}$  e.g.  $\rho_{(900)} \approx 5.11 \text{ gm/cc}$ ,  $\rho_{(1000)} \approx 5.18 \text{ gm/cc}$ ,  $\rho_{(1050)} \approx 5.44 \text{ gm/cc}$  respectively. When the sintering temperature increases beyond  $1050^\circ\text{C}$  and till  $1300^\circ\text{C}$ , the density decreases with the increase of sintering temperature e.g.  $\rho_{(1100)} \approx 5.29 \text{ gm/cc}$ ,  $\rho_{(1150)} \approx 5.15 \text{ gm/cc}$ ,  $\rho_{(1200)} \approx 4.83 \text{ gm/cc}$ ,  $\rho_{(1250)} \approx 4.82 \text{ gm/cc}$  and  $\rho_{(1300)} \approx 4.80 \text{ gm/cc}$ . The density of a pellet/dense compact when sintered at  $1050^\circ\text{C}$ , shows the highest value, indicates the high degree of compactness. In other words,  $1050^\circ\text{C}$  is an optimum sintering temperature of ZBCM varistor system at which high degree of compactness is achieved in the dense compacts/pellets. The decrease in the density at higher sintering temperature is mainly due to the evaporation of  $\text{Bi}_2\text{O}_3$ . As evident from the equation, the density of a dense compact at a particular sintering temperature is given by

$$\text{Density } (\rho) = \frac{\text{Weight (mass)}}{\text{Volume}} \text{ gm/cc}$$

From the above equation, the decrease in density is possible only when there is a (i) weight loss of the

compact and/or; (ii) both weight loss and reduction in volume of the compact. It is worth to mention that all green compacts/pellets were pressed and sintered under identical conditions ( $250 \text{ kg/cm}^2$ ). The sintered compacts have shown that there is a negligible change (reduction/shrinkage) in volume ( $T > 900^\circ\text{C}$ ) and is almost identical for the pellets sintered at different sintering temperatures. Therefore the density is decreased only due to the weight loss of the compacts. This shows that evaporation of  $\text{Bi}_2\text{O}_3$  has taken place at higher sintering temperatures. The evaporation of  $\text{Bi}_2\text{O}_3$  in the ZnO based varistors at higher sintering temperatures has also been reported in the literature [26,29,62] and agrees with our observations.

(b) Phase Analysis by XRD

To identify the complex phases (if any) formed during the synthesis, powder X-ray diffractograms were recorded on active powder (physical mixture) and the powder sintered at different sintering temperatures. To identify the changes in the crystalline phases of pure ZnO during sintering, X-ray diffractograms were recorded for comparison. Fig.3.6 shows the X-ray diffractograms of pure ZnO, physical mixture (PM) and for the powder sintered at different temperatures. From the X-ray diffractogram of a pure ZnO, 'd' values were calculated and compared with standard data [263] as summarised in Table-3.4. The high intensity characteristic lines ( $I/I_1 = 71, 56, 100, 29, 40$  and  $35$ )

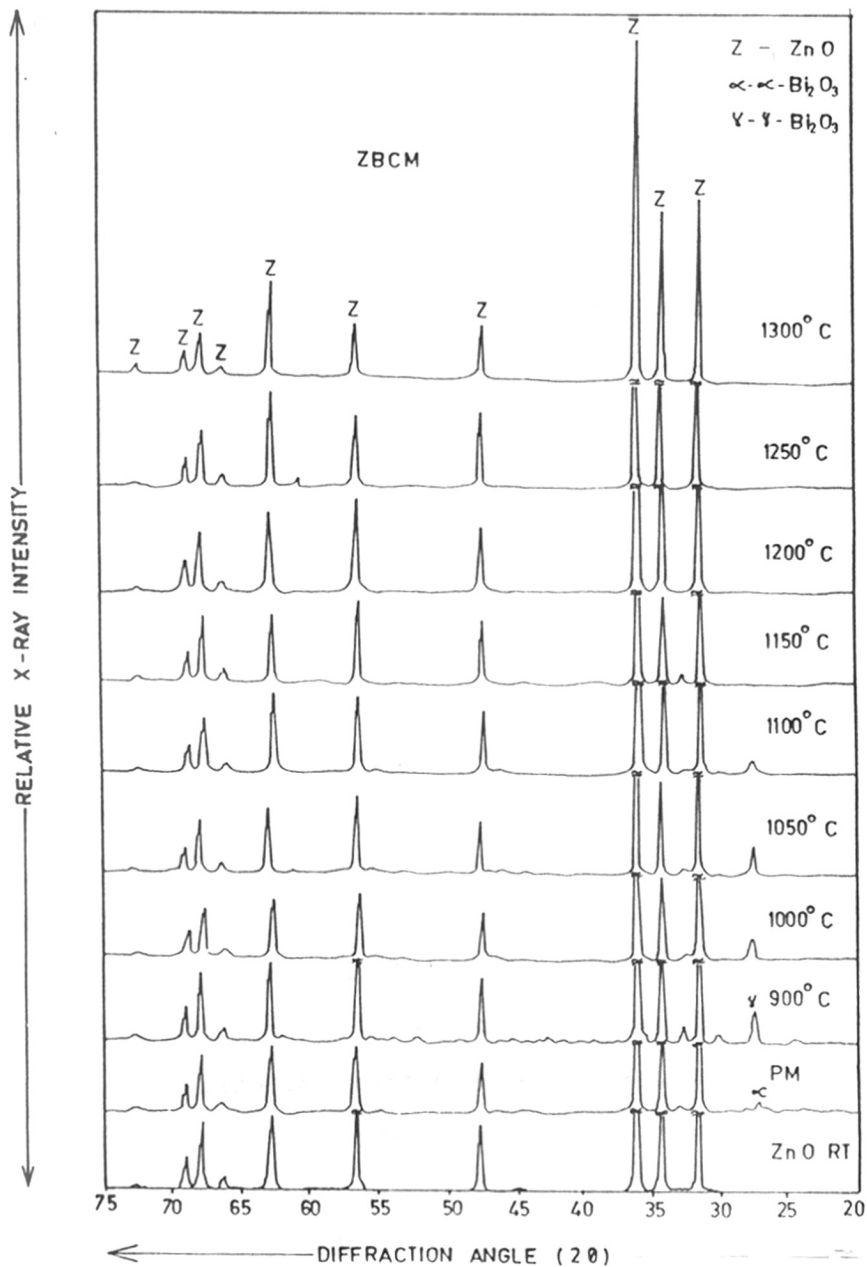


Fig. 3.6 Powder X-ray diffractogram (XRD) of Pure ZnO Physical Mixture and ZBCM powder sintered at different temperatures.

were used for comparison for the X-ray diffractograms of PM and powder sintered at different temperatures. The X-ray diffractogram of a physical mixture shows that all the characteristic lines marked in Table-3.4 are present along with the visible characteristic lines of  $\alpha$ - $\text{Bi}_2\text{O}_3$  (monoclinic)  $2\theta \approx 27.3, 33.1$  [264].

**Table-3.4:** 'd' values of ZnO characteristic lines [263]

d(A)	2.816	2.606	2.476	1.911	1.626	1.477	1.407	1.379	1.359	1.301
I/I <sub>1</sub>	71	56	100	29	40	35	6	28	14	3
2 $\theta$	31.74	34.44	36.24	47.54	56.55	62.86	66.38	67.92	69.92	72.6

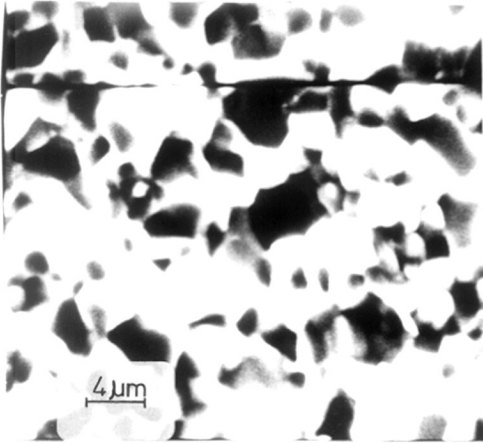
Error of measurements -  $2\theta = \pm 0.1^\circ$

The X-ray diffractogram recorded for the powder sintered at 900°C shows all characteristics of ZnO along with the visible characteristic line of  $\gamma$ - $\text{Bi}_2\text{O}_3$  (cubic)  $2\theta \approx 27.7, 32.77$  [265]. This shows that when a ZBCM powder sintered at 900°C/1hr, the phase transition has taken place in  $\text{Bi}_2\text{O}_3$  i.e.  $\alpha$ - $\text{Bi}_2\text{O}_3$  (monoclinic) changes to  $\gamma$ - $\text{Bi}_2\text{O}_3$  (cubic). The phase transition in  $\text{Bi}_2\text{O}_3$  observed in ZBCM system agrees with that reported in the literature [106,191-193,199,200, 202]. The X-ray diffractograms recorded for the powder sintered at other temperatures like, 1000, 1050, 1100, 1150,1200, 1250 and 1300°C show that all the characteristic lines of ZnO are present similar to the X-ray diffractogram of 900°C. The  $\gamma$ - $\text{Bi}_2\text{O}_3$  characteristic lines are visible in the X-ray diffractograms recorded upto 1100°C and are not

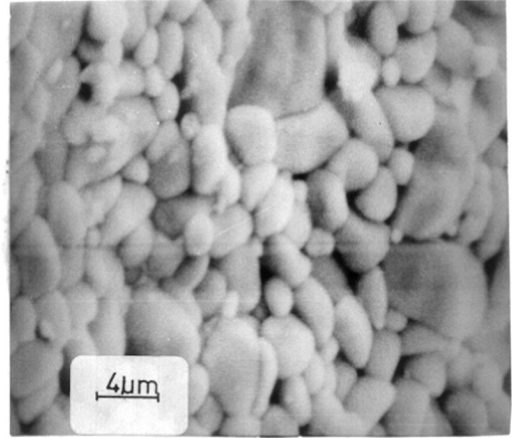
visible for the powders sintered at 1200, 1250 and 1300°C due to evaporation of  $\text{Bi}_2\text{O}_3$ . The absence of  $\text{Bi}_2\text{O}_3$  involves decrease in density and the poor nonlinear behaviour of the compacts. The 'd' values for the ZnO and  $\gamma\text{-Bi}_2\text{O}_3$  crystalline phases observed in the X-ray diffractograms are summarised in Table 3.5(a)-3.5(b).

(c) Microstructural Analysis by SEM

Scanning Electron Microscopic (SEM) studies were carried out to observe the microstructural changes in ZBCM varistor system sintered at different temperatures (900-1300°C). Fig.3.7 shows the typical SEM photomicrographs of the pellets sintered at 1000, 1050 and 1100°C with reference to the optimum sintering temperature. It is seen from the SEM photomicrographs that the microstructure consists of ZnO grains surrounded by a second phase/segregation layer of  $\text{Bi}_2\text{O}_3$  which is responsible for nonohmic behaviour [29,62,83]. The average ZnO grain size increases with the increase in sintering temperature and the width of the second phase/segregation layer also changes. Initially at lower sintering temperature, the ZnO grains are smaller and are surrounded by a second phase having larger width. As the sintering temperature increases the width of second phase becomes thicker with increase in grain size. At 1050°C, larger grains are surrounded by thicker segregation layer of  $\text{Bi}_2\text{O}_3$ . The SEM photomicrographs for the pellets sintered at 1100, 1150,



(a)



(b)



(c)

Fig. 3.7 Typical photomicrographs (SEM) of ZBCM varistor sintered at (a) 1000 (b) 1050 and (c) 1100°C.

**Table-3.5(a):** 'd' values for ZnO crystalline phases in ZBCM varistor system sintered at different temperatures

hkl	PM	900	1000	1050	1100	1150	1200	1250	1300
100	2.82	2.82	2.81	2.83	2.83	2.82	2.82	2.82	2.82
002	2.60	2.60	2.60	2.60	2.60	2.61	2.60	2.61	2.60
101	2.49	2.48	2.48	2.48	2.49	2.49	2.45	2.49	2.49
102	1.92	1.90	1.90	1.91	1.91	1.92	1.90	1.92	1.91
110	1.63	1.63	1.62	1.63	1.62	1.63	1.62	1.63	1.63
103	1.48	1.48	1.48	1.48	1.48	1.48	1.48	1.50	1.48
200	1.40	1.40	1.41	1.40	1.40	1.41	1.40	1.41	1.40
112	1.38	1.38	1.38	1.38	1.38	1.38	1.38	1.38	1.38
201	1.36	1.36	1.36	1.36	1.36	1.36	1.36	1.36	1.36
004	1.30	1.30	1.30	1.30	1.30	1.30	1.30	1.30	1.30

**3.5(b):** 'd' values for  $\sqrt{3}$ -Bi<sub>2</sub>O<sub>3</sub> crystalline phases in ZBCM varistor system sintered at different temperatures.

hkl	900	1000	1050	1100	1150	1200	1250	1300
310	3.22	3.20	3.22	3.20				
321	2.86	-	2.97	-	----- ABSENT -----			
400	2.50	2.88	2.74	2.74				
611	1.70	-	1.70	-				
620	1.65	1.65	1.66	1.65				

1200, 1250 and 1300°C, show that grain size further increases with the increase of sintering temperature and the segregation layer disappears slowly as the sintering temperature increases to 1300°C. The average grain size was calculated from the SEM photomicrographs using the method given in chapter-2. Experimental results on average grain size as a function of sintering temperature are summarised in Table-3.6.

**Table-3.6:** Grain size (d) of ZBCM varistor system sintered at different temperatures.

Sint. temp. (°C)	900	1000	1050	1100	1150	1200	1250	1300
d (µm)	2.0	4.0	5.3	14.0	20.1	26.9	39.0	47.5

Error of measurement -  $d = \pm 0.1 \mu\text{m}$

It is seen from the table that the average grain size increases with the increase in sintering temperature e.g.  $d_{(900)} \approx 2.0 \mu\text{m}$ ,  $d_{(1000)} \approx 4.0 \mu\text{m}$ ,  $d_{(1050)} \approx 5.3 \mu\text{m}$ ,  $d_{(1100)} \approx 14.0 \mu\text{m}$ ,  $d_{(1150)} \approx 20.1 \mu\text{m}$ ,  $d_{(1200)} \approx 26.9 \mu\text{m}$ ,  $d_{(1250)} \approx 39.0 \mu\text{m}$  and  $d_{(1300)} \approx 47.5 \mu\text{m}$  respectively. This shows that grain growth is taking place with the increase in sintering temperature. These results are interpreted as follows:



The added  $\text{Bi}_2\text{O}_3$  in the ZBCM system melts at about  $900^\circ\text{C}$  and spreads through the grain boundaries to form a second phase during liquid phase sintering and remains effectively isolated as this phase solidifies during cooling. At  $1000^\circ\text{C}$ , the molten  $\text{Bi}_2\text{O}_3$  partly dissolves in the ZnO grains to make the second phase thinner. The dissolved  $\text{Bi}_2\text{O}_3$  promotes the grain growth and segregates again at the grain boundary at  $1050^\circ\text{C}$  to make the second phase wider (thick). Above  $1100^\circ\text{C}$ ,  $\text{Bi}_2\text{O}_3$  in the second phase starts evaporating and it almost completely evaporates at  $1300^\circ\text{C}$ , which results into the poor performance of the varistor as seen from the I-V characteristics. The absence of second phase at higher sintering temperatures as seen from the photomicrographs agree with the absence of characteristic lines in X-ray diffractograms and the poor I-V performance of ZBCM system as concluded from the density, XRD and I-V measurement studies. From the literature, it is known that  $\text{Co}_2\text{O}_3$  and  $\text{MnO}_2$  are localised at the grain boundaries and do not distribute through the grains i.e. added  $\text{Co}_2\text{O}_3$  and  $\text{MnO}_2$  do not dissolve in ZnO grains [26-29,62,68,70]. These dopants form a second phase with  $\text{Bi}_2\text{O}_3$  and increase the  $\alpha$  value. The ZBCM pellets sintered at  $1300^\circ\text{C}$  have no segregation layer due to evaporation of  $\text{Bi}_2\text{O}_3$  and to the dissolution of  $\text{Co}_2\text{O}_3$  and  $\text{MnO}_2$  in ZnO as seen from XRD studies. The average grain size of the pellet when sintered at  $1050^\circ\text{C}$  is  $\approx 5.3 \mu\text{m}$ , is much smaller as compared to the grain size observed by Smith et. al. [42] for the same composition at  $1100^\circ\text{C}$  (d

$\approx 21 \mu\text{m}$ ). These results show that due to controlled processing conditions, functional microstructure of our system has been improved. From the SEM photomicrographs, the microstructure of the ZBCM varistor system can be imagined as: ZnO grains are isolated from each other by a continuous network of  $\text{Bi}_2\text{O}_3$  segregation/intergranular layer with some voids and pores, and is well agreed with the functional microstructure of a ZnO based varistor reported in the literature [28-29,62,174-175,183-184,195].

(d) Surface Analysis by XPS

The X-ray photoelectron spectroscopic (XPS) technique was used to study the electronic structure and migration of  $\text{Bi}_2\text{O}_3$  at the grain boundaries. Fig.3.8 shows the XPS spectra (Intensity Vs. Binding energy) of ZBCM varistor system recorded on physical mixture and the pellets sintered at 900, 1050, 1100 and 1300°C. The intensity peaks were identified using known XPS data [266] and were assigned to Zn-2p<sub>3/2</sub>, Bi-4f<sub>7/2</sub> and Bi-4f<sub>5/2</sub> states. It is seen that the intensity of Bi peak increases and Zn peak decreases as a function of increase in sintering temperature. This is possible due to the migration of  $\text{Bi}_2\text{O}_3$  on ZnO grain surface. To get the clear idea about the migration, XPS spectra was recorded at higher resolution. The peak intensities (arb. unit) of Zn-2p<sub>3/2</sub> and Bi-4f<sub>7/2</sub> states were calculated and are given in Table-3.7 as a function of sintering temperature.

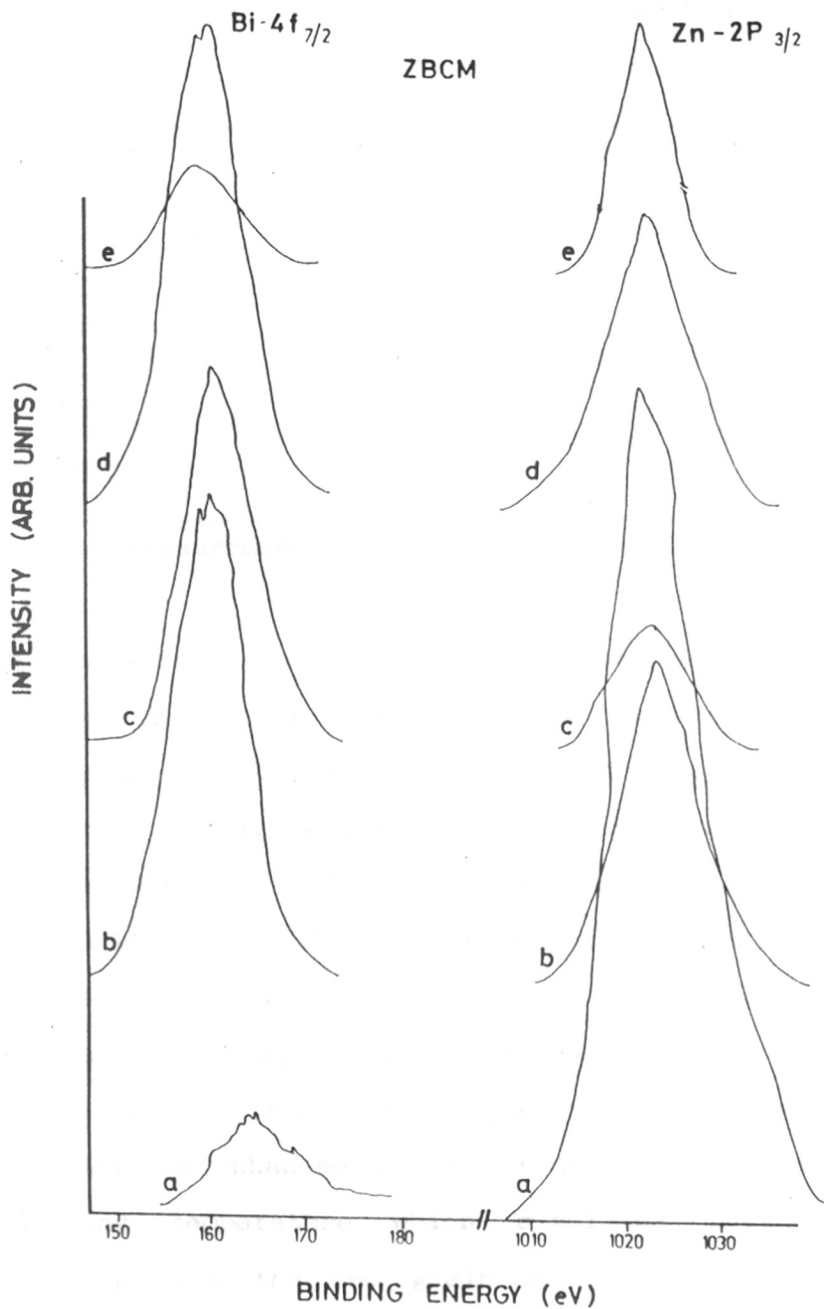


Fig. 3.8 XPS Spectra of ZBCM varistor sintered (a) PM (b) 900 (c) 1050 (d) 1100 and (e) 1300°C.

**Table-3.7:** XPS peak intensities ( $\times 10^4$  CPS) of Zn-2p<sub>3/2</sub> and Bi-4f<sub>7/2</sub> states observed in ZBCM varistor system sintered at different temperatures

Sint. temp. (°C)	PM	900	1050	1100	1300
Zn-2p <sub>3/2</sub>	9.0	7.2	3.6	6.3	9.6
Bi-4f <sub>7/2</sub>	1.4	6.0	6.3	4.8	1.6
Ratio: Bi-4f <sub>7/2</sub> ----- Zn-2p <sub>3/2</sub>	0.16	0.83	1.75	0.76	0.17

Error of measurements - XPS intensity =  $\pm 0.1$  arb. unit.

The intensity of Zn-2p<sub>3/2</sub> state for the physical mixture is  $I_{(PM)} \approx 9.0$  and for other sintering temperature,  $I_{(900)} \approx 7.2$ ,  $I_{(1050)} \approx 3.6$ ,  $I_{(1100)} \approx 6.3$  and  $I_{(1300)} \approx 9.6$ . This shows that initially peak intensity decreases when pellet sintered between 900-1050°C and increases when sintered between 1100-1300°C. The intensity of Bi state for physical mixture is  $I_{(PM)} \approx 1.4$  and for their sintering temperatures,  $I_{(900)} \approx 6.0$ ,  $I_{(1050)} \approx 6.3$ ,  $I_{(1100)} \approx 4.8$  and  $I_{(1300)} \approx 1.6$ . These results show that Bi peak intensity is enhanced continuously with the increase of sintering temperature which signifies that Bi<sub>2</sub>O<sub>3</sub> is migrating from the ZnO grain surface and progressively becomes pronounced at higher sintering temperatures. <sup>(T < 1050°C)</sup> This is clearly seen from the increase in intensities of Bi peaks in comparison with that of Zn peak.

To get clear idea about the variation of Zn and Bi peak intensities, ratio of Bi-4f<sub>7/2</sub>/Zn-2p<sub>3/2</sub> peak intensity curve area (arb. unit) was calculated from the XPS spectra and is given in Table-3.7 as a function of sintering temperature. This data is plotted in Fig.3.9 as Bi-4f<sub>7/2</sub>/Zn-2p<sub>3/2</sub> Vs. sintering temperature. It is seen that the ratio is maximum for a pellet sintered at 1050°C i.e. Bi-peak is maximum and Zn peak is minimum. This indicates that at 1050°C the migration of Bi<sub>2</sub>O<sub>3</sub> is maximum and more or less complete. This is the optimum temperature at which ZBCM varistors have also shown highest  $\alpha$  value, maximum densification and smaller grain size with more number of grain boundaries as concluded earlier.

When the pellet is sintered at 1100°C and 1300°C, Bi peak intensity suddenly decreases and Zn peak intensity increases i.e. the ratio decreases. This is due to evaporation of Bi<sub>2</sub>O<sub>3</sub> from ZnO grain surfaces. In fact, there is a continuous loss of Bi<sub>2</sub>O<sub>3</sub> from the ZnO surface layers during sintering at higher temperatures as clearly seen by comparing the intensity curve area ratio with the physical mixture. Indirectly, due to the loss of Bi<sub>2</sub>O<sub>3</sub> from surface layers, the fresh ZnO surface layers are exposed to the X-ray excitation, culmination in the rise in intensity of the Zn peaks.

However, XPS spectra does not show any visible intensity peaks of Co<sub>2</sub>O<sub>3</sub> and MnO<sub>2</sub> states. This is mainly because Co<sub>2</sub>O<sub>3</sub> and MnO<sub>2</sub> are not migrating on the surface of

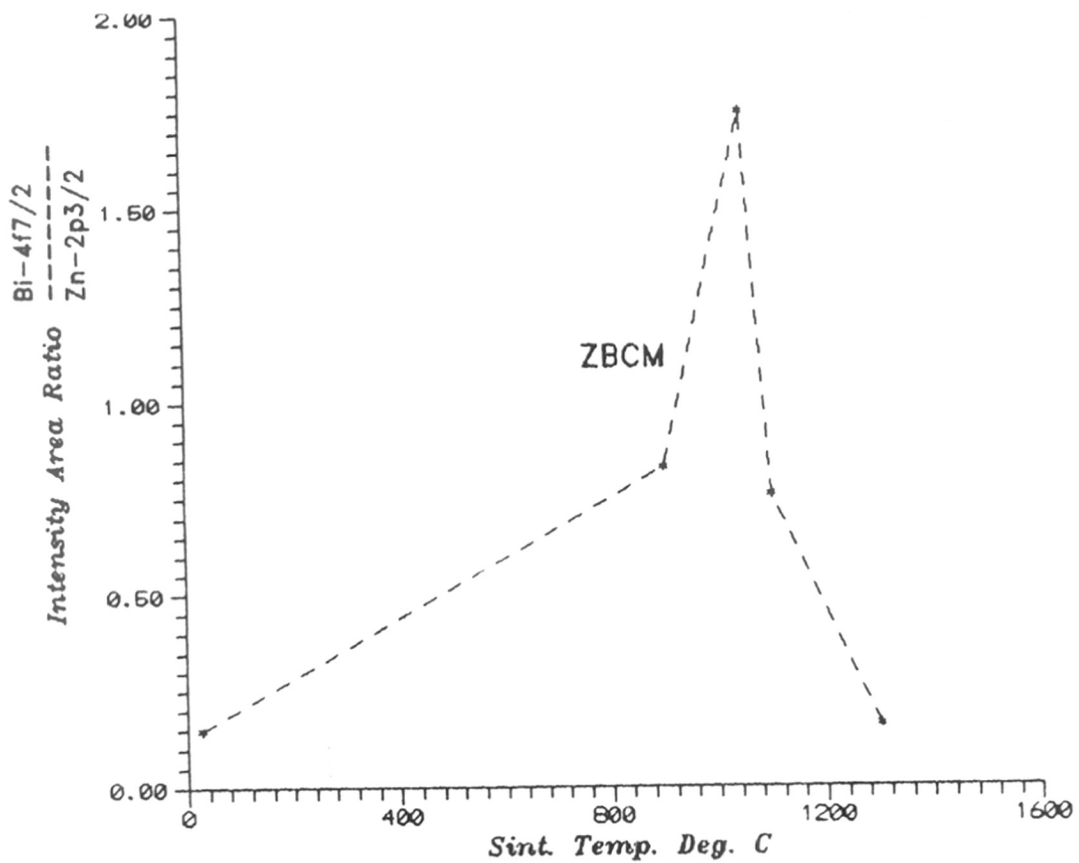


Fig. 3.9 XPS intensity peak area Vs sintering temp. of ZBCM varistor.

ZnO grains but are dissolving during liquid phase sintering into the zinc oxide phase. The migration of  $\text{Bi}_2\text{O}_3$  from ZnO grain surface in ZBCM varistor system as a function of sintering temperature agrees with the reported results in the literature [253,255]. It is concluded from the above studies that  $\text{Bi}_2\text{O}_3$  phase plays an important role to achieve the nonlinear property.

#### 3.4 Current-Voltage (I-V) Characteristics of ZBCM-10MgO Varistor System

Fig.3.3 shows the current-voltage (I-V) characteristics of ZBCM-10MgO varistor system sintered at different sintering temperature (900-1300°C/1 hr) plotted in log-log scale. These I-V plots are similar to the ZBCM varistor system as discussed in section 3.3, except for the pellets sintered at 900 and 1000°C, it shows the linear behaviour (absence of nonlinearity). From the I-V plots, values of nonlinearity coefficient and breakdown electric field were calculated as a function of sintering temperature and are summarised in Table-3.8. It is seen from the table that,

(i) the nonlinearity is absent for the pellets sintered at 900 and 1000°C. This is mainly because  $\text{Bi}_2\text{O}_3$  may diffuse rapidly on the ZnO surfaces through the grain boundaries and finally reaches to the other surfaces during sintering.

**Table-3.8:**  $E_b$  and  $\alpha$  values of ZBCM-10MgO varistor system sintered at different temperatures

Sint. temp. ( $^{\circ}$ C)	900	1000	1050	1100	1150	1200	1250	1300
$E_b$ (V/mm)	X	X	1000	501	398	316	200	168
$\alpha$	X	X	29	10	7	5	3	3

X - Absence of nonlinearity (linear behaviour)

In such cases varistor does not have active grain boundaries responsible for linear behaviour.

(ii) The breakdown electric field ( $E_b$ ) decreases as a function of increase in sintering temperature e.g.  $E_b(1050) \approx 1000$  V/mm,  $E_b(1100) \approx 501$  V/mm,  $E_b(1150) \approx 398$  V/mm,  $E_b(1200) \approx 316$  V/mm,  $E_b(1250) \approx 200$  V/mm and  $E_b(1300) \approx 168$  V/mm respectively.

(iii) The nonlinearity coefficient ( $\alpha$ ) decreases with the increase in the sintering temperature e.g.  $\alpha(1050) \approx 29$ ,  $\alpha(1100) \approx 10$ ,  $\alpha(1150) \approx 7$ ,  $\alpha(1200) \approx 5$ ,  $\alpha(1250) \approx 3$  and  $\alpha(1300) \approx 3$  respectively. However, in case of ZBCM system it is noticed that initially  $\alpha$  increases as a function of increase in sintering temperature in the temperature 900-1050 $^{\circ}$ C and then decreases when sintered at 1100-1300 $^{\circ}$ C.

The variation in the breakdown electric field and nonlinearity coefficient as a function of sintering temperature observed is similar to ZBCM varistor system and



well agrees with the observation of earlier researchers [25-26,42,68,81-83,85-86,113,239]. The above results show that the pellet sintered at 1050°C/1 hr exhibiting highest nonlinear coefficient ( $\alpha \approx 29$ ) with breakdown electric field  $E_b \approx 1000$  V/mm. This temperature is found to be the optimum temperature for sintering of compacts. The values of nonlinearity coefficient ( $\alpha$ ) and breakdown electric field ( $E_b$ ) are better than reported by Smith et. al.[42] for nearly identical composition (MgO 9.6 mol% in ZBCM system,  $\alpha_{(1100)} \approx 13$ ,  $E_{b(1100)} \approx 200$  V/mm.

Comparing the above results with that obtained for ZBCM varistor system, it shows that there is considerable improvement in the breakdown electric field with almost same nonlinearity coefficient for the pellets sintered at 1050°C/1 hr under identical conditions ( $E_{b(\text{ZBCM})} \approx 282$  V/mm,  $\alpha_{\text{ZBCM}} \approx 36$ ,  $E_{b(\text{ZBCM-10MgO})} \approx 1000$  V/mm,  $\alpha_{(\text{ZBCM-10MgO})} \approx 29$ ). The improvement in the performance parameters are most likely due to improved functional microstructure developed during controlled processings. It is known that higher values can be obtained by increase in the number of grain boundaries and reducing the grain size. Two possibilities exist for this improvement in microstructure [42,166,171,252]; (i) due to addition of MgO, the grain growth of the dense compacts of highly conducting ZnO grains is inhibited, which helps in increasing the number of barriers per unit thickness and; (ii) the composition may correspond to two phase system containing zincite and a

mixture of ZnO and magnesia, which is highly insulating. To understand the relative contributions from these two pathways, extensive physico-chemical characterizations of active and sintered powder/pellets were carried out similar to ZBCM varistor system.

(a) Density Analysis

The densities of the sintered compacts were calculated as a function of sintering temperature using the method described in chapter-2. The density of the green compact was also calculated for reference purpose. The experimental results are summarised in Table-3.9.

**Table-3.9:** Density ( $\rho$ ) of ZBCM-10MgO varistor system sintered at different temperatures.

Sint. temp. ( $^{\circ}\text{C}$ )	PM	900	1000	1050	1100	1150	1200	1250	1300
$\rho$ (gm/cc)	3.74	5.03	5.10	5.20	5.00	4.98	4.88	4.83	4.76

Error of measurement- Mass:  $\pm 0.001$  gm, Dimension:  $\pm 0.01$  mm.

The effect of sintering temperature on density can be easily seen from the table. The trend is similar to ZBCM pellets as observed earlier. The density of green compacts i.e. for physical mixture  $\rho$  (PM)  $\approx 3.74$  gm/cc which is  $\approx 66.96\%$  of the theoretical density of a pure ZnO (5.606 gm/cc). The density increases with the increase of

sintering temperature initially in the temperature range of 900-1050°C e.g.  $\rho(900) \approx 5.03$  gm/cc,  $\rho(1000) \approx 5.10$  gm/cc and  $\rho(1050) \approx 5.20$  gm/cc respectively. When the sintering temperature increased beyond 1050°C and till 1300°C, the density decreases with the increase in sintering temperature e.g.  $\rho(1100) \approx 5.00$  gm/cc,  $\rho(1150) \approx 4.98$  gm/cc,  $\rho(1200) \approx 4.88$  gm/cc,  $\rho(1250) \approx 4.83$  gm/cc and  $\rho(1300) \approx 4.26$  gm/cc respectively.

The density of a pellet/dense compact, when sintered at 1050°C, shows the highest value, indicates the high degree of compactness. In other words, 1050°C is an optimum sintering temperature at which high degree of compactness is achieved in the dense compacts/pellets. The decrease in the density at higher sintering temperature is mainly due to the weight loss of the pellets and leads to the similar observation made in case of ZBCM varistor system.

#### (b) Phase Analysis by XRD

To identify the complex phases (if any) developed during synthesis, powder X-ray diffractograms were recorded on active powder (physical mixture) and the powder sintered at different sintering temperatures. To identify the crystalline phases of pure ZnO during sintering, X-ray diffractograms were recorded for comparison. Fig.3.10 shows the X-ray diffractograms of pure ZnO, physical mixture and powder sintered at different temperatures. These X-ray diffractograms are not different from those observed in case of ZBCM varistor system. There is no indication of any

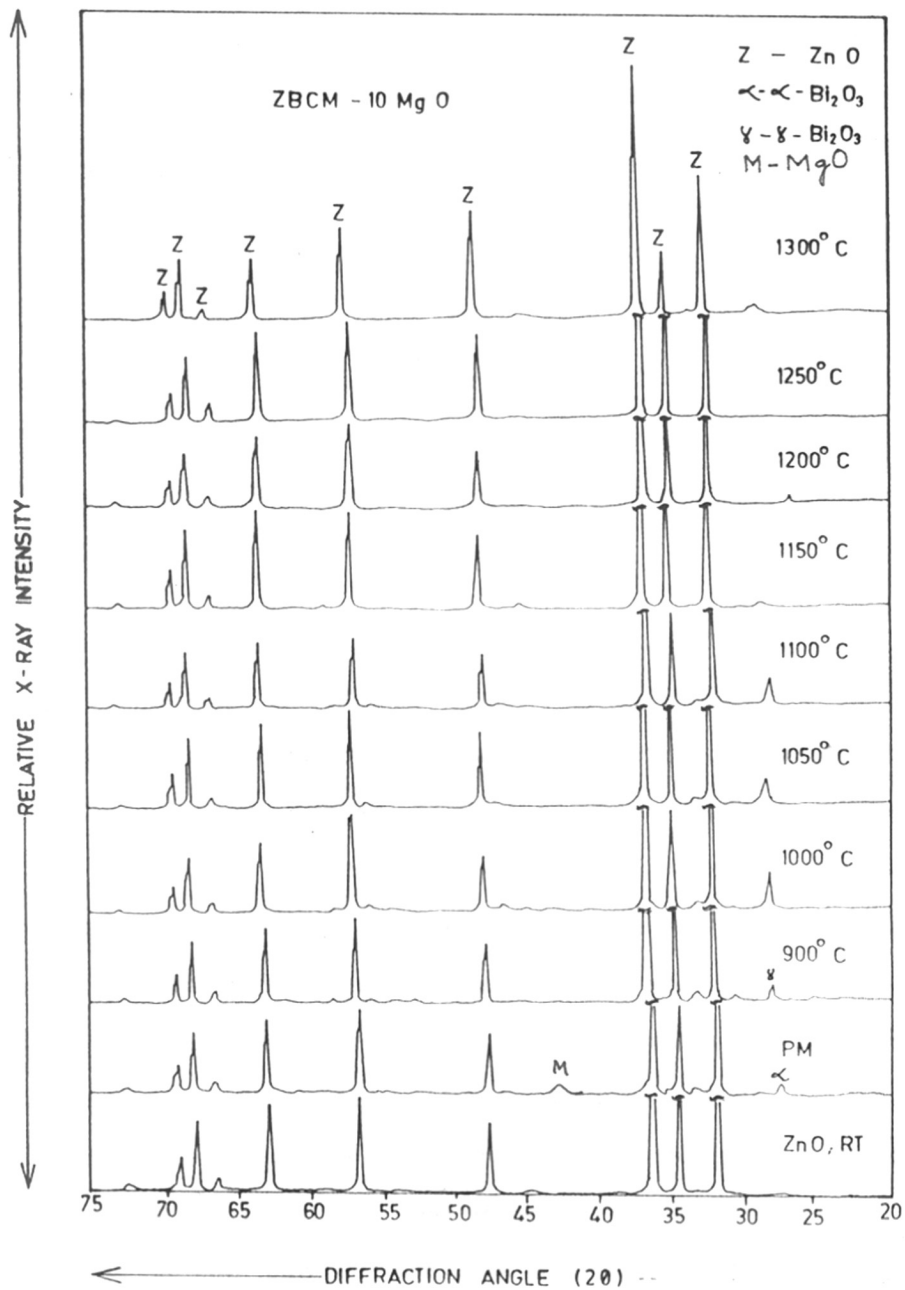
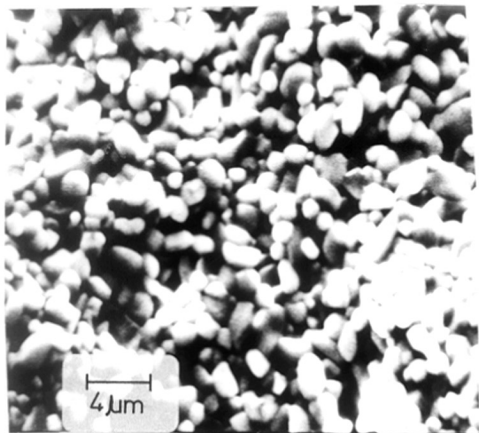


Fig. 3.10 Powder X-ray diffractogram (XRD) of a pure ZnO, physical mixture and ZBCM-10MgO powder sintered at different temperatures.

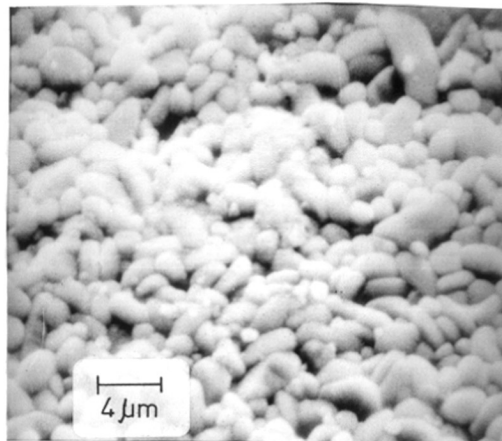
separate (mixed phase) characteristic lines of MgO ( $2\theta \approx 42.9, 63.3$ ) [268], shows that MgO forms a solid solution (ZnO-MgO) with ZnO during sintering. In other words, all characteristic lines of this two phase system (ZnO and ZnO-MgO) are overlapping with each other. We did not attempt to resolve this superimposed pattern to derive finite changes in the lattice parameters of ZnO-MgO solid solutions. This confirms the postulates that the formation of two phase system is within the detection limit of powder XRD data. The 'd' values of ZnO and  $\gamma$ -Bi<sub>2</sub>O<sub>3</sub> crystalline phases observed in ZBCM system are summarised in Tables-3.10(a) and 3.10(b).

(c) Microstructural Analysis by SEM

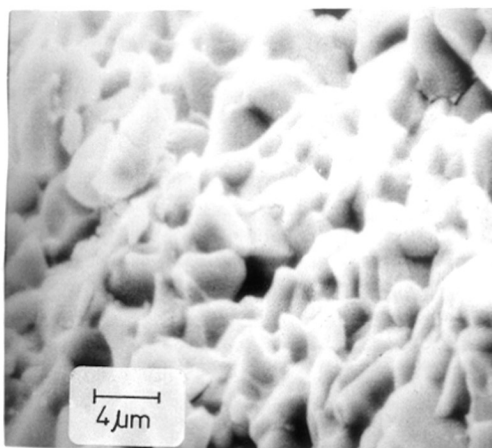
Scanning Electron Microscopic (SEM) studies were carried out to observe the microstructural changes in ZBCM-10MgO varistor system sintered at different temperatures (900-1300°C). Fig.3.11 shows the typical SEM photomicrographs of the pellets sintered at 1000, 1050 and 1100°C with reference to the optimum sintering temperature. The average grain size was calculated from the photomicrographs using the procedure given in chapter-2. Experimental results on average grain size as a function of sintering temperature are summarised in Table-3.11. It is seen from the table that the average grain size increases with the increase of sintering temperature e.g.  $d_{(900)} \approx 1.4 \mu\text{m}$ ,  $d_{(1000)} \approx 3.2 \mu\text{m}$ ,  $d_{(1050)} \approx 4.0 \mu\text{m}$ ,  $d_{(1100)} \approx 9.0 \mu\text{m}$ ,  $d_{(1150)} \approx 10.0 \mu\text{m}$ ,  $d_{(1200)} \approx 12.5 \mu\text{m}$  and  $d_{(1300)} \approx 19.8$



(a)



(b)



(c)

Fig. 3.11 Typical photomicrographs (SEM) of ZBCM-10 MgO varistor sintered at (a) 1000 (b) 1050 and (c) 1100°C.

**Table-3.10(a):** 'd' values for ZnO crystalline phases in ZBCM-10MgO varistor system sintered at different sint. temps.

hkl	PM	900	1000	1050	1100	1150	1200	1250	1300
100	2.82	2.82	2.81	2.82	2.81	2.83	2.83	2.811	2.81
002	2.60	2.61	2.60	2.60	2.60	2.60	2.60	2.60	2.59
101	2.48	2.48	2.48	2.47	2.48	2.48	2.48	2.48	2.48
102	1.91	1.91	1.90	1.94	1.91	1.91	1.91	1.91	1.91
110	1.63	1.63	1.62	1.62	1.63	1.63	1.63	1.63	1.63
103	1.48	1.48	1.48	1.48	1.48	1.47	1.48	1.48	1.47
200	1.40	1.40	1.42	1.40	1.40	1.40	1.41	1.41	1.41
112	1.38	1.38	1.38	1.38	1.38	1.38	1.38	1.38	1.38
201	1.36	1.36	1.36	1.36	1.36	1.36	1.36	1.36	1.36
004	1.30	1.30	1.30	1.30	1.30	1.30	1.30	1.29	1.29

**3.10(b):** 'd' values for  $\delta$ -Bi<sub>2</sub>O<sub>3</sub> crystalline phases in ZBCM-10MgO varistor system sintered at different temperatures

hkl	900	1000	1050	1100	1150	1200	1250	1300
310	3.22	3.21	3.21	3.22				
611	1.74	-	-	-				
400	2.73	2.74	2.74	2.74				
321	2.75	2.96	-	3.20	<-----	ABSENT	----->	
541	1.65	1.66	1.65	1.63				
620	1.70	1.71	-	1.70				
640	1.50	-	-	-				

**Table-3.11:** Grain size(d) of ZBCM-10MgO varistor system sintered at different temperatures.

Sint. temp. (°C)	900	1000	1050	1100	1150	1200	1250	1300
d (µm)	1.4	3.2	4.0	9.0	10.0	12.5	12.8	19.8

Error of measurement -  $d = \pm 0.1 \mu\text{m}$

µm respectively. From the critical observations of SEM photomicrographs of ZBCM and ZBCM-10MgO varistor systems, it is seen that the overall average grain size of ZBCM--10MgO system is small, indicating that MgO has acted as a grain growth inhibitor. The grains are uniformly distributed and closely packed with more number of grain boundaries. This shows the improvement in the functional microstructure. The improvement in the functional microstructure helps in increasing the breakdown electric field without affecting the nonlinear behaviour. Smith et. al. [42] have reported that magnesium oxide dissolves in the spinel particles and stabilizes them during sintering. This reduces the grain size and increases the number of grain boundaries and thereby creating more current carrying paths and helps in increasing the breakdown electric field.



(d) Surface Analysis by XPS

Fig.3.12 shows XPS spectra (intensity Vs. Binding energy) of ZBCM-10MgO varistor system recorded on physical mixture and pellets sintered at 900, 1050 and 1300°C. The spectra are not different from that observed for ZBCM varistor system. The peak intensities (arbt. unit) of Zn-2p<sub>3/2</sub> and Bi-4f<sub>7/2</sub> states were calculated and are given in Table-3.12.

**Table-3.12:** XPS peak intensities (X10<sup>4</sup> CPS) of Zn-2p<sub>3/2</sub> and Bi-4f<sub>7/2</sub> states observed in ZBCM-10MgO varistor system sintered at different temps.

Sint. temp. (°C)	PM	900	1050	1100	1300
Zn-2p <sub>3/2</sub>	6.3	5.7	4.5	6.0	8.4
Bi-4f <sub>7/2</sub>	0.5	6.0	7.2	4.2	2.0
Ratio: Bi-4f <sub>7/2</sub> ----- Zn-2p <sub>3/2</sub>	0.08	1.05	1.60	0.70	0.23

Error of measurements - XPS intensity = ±0.1 arb. unit.

It is seen from the table that the intensity of Zn-2p<sub>3/2</sub> state as a function of sintering temperature for the physical mixture is I<sub>(PM)</sub> ≈ 6.3, and for other sintering temperatures are, I<sub>(900)</sub> ≈ 5.7, I<sub>(1050)</sub> ≈ 4.5, I<sub>(1100)</sub> ≈ 6.0 and I<sub>(1300)</sub> ≈ 8.4. This shows that initially peak intensity decreases when pellet is sintered between 900-1050°C and increases when sintered between 1100-1300°C. The

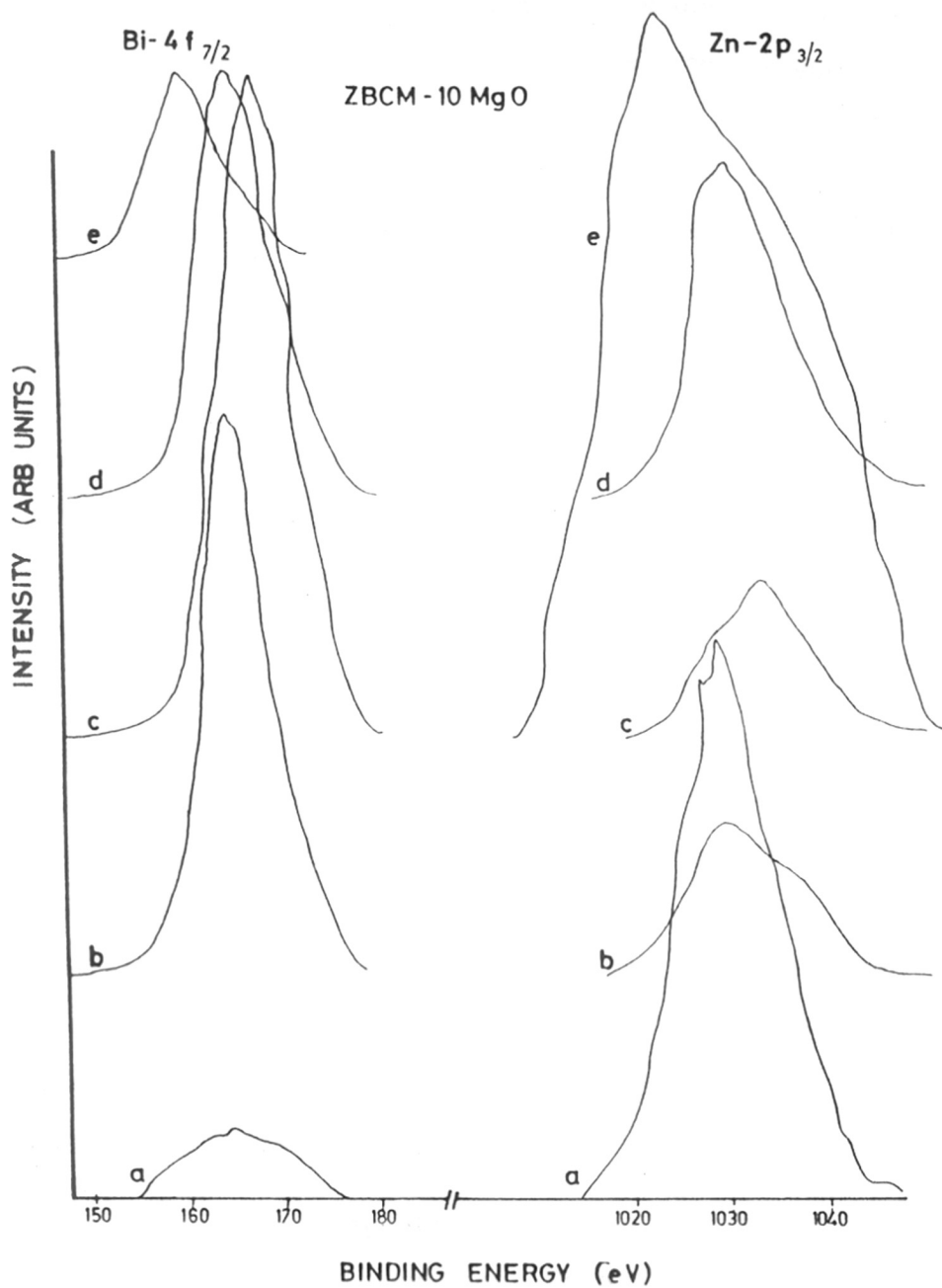


Fig. 3.12 XPS Spectra of ZBCM-10MgO varistor sintered at (a) PM (b) 900 (c) 1050 (d) 1100 and (e) 1300°C.

intensity of Bi state for physical mixture is  $I_{(PM)} \approx 0.5$  and for other sintering temperatures are,  $I_{(900)} \approx 6.0$ ,  $I_{(1050)} \approx 7.2$ ,  $I_{(1100)} \approx 4.2$  and  $I_{(1300)} \approx 2.0$ . The above results lead to the similar discussion in comparison with ZBCM varistor system and confirms that  $\text{Bi}_2\text{O}_3$  is migrating from ZnO grain surface with increase of sintering temperature. To get clear idea about the migration of  $\text{Bi}_2\text{O}_3$ , Bi-4f<sub>7/2</sub>/Zn-2p<sub>3/2</sub> peak intensity curve area ratio (arb/unit) was calculated from XPS spectra and is given in Table-3.12 as a function of sintering temperature. The data is plotted in Fig.3.13 as Bi-4f<sub>7/2</sub>/Zn-2p<sub>3/2</sub> Vs sintering temperature. It is seen from Table-3.12 and Fig.3.13, the ratio is maximum for a pellet sintered at 1050°C, i.e. Bi-4f<sub>7/2</sub> peak is maximum and Zn-2p<sub>3/2</sub> peak is minimum. This indicates that at 1050°C the migration of  $\text{Bi}_2\text{O}_3$  to intergranular layer separating ZnO grains is maximum and more or less complete. This is the optimum sintering temperature at which density is maximum and the microstructure consists of grains of smaller size with more number of grain boundaries and gives higher values of performance parameters.

However, XPS spectra does not show any visible intensity peaks of Mg-2p<sub>3/2</sub> states. This is mainly because MgO is not migrating on the ZnO grains but dissolves during liquid phase sintering and forms ZnO-MgO solid solution with ZnO as predicted earlier from XRD and SEM studies.

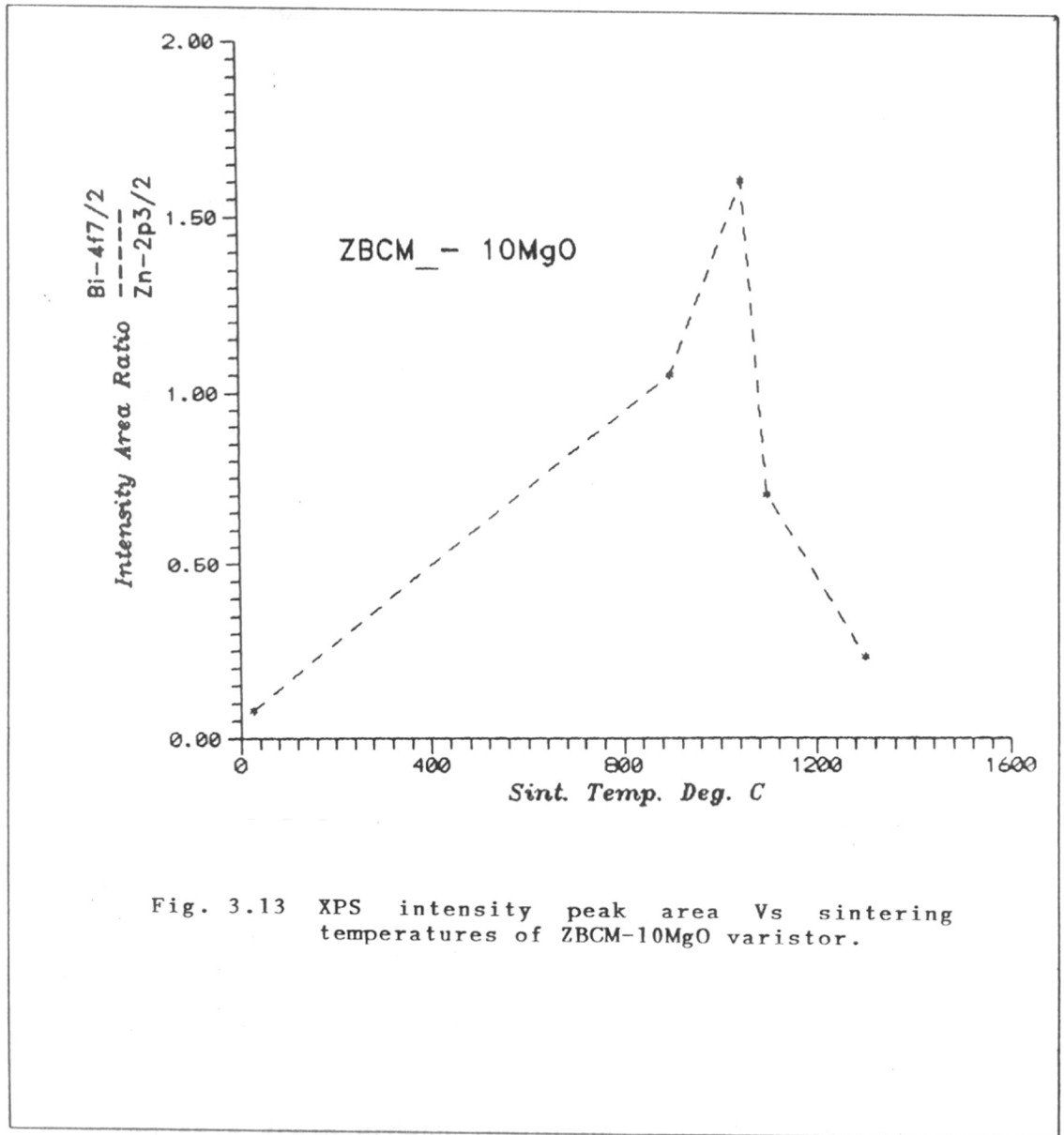


Fig. 3.13 XPS intensity peak area Vs sintering temperatures of ZBCM-10MgO varistor.

### 3.5 Improvement in the Performance Parameters of ZBCM Varistors with 10mol% MgO

It is seen from the results discussed in section 3.3-3.4 that the performance parameters of modified varistor with 10MgO are improved when sintered at 1050°C. This is mainly due to the improvement in the functional microstructure developed during synthesis. The SEM photomicrographs of ZBCM-10MgO varistors have shown that: (i) Due to addition of MgO, the grain growth of the dense compacts of highly conducting ZnO grains is inhibited and helped in increasing the number of barriers per unit thickness in the sintered compacts and; (ii) the composition corresponds to two phase system containing zincite and a mixture of ZnO and magnesia which is highly insulating. The ZBCM-10MgO varistor has shown the difference in microstructure as compared to ZBCM varistor when sintered at 1050°C. In case of ZBCM, average grain size is  $\approx 5.3 \mu\text{m}$  and grains are not uniformly distributed. However, in case of ZBCM-10MgO, average grain size is  $\approx 4 \mu\text{m}$  and grains are uniformly distributed and closely packed. This increases the number of grains and grain boundaries in a modified varistor with 10mol% MgO. This shows that MgO acted as a grain growth inhibitor. Consequently, all these changes in the microstructure resulted in different current carrying pathways with different breakdown voltages for each pathway. As the number of current carrying pathways

are increased in ZBCM-10MgO microstructure, which leads to the increase of breakdown electric field as evident from the I-V characteristic studies i.e. breakdown electric field per barrier is increased.

To find the role of breakdown electric field per barrier, electric field versus the reciprocal of average grain size is plotted as shown in Fig.3.14(a)-3.14(b) for the ZBCM and ZBCM-10MgO varistors. The slope of the plots directly gives the average value of electric field per barrier ( $V_g$ ). The value of ( $V_g$ ) from the slopes are: for  $V_g$  (ZBCM)  $\approx 1.16$  V/barrier and  $V_g$  (ZBCM-10MgO)  $\approx 3.0$  V/barrier. The increase in the value of  $V_g$  (ZBCM-10MgO) is certainly due to the increase in the number of current carrying paths in the functional microstructure of the dense compacts. This confirms the increase of breakdown electric field in the modified varistor system. The values of  $V_g$  (ZBCM) and  $V_g$  (ZBCM-10MgO) observed are well agreed with the values reported in the literature [45,63,79,162, 181,188,204,237,252] for the ZnO based varistors.

Grauter et. al.[79] and Entage [206] have also shown by statistical arguments that the wider distribution of the grain size in ceramic bodies causes the lower breakdown voltage per grain boundary. The much greater value of breakdown voltage per grain boundary in the modified varistors is attributed to a narrow distribution of grain size in the varistor i.e. it is related to the functional microstructure. The modified varistors have shown the

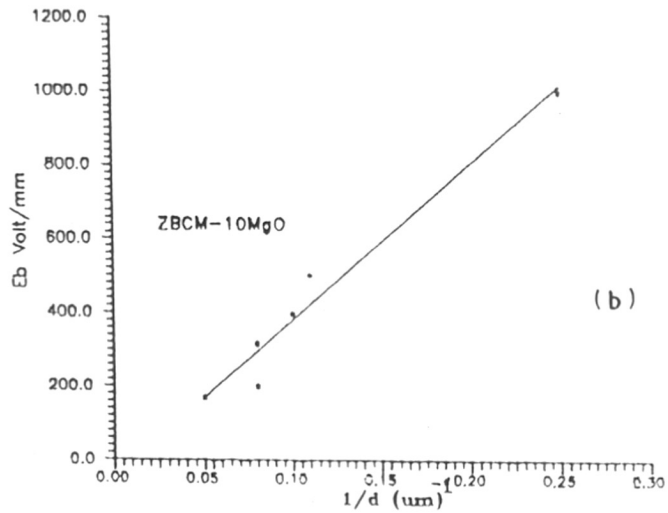
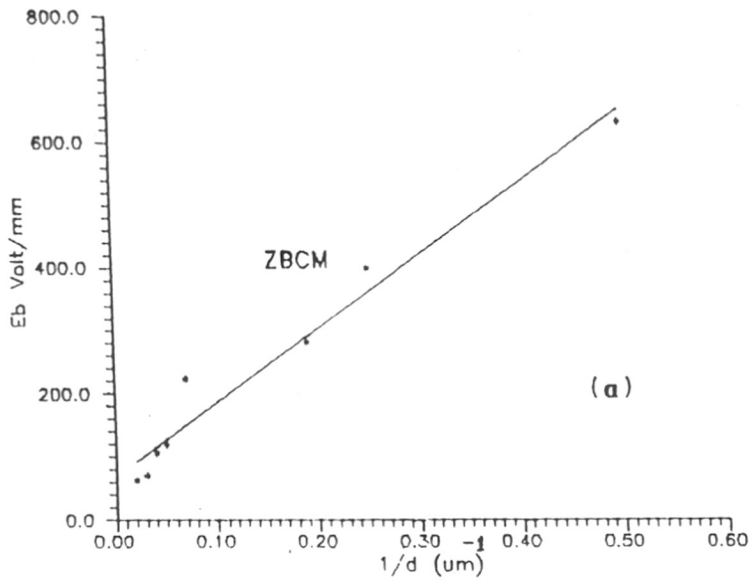


Fig. 3.14 Electric field versus Reciprocal of grain size of (a) ZBCM and (b) ZBCM-10 MgO varistors.

improvement in the functional microstructure, which directly leads the high breakdown electric field as observed from our experimental results.



## REFERENCES

1. Frontiers in Chemical Engineering. Research Needs and Opportunities, National Academy Press, Washington D.C. (1988).
2. Science of Ceramic Processing (edited by D.R. Ulrich), John Wiley and Sons, NY (1986).
3. Material Science Research, Vol.20, Tailoring Multiphase and Composite Ceramics (edited by R.E. Tressler, G.L. Messing, C.G. Pantano and R.E. Newnham), Plenum Press, NY (1986).
4. British Ceramic Proceedings No.38, Novel Ceramic Fabrication Processes and Applications, (edited by R.W. Davidge), The Institute of Ceramics, Shelton, Staffs, U.K. (1986).
5. Advances in Ceramics Vol.21, Ceramic Powder Science (edited by G.L. Messing, J.W. Mccanley, K.S. Mazdidasni and R.A. Haber), Am. Ceram. Soc. Inc., Ohio, USA (1987).
6. Ceramic Transactions Vol.1, Ceramic Powder Science IIB (edited by G.L. Messing, E.R. Fuller Jr., H. Hausner), Am. Ceram. Soc., Ohio, USA (1988).
7. Ultrastructure Processing of Advanced Ceramics, (edited by J.D. Mackenzie and D.R. Ulrich) John Wiley & Sons, NY, USA (1988).
8. L.L. Hench in Ultrastructure Processing of Ceramic Glasses and Composites (edited by L.L. Hench & D.R. Ulrich), John Wiley & Sons, NY, USA (1984) pp. 3-5.

9. Material Science Research Vol.21, Ceramic Microstructure '86, Role of Interfaces (edited by Joseph A. Pask and A.G. Evans), Plenum Press, NY, USA (1987).
10. D.R. Ulrich in Ultrastructure Processing of Ceramic Glasses and Composites (edited by L.L. Hench & D.R. Ulrich), John Wiley & Sons, NY, USA (1984) pp.6-11.
11. Material Science Monographs:66A. Proceedings of the 7th International Meeting on Modern Ceramic Technology (7th CIMTEC) World Ceramic Congress, Montecatini, Terme, Italy, 24-30 June 1990 (edited by P. Vincenzini), Elsevier, Amsterdam, Oxford, NY, USA (1991).
12. ibid 66B.
13. ibid 66C.
14. ibid 66D.
15. Principles of Electronic Ceramics (edited by L.L. Hench & J.K. West), John Wiley & Sons, NY, USA (1990).
16. Advanced Ceramics (edited by S. Saito), Oxford Science Publications (1988).
17. N. Ichinose, JEE (1982) 81.
18. H. Yanagida, JEE (1984) 78.
19. R.R. Hirwani, Chem. Business (1987) 45.
20. Ceramic Transactions Vol.15, Materials and Processings for Microelectronic Systems (edited by K.M. Nair, E.I. Dupont de), Am. Ceram. Soc., Ohio, USA (1989).
21. Proceedings of International Conference on Electronic Components and Materials, Nov.7-10, 1989, Beijing, China, Pergamon Press, Oxford, NY, USA (1989).

22. E.G. Acheson, Trans. AIEE 6 (1889) 74.
23. C.T. Allcut, Trans. AIEE 37 (1918) 833.
24. K.B. McEachron, Trans. AIEE 49 (1930) 410.
25. M. Matsuoka, T. Masuyama & Y. Iida, Supl. to Jpn. J. Appl. Phys. 39 (1970) 94.
26. M. Matsuoka, Jpn. J. Appl. Phys. 10 (1971) 736.
27. W.G. Morris, J. Am. Ceram. Soc. 56 (1973) 360.
28. J. Wong, J. Am. Ceram. Soc. 57 (1974) 357.
29. J. Wong, J. Appl. Phys. 46 (1975) 1653.
30. L.M. Levinson and H.R. Philipp, J. Appl. Phys. 46 (1975) 1332.
31. J. Eagan, MRS Bull. 15 (1987) 25.
32. Ceramic Transactions Vol.7, Sintering of Advanced Ceramics (edited by C.A. Handwerker, J.E. Blendell, W.A. Kaysser), Am. Ceram. Soc., Ohio, USA (1988).
33. L. Ketron, Ceram. Soc. Bull. 68 (1989) 860.
34. N. Ichinose, Y. Tanno, Y. Yokomizo, S. Sudo and K. Minami in Advances in Ceramics Vol.I, Am. Ceram. Soc. (1981) pp.375-382.
35. K. Eda in Grain Boundaries in Semiconductors (edited by G.E. Pike, S. Seager and L.M. Leamy), Elsevier Science Publishing Co. Inc., USA (1982) pp.381-392.
36. L.J. Bowen and F.J. Avella, J. Appl. Phys. 54 (1983) 2764.
37. P.M. Vipin, V.V. Sanjaynath, H.K. Varma, K.G.K. Warriier and A.D. Damodaran, J. European. Ceram. Soc. 5 (1989) 233.

38. Y. Suzuoka, A. Okhi, M. Nakagawa, T. Mizutani and M. Ieda, Ceramic Transactions Vol.3, Advances in Varistor Technology (edited by L.M. Levinson), Am. Ceram. Soc. Inc., Ohio (1989) pp.338-345.
39. M. Hyashi and M. Kuramoto, Ceramic Transactions Vol.3, pp.364-370.
40. H. Okuma, T. Sasaki, K. Higashibata, K. Higashibata, S. Horiuchi and F. Ichikawa, Ceramic Transactions Vol.3, pp.371-380.
41. J. Funayama, M. Masuyama, N. Yamaoka, Ceramic Transactions Vol.3, pp.381-386.
42. A. Smith, G. Gasgnier and P. Abelard, J. Am. Ceram. Soc. 73 (1990) 1098.
43. J. Wong and F.P. Bundy, Appl. Phys. Letters 29 (1976) 49.
44. H.R. Philipp and L.M. Levinson, J. Appl. Phys. 52 (1981) 1083.
45. L.M. Levinson, Ceram. Bull. 68 (1989) 866.
46. L.M. Levinson and H.R. Philipp in Ceramic Materials for Electronics (edited by R.C. Buchanan), Marcel Dekker Inc., N.Y. (1986) pp.375-401.
47. M. Sumiyoshi in Ceramic Transactions Vol.3, pp.22-30.
48. J.S. Kresge, E.C. Sakshang, H. Fishman and H.F. Ellis, Ceramic Transactions Vol.3, pp.207-218.
49. M. Kobayashi and M. Mizuno, Ceramic Transactions Vol.3, pp.219-227.
50. P. Kirkby and C.C. Erven, Ceramic Transactions Vol.3, pp.231-239.

51. A. Sweetana, K. Radford, R. Johnson and S. Hensley, Ceramic Transactions Vol.3, pp.240-247.
52. H. Lawatsch and R.S. Perkins, Ceramic Transactions Vol.3, pp.248-255.
53. J. Ozawa, S. Maruyama, S. Shirakawa, K. Nakano and A. Mizukoshi, Ceramic Transactions Vol.3, pp.256-265.
54. N. Nagoka and A. Amentani, Ceramic Transactions Vol.3, pp.266-274.
55. H.F. Nied, Ceramic Transactions Vol.3, pp.274-285.
56. M. Mizuno, Ceramic Transactions Vol.3, pp.286-294.
57. J.E. May, Ceramic Transactions Vol.3, pp.295-305.
58. F.D. Martzloff and T.F. Leedy, Ceramic Transactions Vol.3, pp.306-311.
59. B.I. Wolf, Ceramic Transactions Vol.3, pp.312-317.
60. S.L. Wang, Y.C. Xu, P.Y. Wang, H.F. Li and Z.Y. Zhu, Ceramic Transactions Vol.3, pp.318-324.
61. N. Sohata, M. Nakanishi and K. Utsumi, Ceramic Transactions Vol.3, pp. 329-337.
62. T.K. Gupta, J. Am. Ceram. Soc. 73 (1990) 1817 and references therein.
63. L.M. Levinson and H.R. Philipp in Ceramic Materials for Electronics, Second edition (edited by R.C. Buchanan), Marcel & Dekker Inc., N.Y. (1991) pp.349-377.
64. M.F. Stringfellow, ITEM (1991) 122.
65. JEE Report, March (1992) 66.
66. H.J. Sanders, Chem. Engng. News (1984) 26.

67. H.R. Philipp in Tailoring of Multiphase and Composite Ceramics (edited by R.E. Tressler, G.L. Messing, C.G. Pantano and R.E. Newnham), Plenum Press, N.Y. (1986) pp.481-492.
68. L.M. Levinson and H.R. Philipp, J. Appl. Phys. 46 (1975) 1332.
69. A. Iga, M. Matsuoka and T. Masuyama, Jpn. J. Appl. Phys. 15 (1976) 1847.
70. P.R. Emtage, J. Appl. Phys. 48 (1977) 437.
71. P.L. Hower and T.K. Gupta, J. Appl. Phys. 50 (1979) 4847.
72. W.D. Kingery, J.B. Vandersande and T. Mitamura, J. Am. Ceram. Soc. 62 (1979) 221.
73. M. Inada, Jpn. J. Appl. Phys. 19 (1980) 409.
74. M. Miyayama and H. Yanagida in Ceramic Materials for Electronics, Process, Properties and Analysis (edited by R.C. Buehanan), Marcel and Dekker Inc., N.Y. (1982) pp. 275-280.
75. M. Inada and M. Matsuoka, Advances in Ceramics Vol.7, Additives and Interfaces in Electronic Ceramics (edited by M.F. Yan & A.H. Heur), Am. Ceram. Soc. (1984) pp.91-106.
76. E. Olson, L.K.L. Falk, G.L. Dunlop and R.J. Osterlund, Mat. Sci. 20 (1985) 1847.
77. F. Greuter, G. Blatter, M. Rossinelli and F. Schmuckle in Defects in Semiconductors. Material Science Forum Vol.10-12 (edited by H.J. VonBardleben), Trans. Tech. Publications Ltd., Switzerland (1986) pp.235-240.
78. T. Asokan, G.N.K. Iyengar and G.R. Nagbushana, Br. Ceram. Trans. J. 86 (1987) 190.

79. T.J. Grander, D.H. Doughty, S.J. Lockwood, B.A. Tuttle and J.A. Voight, Ceramic Transactions Vol.3, pp.84-92.
80. Y.C. Chen, C.Y. Shen, H.Z. Chen, Y.F. Wei and L. Wu, J. Mater. Sci. 27 (1992) 1397.
81. L.M. Levinson and H.R. Philipp, Ceram. Bull. 65 (1986) 639.
82. R. Einzinger, Annual Review of Mat. Sci. 17 (1987) 299.
83. K. Eda, IEEE Elect. Ins. 5 (1989) 28.
84. M. Matsuoka, Ceramic Transactions Vol.3, pp.3-9.
85. T.K. Gupta, Engineered Materials Hand Book, Ceramics and Glasses Vol.4, ASM International (1991) pp.1150-1155.
86. A. Lagrange, Electronic Ceramics (edited by BCH Steele), Elsevier Applied Science, N.Y. (1991) pp.1-27.
87. R. Ramaswami, A report, Technology Exchange Network, Bangalore (1990).
88. S. Paul, E10B Indigenisation Status, Telematics India 8 (1989) 10.
89. New Jersey Zinc Co., New York (1957) 100.
90. G. Heiland, E. Mollwo and F. Stockmann, Solid State Physics, Vol.8, Academic Press, New York (1959) 199.
91. W. Jacobowski and D.H. Whitmore, J. Am. Ceram. Soc. 54 (1971) 161.
92. R.C. Neville and C.A. Mead, J. Appl. Phys. 41 (1970) 3795.
93. K. Hauffe and A.L. Vierk, Z. Phys. Chem. 196 (1950) 160.
94. T.K. Gupta and R.L. Coble, J. Am. Ceram. Soc. 51 (1968) 521.
95. S.K. Dutta and R.M. Spriggs, J. Am. Ceram. Soc. 53 (1970) 61.

96. W. Komatsu, Y. Moriyoshi and N. Seto, *Yogyo Kyokai Shi.* 77 (1969) 347.
97. W. Komatsu, H. Ooki, I. Naka and A. Kobayashi, *J.C. Tal* 15 (1969) 43.
98. T.K. Gupta, *J. Am. Ceram. Soc.* 54 (1971) 413.
99. E.E. Hahn, *J. Appl. Phys.* 22 (1951) 855.
100. S.E. Harison, *Phys. Rev.* 93 (1954) 52.
101. T. Masuyama and M. Matsuoka, *Jpn. J. Appl. Phys.* 7 (1968) 438.
102. W.D. Kingery, *Introduction to Ceramics*, John Wiley & Sons, N.Y., USA (1963) 136.
103. H. Yanagida, *J. Elec. Engng.* (1984) 78.
104. D.G. Thomas, *Semiconductors* (edited by N.B. Haunary), Reinhold Publ. Corp., New York (1959).
105. L.M. Levinson and H.R. Philipp, *Appl. Phys. Letters* 24 (1974) 75.
106. J. Wong, P. Rao and E.F. Koch, *J. Appl. Phys.* 46 (1975) 1817.
107. K. Mukae, K. Tsuda and I. Nagaswa, *Jpn. J. Appl. Phys.* 16 (1977) 1361.
108. P.R. Emtage, *J. Appl. Phys.* 48 (1977) 4372.
109. N. Shohata and J. Yoshida, *Jpn. J. Appl. Phys.* 16 (1977) 2299.
110. G. Itakura, A. Takami, T. Kuroda, K. Nagano and M. Matsuoka, *Br. Patent No.1508254*, 20 Aug. 1976.
111. G.D. Mahan, L.M. Levinson and H.R. Philipp, *Appl. Phys. Letters* 33 (1978) 830.



112. J. Wong and F.P. Bundy, High Pressure Science and Technology, Vol.I (edited by K.D. Timmerhaus and M.S. Barber), Plenum Publishing Corp., USA (1979) pp.805-812.
113. M. Matsuoka, Advances in Ceramics, Vol.I, pp.290-308.
114. B. Hoffmann and U. Schwing, Advances in Ceramics, Vol.I, pp.343-347.
115. T.K. Gupta, W.G. Carlson and B.O. Hall, Grain Boundaries in Semiconductors (edited by G.E. Pike, Seager and Leamy), Elsevier Publishing Co. Inc., USA (1982) pp.393.
116. H.R. Philipp and L.H. Levinson, Advances in Ceramics, Vol.7, Additives and Interfaces in Electronic Ceramics, (edited by M.F. Yan and A.H. Heuer), Am. Ceram. Soc. (1984) pp.1-21.
117. S. Sato and Y. Takada, T. Tekumura and M. Ototake, Advances in Ceramics, Vol.7, pp.22-29.
118. T.K. Gupta and W.G. Carlson, Advances in Ceramics, Vol.7, pp.30-40.
119. P. Gaucher, R.L. Perrier and J.P. Ganne, Ceramic Transactions, Vol.3, pp.354-363.
120. S.H. Fan, H.J. Wang, S.L. Wang, Y.C. Xu, Ceramic Transactions, Vol.3, pp.406-412.
121. J.C. Kim and E. Goo, J. Am. Ceram. Soc. 73 (1990) 877.
122. J. Takada, S.I. Hishita and H. Okushi, J. Am. Ceram. Soc. 73 (1990) 1425.
123. T.K. Gupta and W.D. Straub, J. Appl. Phys. 68 (1990) 845.
124. T.K. Gupta and W.D. Straub, J. Appl. Phys. 68 (1990) 851.
125. F.A. Modine, R.W. Major, S.I. Choi, L.B. Bergman and M.N. Silver, J. Appl. Phys. 68 (1990) 339.

126. T. Miyoshi, K. Macda, K. Takahashi and T. Yamazaki, *Advances in Ceramics*, Vol.I, pp.309-315.
127. J.M. Driear, J.P. Guertin, T.O. Sokoly and L.B. Hackney, *Advances in Ceramics*, Vol.I, pp.316-330.
128. K. Mukae and I. Nagaswa, *Advances in Ceramics*, Vol.I, pp.331-341.
129. H. Okuma, N. Amiji, M. Suzuki and Y. Tanno, *Advances in Ceramics*, Vol.7, pp.41-49.
130. T. Takamura, M. Kobayashi, Y. Takada and K. Sato, *Advances in Ceramics*, Vol.7, pp.50-59.
131. M.A. Seitz, F. Hampton and W. Richmond, *Advances in Ceramics*, Vol.7, pp.60-70.
132. M. Tronteg, D. Kolar and V. Krasevec, *Advances in Ceramics*, Vol.7, pp.107-116.
133. M. Castongury, B. Fernandez, F. Guillon and J.D.N. Cheeke, *J. Appl. Phys.* 61 (1987) 5199.
134. T. Asokan, G.N.K. Iyengar, G.R. Nagbushana, *J. Mater. Sci.* 22 (1987) 1019.
135. T. Asokan, *Br. Ceram. Trans. J.* 86 (1987) 187.
136. F.A. Modine and H.M. Hyatt, *J. Appl. Phys.* 64 (1988) 4229.
137. J.P. Gambino, W.D. Kingery, G.E. Pike, L.M. Levinson and H.R. Philipp, *J. Am. Ceram. Soc.* 72 (1989) 642.
138. H.C. Ling, M.F. Yan and W.W. Rhodas, *J. Am. Ceram. Soc.* 72 (1989) 1274.
139. G.Y. Sung and C.H. Kim, *Ceramic Transactions*, Vol.3, pp.101-108.

140. M. Trontej and V. Krasevec, *Ceramic Transactions*, Vol.3, pp.108-116.
141. P. Gaucher, R.L. Perrier and J.P. Ganne, *Ceramic Trans.*, Vol.3, pp. 354-363.
142. C.S. Furtado, A.R. Ferreira and J.M. Perdigao, *Ceramic Transactions*, Vol.3, pp.387-394.
143. I.R. Krstanovic, A.A. Radakovic and M.M. Ristic, *Ceramic Transactions*, Vol.3, pp.431-435.
144. N. Raghu and T.R.N. Kutty, *J. Mater. Sci. in Electronics* 1 (1990) 84.
145. Y. Chung Chen, C.Y. Shen, H.Z. Chen, Y.F. Wei and L. Wu, *Jpn. J. Appl. Phys.* 30 (1991) 84.
146. N. Raghu and T.R.N. Kutty, *Appl. Phys. Lett.* 58 (1991) 1050.
147. M.N. Rahman, L.C. Dejonghe and M.Y. Chu, *J. Am. Ceram. Soc.* 74 (1991) 514.
148. Y. Sakashita, T. Ono, H. Segawa, K. Tominaga and M. Okada, *J. Appl. Phys.* 69 (1991) 8352.
149. J.M. Wu and C.H. Lai, *J. Am. Ceram. Soc.* 74 (1991) 3112.
150. A.B. Alles and V.L. Burdick, *J. Appl. Phys.* 70 (1991) 6883.
151. T.R.N. Kutty and N. Raghu, *Matr. Sci. Engg.* B13 (1992) 181.
152. A. Shrivastava, P. Singh, V.G. Gunjekar and C.I. Jose, *Thermochim. Acta* 76 (1984) 249.
153. P. Singh and S.K. Date, *J. Mat. Sci. Lett.* 6 (1987) 621.
154. A. Srivastava, P. Singh and A. Mitra, *Mat. Lett.* 5 (1987) 269.

155. P. Singh, S.R. Sainkar, V.G. Gunjekar, M.V. Kuber, R.F. Shinde and S.K. Date, *Mat. Lett.* 9 (1990) 65.
156. P. Singh, *J. Mat. Sci. Lett.* 9 (1990) 613.
157. K. Eda, M. Inada and M. Matsuoka, *J. Appl. Phys.* 54 (1983) 1095.
158. P. Palaniswamy and T. Ashokan, *Am. Ceram. Soc. Bull.* 67 (1988) 1695.
159. G.S. Snow, S.P. White, R.A. Cooper and R. Amijo, *Am. Ceram. Soc. Bull.* 59 (1980) 617.
160. G.S. Snow and R.A. Cooper, *Am. Ceram. Soc. Bull.* 59 (1980) 550.
161. R.J. Lauf and W.D. Bond, *Ceram. Bull.* 63 (1984) 278.
162. R.G. Dosch, *Science of Ceramic Chemical Processing* (edited by L.L. Hench and D.R. Ulrich), John Wiley & Sons, N.Y. (1986) pp.311-319.
163. T.K. Gupta, *J. Mat. Res.* 2 (1987) 231.
164. T. Asokan, G.N.K. Iyengar and G.R. Nagbushana, *J. Am. Ceram. Soc.* 70 (1987) 643.
165. T.K. Gupta and A.C. Miller, *J. Mater. Sci.* 3 (1988) 745.
166. S.M. Haile, D.W. Johnson Jr., G.H. Wiseman and H.K. Bowen, *J. Am. Ceram. Soc.* 72 (1989) 2004.
167. (a) L. Ruixia, W. Peiyong and W. Shiliang, *Ceramic Transactions*, Vol.3, pp.117-120.  
(b) G. Hohenberger, G. Tomandal, R. Ebert and T. Taube, *J. Am. Ceram. Soc.* 74 (1991) 2067.

168. O. Milosivic, D. Vasovic, D. Poteti, L. Karanovic, V. Petrovic and D. Uskokovic, Ceramic Transactions, Vol.3, pp.395-405.
169. H.V. Tran, Ceramic Transactions, Vol.3, pp.420-424.
170. L. Fuyi, R. Wene and J. Xingliu, Ceramic Transactions, Vol.3, pp.425-430.
171. M.Y. Chu, L.C. De.Jonghe, M.K.F. Lin and F.J.T. Lin, J. Am. Ceram. Soc. 74 (1991) 2902.
172. S.C. Yang and R.M. German, J. Am. Ceram. Soc. 74 (1991) 3085.
173. News Adv. Ceram. Mat. 1 (1986) 7.
174. D.R. Clarke, J. Appl. Phys. 49 (1978) 2407.
175. A.T. Santharaman, T.K. Gupta and W.G. Carlson, J. Appl. Phys. 50 (1979) 852.
176. L.M. Levinson, H.R. Philipp and E. Sonder in Material Science Research Vol.21, Ceramic Microstructure 86 - Role of interfaces (edited by A.P. Joseph and A.G. Evans), Plenum Press, New York (1987) pp.665-678.
177. E.O. Olson and G.L. Dunlop, Material Science Research Vol.21, pp.679-686.
178. H. Kenya, N. Zenbe, O. Yoshiaki, S. Akio and M. Tatsuro, Material Science Research Vol.21, pp.687-695.
179. M. Maturra and H. Yamoki, Jpn. J. Appl. Phys. 16 (1977) 1261.
180. K. Mukae and I. Nagaswa, in Grain Boundary Phenomenon in Electronic Ceramics Vol.I, pp.331-342.
181. M. Tao, B. Ai, O. Dorlanne and A. Loubiere, J. Appl. Phys. 61 (1987) 1562.

182. T. Asokan, G.N.K. Iyengar and G.R. Nagbhushana, *J. Mater. Sci.* 22 (1987) 2229.
183. E. Olsson and G.L. Dunlop, *J. Appl. Phys.* 66 (1989) 4317.
184. E. Olsson, G.L. Dunlop and R. Osterlund, *Ceramic Transactions*, Vol.3, pp.57-64.
185. E. Olsson and G.L. Dunlop, *Ceramic Transactions*, Vol.3, pp.65-72.
186. M. Kobayashi, T. Takemura and Y. Takada, *Ceramic Transactions*, Vol.3, pp.73-83.
187. H. Cerva and W. Russwurm, *Ceramic Transactions*, Vol.3, pp.93-100.
188. D.F.K. Hennings, R. Hartung and P.J.L. Reijnen, *J. Am. Ceram. Soc.* 73 (1990) 645.
189. S.R. Sainkar, S. Badrinarayanan, A.P.B. Sinha and S.K. Date, *Surf. Inter. Anul.* 3 (1981) 142.
190. S.R. Sainkar and A.P.B. Sinha, *Indian J. Pure Appl. Phys.* 23 (1985) 87.
191. S.R. Sainkar, S. Badrinarayanan, A.P.B. Sinha and S.K. Date, *Appl. Phys. Lett.* 39 (1981) 65.
192. E.M. Levin and R.S. Roth, *J. Res. Nat., Burstand* 68A (1964) 189.
193. G. Malmors, *Acta Chem. Scand* 24 (1970) 384.
194. T.K. Gupta and R.C. Coble, *J. Am. Ceram. Soc.* 51 (1968) 521.
195. J. Wong and W.G. Morris, *Am. Ceram. Soc. Bull.* 53 (1974) 816.

196. A. Iga, M. Matsuoka and T. Masuyama, *Jpn. J. Appl. Phys.* 15 (1976) 1161.
197. M. Inada, *Jpn. J. Appl. Phys.* 17 (1978) 1.
198. J.W. Mederanch and R.L. Snyder, *J. Am. Ceram. Soc.* 61 (1978) 494.
199. C.N.R. Rao, G.V.S. Rao and S. Ramdas, *J. Phys. Chem.* 73 (1969) 672.
200. A.R. Huston, *J. Phys. & Chem. Solids*, 8 (1959) 467.
201. N.Y. Lee, M.S. Kim, J.J. Chung and M.H. Oh, *J. Mater. Sci.* 25 (1990) 1.
202. E.M. Levin, C.R. Robins and H.F. McMuride, *Am. Ceram. Soc.* (1964) 127.
203. R.M. Biefold and S.S. White, *J. Am. Ceram. Soc.* 64 (1981) 182.
204. R. Einzinger, *Appl. Surf. Sci.* 3 (1979) 390.
205. D.R. Clarke, *J. Am. Ceram. Soc.* 63 (1980) 339.
206. P.R. Emtage, *J. Appl. Phys.* 50 (1979) 6833.
207. D.R. Clarke, *J. Appl. Phys.* 50 (1979) 6829.
208. N. Shohata, T. Matsumura, K. Utsumi and T. Ohno, *Advances in Ceramics, Vol.I*, pp.349-358.
209. R.Einginger, *Advances in Ceramics, Vol.I*, pp.359-374.
210. H.R. Philipp and L.M. Levinson, *Advances in Ceramics, Vol.I*, pp.394-414.
211. W.D. Kingery, *Advances in Ceramics, Vol.I*, pp.1-15.
212. K. Okazaki, *Advances in Ceramics, Vol.I*, *ibid* pp.23-27.
213. D.R. Clarke, *Advances in Ceramics, Vol.I*, pp.67-90.
214. P.F. Bongers and E.C. Franken, *Advances in Ceramics, Vol.I*, pp.38-52.

215. T.G. Strutton, D. Reed and H.L. Tuller, *Advances in Ceramics*, Vol.I, pp.114-123.
216. M.A. Seitz and W. Orlow, *Advances in Ceramics*, Vol.I, pp.124-129.
217. D.A. Yuwang and A.S. Nowick, *Advances in Ceramics*, Vol.I, pp.130-137.
218. Y.M. Chiang, A.F. Henriksen, W.D. Kingery and D. Finello, *J. Am. Ceram. Soc.* 64 (1981) 385.
219. S.J. Bennison and M.P. Haruner, *Advances in Ceramics*, Vol.6, (edited by M.F. Yen and A.H. Huner), *Am. Ceram. Soc.*, USA (1982) pp.171-183.
220. J. Dodgworth, C.B. Carter and D.L. Kohlstedt, *Advances in Ceramics*, Vol.6, pp.73-85.
221. K. Eda, M. Inada and M. Matsuoka, *J. Appl. Phys.* 54 (1983) 1095.
222. J.P. Gambino, W.D. Kingery, G.E. Pike, H.R. Philipp and L.M. Levinson, *J. Appl. Phys.* 61 (1987) 2571.
223. T.K. Gupta, W.D. Straub, M.S. Ramanachalam, J.P. Schaffer and R.A. Rohatgi, *J. Appl. Phys.* 66 (1989) 6132.
224. T. Senda and R.C. Brad, *J. Am. Ceram. Soc.* 73 (1990) 106.
225. T.K. Gupta, *Ceramic Transactions*, Vol.15, *Materials and Processing for Electronic Systems* (edited by K.M. Nair, R. Pokhana and R.C. Buchanan), *Am. Ceram. Soc. Inc.*, Ohio, USA (1990) pp.711-727.



226. H.C. Ling, Ceramic Transactions, Vol.8, Ceramic Dielectrics: Composition, Processing and Properties (edited by H.C. Ling and M.F. Yan), Am. Ceram. Soc. Inc., USA (1990) pp.253-260.
227. Y. Chung Chen, C. Yen Shen and L. Wu, J. Appl. Phys. 69 (1991) 8363.
228. T. Senda and R.C. Brad, J. Am. Ceram. Soc. 74 (1991) 1296.
229. L. Wu, C.Y. Shen, Y.C. Chen, Y.F. Wei, M.H. Chen and K.C. Huang, Jpn. J. Appl. Phys. 30 (1991) 2850.
230. T. Sone, H. Akagi and H. Watarai, J. Am. Ceram. Soc. 74 (1991) 3151.
231. W.G. Carlson and T.K. Gupta, J. Appl. Phys. 53 (1982) 5746.
232. Y.L. Tsai, C.L. Huang and C.C. Wei Taiman, J. Mat. Sci. Lett. 4 (1985) 1305.
233. M. Takata, D. Tsubone and H. Yanagida, J. Am. Ceram. Soc. 59 (1976) 4.
234. W.C. Stewart, J. Appl. Phys. 45 (1974) 452.
235. M. Fix and J. Sohn, Appl. Phys. Lett. 26 (1975) 519.
236. H.R. Philipp and L.M. Levinson, J. Appl. Phys. 46 (1975) 3206.
237. J. Bernasconi, H.P. Klein, B. Knecht and S. Strassler, J. Elect. Mat. 5 (1976) 473.
238. K. Eda and M. Matsuoka, Jpn. J. Appl. Phys. 16 (1977) 195.
239. K. Eda, J. Appl. Phys. 49 (1978) 2964.
240. K. Eda, J. Appl. Phys. 50 (1979) 4436.
241. L.K.J. Vandamma and J.C. Brugman, J. Appl. Phys. 5 (1980) 4240.

242. K. Eda, M. Inada and M. Matsuoka, J. Appl. Phys. 54 (1987) 1095.
243. A. Kusy and T.G.M. Kleinpenning, J. Appl. Phys. 54 (1983) 2900.
244. M. Prudenziati, A. Masoero and A.M. Rietto, J. Appl. Phys. 58 (1985) 345.
245. F. Greuter, G. Blatter, F. Stucki and M. Rossinelli, Ceramic Transactions, Vol.3, pp.31-53.
246. G.D. Mahan, Grain Boundaries in Semiconductors (edited by H.J. Leamy, G.E. Pike and C.H. Seager), North Holland, New York, USA (1982) pp.85-98.
247. K. Eda, Ceramic Transactions, Vol.3, pp.10-21.
248. R.G. Dosch, B.A. Tuttle and R.A. Brooks, J. Mater. Res. 1 (1986) 90.
249. French Patent No.86 16803, 2 December, 1986.
250. H. Tran, G. Djega-Mariadasson and A. Lagrange in 2nd International Conference on Passive Components, Paris, (1987).
251. K. Seitz, E. Ivers-Tiffe, H. Thomann and A. Weiss, Influence of Zinc Acetate and Nitrate Salts on the Characteristics of Undoped ZnO Powders, Elsevier, Amsterdam, (1986).
252. G. Hohenberger and G. Tomandl, J. Mat. Sci. Res. 7 (1992) 546.
253. S.R. Sainkar, Ph.D. Thesis, University of Poona (1981).
254. A. Srivastava, Ph.D. Thesis, University of Poona (1985).

255. T. Asokan, Ph.D. Thesis, Indian Institute of Science, Bangalore (1986).
256. G.H. Heiland and E. Mollwo, Solid State Physics, Vol.8 (edited by F. Seitz and D. Turhaball), Academic Press, N.Y., USA (1959).
257. C. Whiston, X-ray Methods (edited by F.E. Prichard), J. Wiley & Sons, USA (1987).
258. G. Lawcs, Scanning Electron Microscopy and X-ray Microanalysis (edited by A.M. James), John Wiley & Sons, USA (1987).
259. A Guide to Materials Characterizations and Chemical Analysis (edited by J.P. Sibilias), VCH Publishers Inc., N.Y., USA (1988).
260. Impedance Spectroscopy (edited by J.R. Macdonald), John Wiley & Sons, USA (1987).
261. Ceramic Transition, Vol.3, Advances in Varistor Technology (edited by L.M. Levinson), Am. Ceram. Soc. Inc., Ohio, USA (1989).
262. B.A. Boukamp, Equivalent Circuit Software, Twente University, Netherlands.
263. ASTM card No.5-0664.
264. ASTM card No.6-0294.
265. ASTM card No.6-0312.
266. Practical Surface Analysis by Auger and X-ray Photoelectron Spectroscopy (edited by D. Briggs and M.P. Seah), John Wiley & Sons, New York, U.S.A. (1983).
267. ASTM card No.4-0829.

*CHAPTER - 4*

**AC IMPEDANCE MEASUREMENT**  
**AND ANALYSIS**

#### 4.1 Impedance Spectroscopy

Impedance Spectroscopy (IS) is a valuable technique used for the characterization of inhomogeneous electrical and magnetic materials exhibiting granular structures [1]. It employs different frequency dependence of the constituent components like bulk, grain, grain boundaries and electrode interfaces, etc. for their separation. The response of these components takes the form of electrical relaxations and can be modeled using simple RC (Resistance-Capacitance) parallel circuit elements. Each electrical component has its own characteristic relaxation time, given by the magnitude of RC product and can be separated in the frequency domain.

Impedance spectroscopy is becoming a popular analytical tool in material research and developments because, (i) it involves simple electrical measurements, and; (ii) can be automated easily. The results obtained from impedance spectroscopy can be correlated with many complex material variables like mass transport, dielectric properties, microstructure (grain, grain boundaries, intergranular layers and electrode interfaces) and compositional influences, etc. It gives direct access to establish the property-correlationship between the functional and electrical microstructure of any variety of granular structures. To differentiate between the varying contributions from grains, grain boundaries, intergranular layers and electrode interfaces, AC impedance measurements

are often used with great success [2-7]. In favourable cases, the difference in impedance responses originating from the different regions of granular ceramics can be explained using simple RC parallel and series circuit elements. Analysis of such a random network of elements allowed researchers to establish processing structure-property relationship in a variety of granular ceramics such as manganese-zinc (Mn-Zn) ferrites [8-9], nickel-zinc (Ni-Zn) ferrites [10-11], PTC thermistors [12-14], grain boundary layer (GBL) capacitors [15], various multilayer structures [16-17], and varistors [18-19].

#### 4.2 AC Impedance Measurement Techniques

In AC impedance spectroscopic measurements, a time dependent voltage  $\Delta E \sin(\omega t)$  ( $\Delta E \approx 100-300$  mV) is generally applied across the inhomogeneous ceramic specimen. A sinusoidal current flows through the specimen with same angular frequency  $\omega$  ( $\omega = 2\pi f$ ). The input and output have the same form and the magnitude of the output response is directly proportional to the electrical stimulus. At a particular frequency, there is a linear relationship between the input and the output signals. The output signal is compared with the input signal to determine impedance modules and phase shift. The impedance of a linear circuit is given by the ratio of the voltage to the current flowing through it and composed of two components e.g. real and imaginary impedances respectively.

The data is computed and displayed in a complex plane in a form of real and imaginary components. The common representations used in impedance spectroscopic analyses are, (i) complex impedance ( $Z^*$ ), (ii) complex admittance ( $Y^*$ ), (iii) complex permittivity ( $\epsilon^*$ ), and; (iv) complex modulus ( $M^*$ ). The interrelationship between these four basic immittance functions are:

$$Z^* = Z' - jZ'' \quad . \quad . \quad . \quad . \quad . \quad (4.1)$$

$$Y^* = \frac{1}{Z^*} = Y' + jY'' \quad . \quad . \quad . \quad . \quad . \quad (4.2)$$

$$\epsilon^* = \frac{1}{j\omega Z^*} = \epsilon' - j\epsilon'' \quad . \quad . \quad . \quad . \quad . \quad (4.3)$$

$$M^* = j\omega Z^* = M' + jM'' \quad . \quad . \quad . \quad . \quad . \quad (4.4)$$

These relationships form the basis of complex plane analysis techniques.

#### 4.3 Complex Plane Analysis

In the complex plane analysis, all R,L,C (Resistive, capacitive and inductive) networks can be reduced into two component parallel combination ( $R_p, C_p$ ) or a corresponding two component series combination ( $R_s, C_s$ ). For the series combination, the equivalent impedance is given by,

$$Z^* = R_s + \frac{1}{j\omega C_s} = R_s - \frac{j}{\omega C_s} \quad . \quad . \quad . \quad . \quad . \quad (4.5)$$

Similarly for parallel combination,

$$Z^* = \left[ \frac{1}{R_p} + j\omega C_p \right]^{-1} \dots \dots \dots (4.6)$$

$$= \frac{R_p}{1 + j\omega C_p R_p} = \frac{R_p - j\omega C_p R_p^2}{1 + \omega^2 C_p^2 R_p^2}$$

$$= \frac{R_p}{1 + \omega^2 C_p^2 R_p^2} - \frac{j\omega C_p R_p^2}{1 + \omega^2 C_p^2 R_p^2} \implies Z' - jZ'' \dots \dots (4.7)$$

$$= \frac{R_p}{1 + \omega^2 C_p^2 R_p^2} - j\omega C_p \frac{R_p^2}{1 + \omega^2 C_p^2 R_p^2}$$

$$= \frac{R_p}{1 + Q^2} - \frac{j\omega C_p}{\omega^2 C_p^2} \cdot \frac{Q^2}{1 + Q^2} \quad \text{as } Q = \omega \cdot C_p \cdot R_p$$

$$Z^* = \frac{R_p}{1 + Q^2} - \frac{j}{\omega C_p} \cdot \frac{Q^2}{1 + Q^2} \dots \dots \dots (4.8)$$

Equation (4.6) and (4.8) give the relationship between the equivalent parallel and series components as,

$$R_s = \frac{R_p}{1 + Q^2} \dots \dots \dots (4.9)$$

$$C_s = C_p \cdot \frac{1 + Q^2}{Q^2} \dots \dots \dots (4.10)$$

Equation (4.6) may be rewritten as,

$$\frac{1}{Z^*} = \frac{1}{R_p} + j\omega C_p$$

or,  $Y = G_p + j\omega C_p \dots \dots \dots (4.11)$



Therefore comparing (4.5) and (4.11) with (4.1) and (4.2) we get,

$$Z' = R_S; Z'' = \frac{1}{\omega C_S}$$

$$Y' = G_P \cdot \left(\frac{1}{R_P}\right); Y'' = \omega C_P \quad . . . . . \quad (4.12)$$

Similarly,  $\epsilon' = C_P; \epsilon'' = \frac{G_P}{\omega}$  and . . . . . (4.13)

$$M' = \frac{1}{C_S}; M'' = \omega R_S \quad . . . . . \quad (4.14)$$

The impedance data usually obtained experimentally as a simultaneous values, at a particular frequency, of resistance and capacitance either in a parallel or series two component configuration. In general, these data actually represent a more complex network and the reduced values ( $R_S, C_S$  or  $G_P, C_P$ ) are combination of the individual network components; the contribution of any given component being dependent on frequency of measurement. Complex plane analysis is a mathematical technique which allows the determination of the individual component values from reduced data obtained over a range of frequencies. It involves, simply, the plotting, one against the other, of the real and imaginary parts of the complex electrical quantities described above i.e.  $Z^*, Y^*, \epsilon^*$  and  $M^*$ , as a frequency dispersion. The subsequent plots are characteristic of particular equivalent circuits and ideally consists of a combination of semicircles and

straight lines. Intercepts with the real axis and frequency values at maximum or minimum positions lead to the single component values. To understand the above concept, we have from equation (4.7)

$$1 + w^2 R_P^2 C_P^2 = \frac{R_P}{Z'} \quad \dots \dots \dots (4.15)$$

$$w^2 C_P^2 R_P^2 = \left( \frac{R_P}{Z'} - 1 \right)$$

$$w^2 = \frac{1}{C_P^2 R_P^2} \left( \frac{R_P}{Z'} - 1 \right)$$

$$w = \frac{1}{C_P \cdot R_P} \sqrt{\left( \frac{R_P}{Z'} - 1 \right)} \quad \dots \dots \dots (4.16)$$

Using equations (4.15) and (4.16) in equation (4.7) we get,

$$Z'' = \frac{\frac{1}{C_P R_P} \cdot \sqrt{\left( \frac{R_P}{Z'} - 1 \right)} \cdot C_P R_P^2}{R_P / Z'} = Z' \cdot \sqrt{\left( \frac{R_P}{Z'} - 1 \right)}$$

Squaring on both sides we get,

$$Z''^2 = Z'^2 \cdot \left( \frac{R_P}{Z'} - 1 \right) = Z'^2 \left( \frac{R_P - Z'}{Z'} \right) = Z' (R_P - Z')$$

$$= Z' R_P - Z'^2$$

$$Z''^2 - Z' R_P + Z'^2 = 0$$

$$Z'^2 - Z' R_P + Z''^2 = 0$$

Rearranging the terms and adding  $\frac{R_p}{4}$  on both the sides

we get,

$$Z'^2 - Z'R_p + \frac{R_p}{4} + Z''^2 = \frac{R_p}{4}$$

$$(Z' - \frac{R_p}{2})^2 + Z''^2 = \frac{R_p}{4} \quad \dots \dots \dots (4.17)$$

Equation (4.17) represents an equation of a circle with radius  $R_p/2$  and centre at  $(\frac{R_p}{2}, 0)$ . The coordinates at the top (summit) of the arc are  $(R_p/2, R_p/2)$ . Therefore at a particular frequency  $w_o$  we have,

$$Z' = \frac{R_p}{2} = \frac{R_p}{(1 + w_o^2 C_p^2 R_p^2)} \quad \dots \dots \dots (4.18)$$

and  $Z'' = \frac{R_p}{2} = \frac{w_o^2 C_p \cdot R_p^2}{(1 + w_o^2 C_p^2 R_p^2)} \quad \dots \dots \dots (4.19)$

Rearranging equation (4.18) and (4.19) we get,

$$w_o C_p \cdot R_p = 1 \quad \text{Or} \quad W_o = \frac{1}{C_p \cdot R_p} \quad \dots \dots \dots (4.20)$$

Thus impedance response of a resistor connected in parallel with a capacitor is a perfect semicircle intersecting the real axis at  $R_p$  and 0 (origin). The relaxation time ( $\tau_o = R_p C_p$ ) for the circuit is given by the inverse of the frequency at the top (summit) of the semicircle. AC

impedance analysis studies give direct access for the calculation of these immittance parameters across the grains, grain boundaries, intergranular layers, and the electrode interfaces of the granular structures.

#### 4.4 Electrical Characterization of 10 mol% MgO Doped ZnO Based Varistors

As discussed in chapter-III of the thesis, it is confirmed that the improved performance parameters in a judiciously modified varistors are due to the addition of 10 mol% MgO and its subsequent processing [20-21]. The improvement was found to be closely related to the ceramic microstructure (functional) and various processing parameters. The I-V characteristics of the modified varistor have shown:

- (i) Breakdown electric field  $E_b$  ( $1\text{mA}/\text{cm}^2$ )  $\approx 1000$  V/mm and;
- (ii) nonlinear coefficient  $\alpha \approx 29$ .

SEM studies have shown the improved functional microstructure e.g. uniform, closely packed grains with well defined grain boundaries associated with voids. On the other hand, XRD studies on these varistors have not shown the presence of any other additional complex (bulk) phase formed during sintering. To resolve this dilemma and to differentiate between varying contributions from grains, grain boundaries/intergranular layers and electrode interfaces, AC impedance spectroscopy was thought of as an invaluable tool due to high sensitivity of microstructural

changes.

The electrical properties of these varistors are primarily influenced by double Schottky barriers located in the region of ZnO grains and intergranular layers [22-23]. Recent modeling of grain boundary (GB) phenomena in the varistors have predicted the associated charge depletion layers which have been confirmed by a variety of physico-chemical characterization techniques [24-26]. Some researchers have reported that these barriers are responsible for the dispersion of the real and imaginary parts of complex impedance and for the nonlinearity of the current-voltage (I-V) characteristics [27-32]. Usually three different processes take place during charge transport through the barriers. (i) Bulk conduction or intra-grain conduction; (ii) conduction across the grain boundary; and (iii) transport across the electrode-interface. In impedance analysis techniques, each of these processes are represented by independent RC combination and depending upon the relative values of their relaxation times they give rise to three independent semicircular arcs in the impedance plot. Usually the highest frequency arc corresponds to the bulk conduction, the intermediate one to the grain boundary conduction and the lowest frequency one to the interface process. The resistance values of the circuit elements are obtained from the real axis intercept while the capacitance values are obtained from the frequency corresponding to highest point in each

semicircle.

To establish a working relationship, electrical microstructure of a functionally modified ZnO based varistor compositions was investigated using ac impedance spectroscopic analysis method discussed in chapter-II in the frequency range of 1Hz-10MHz over the temperature range of 25-250°C. The grain and grain boundary impedance values have been extracted from the real and imaginary impedance ( $Z' \rightarrow Z''$ ) plots [33]. The temperature dependence of real and imaginary parts of  $Z^*$  (Total impedance) have been studied to understand the role of activation energies across the each network elements. The experimental data and its analysis are discussed in the present chapter.

#### 4.5 Results and Discussion

For the comparative evaluation, the pellets of ZBCM and ZBCM-10 MgO varistor systems (air sintered at 1050°C/1 hr) were used. The optimal sintered temperature (1050°C) was selected because the ZBCM-10 MgO varistor has shown the improvement in the functional microstructure and hence the electrical performance parameters [21]. Fig.4.1(a)-4.1(b) and Fig.4.2(a)-4.2(b) show the complex plane plots for these two types of varistor systems. For clarity and easy analysis, the plots have been split into two parts - experimental data in low and high temperature ranges. It is seen from Fig.4.1(a) that in the case of ZBCM varistor studied at room temperature, only a part of the semicircle

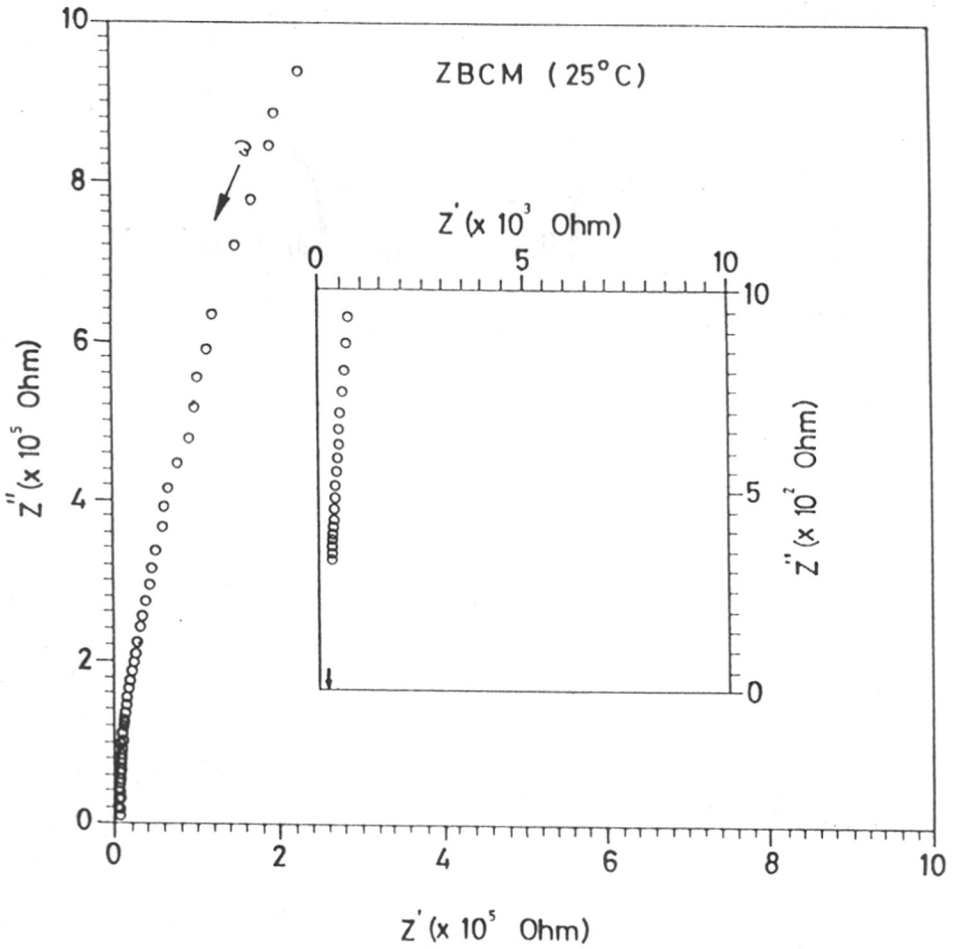


Fig. 4.1(a) Complex impedance plot for ZBCM varistor at 25°C.

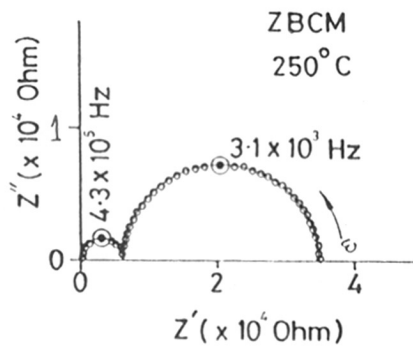
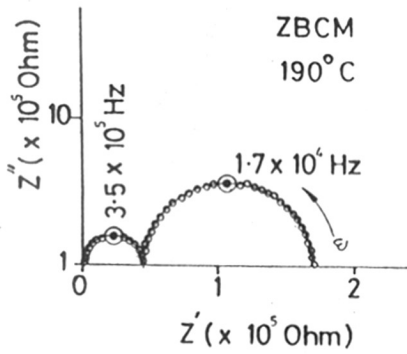
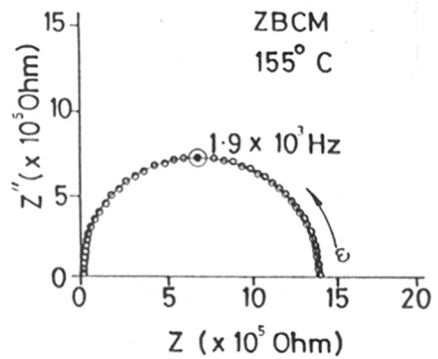
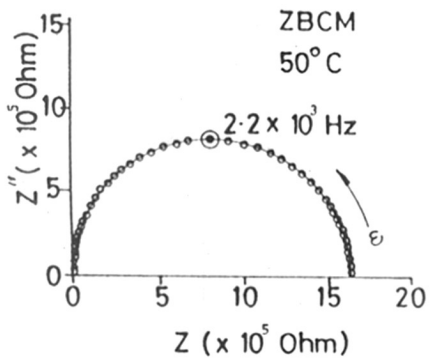


Fig. 4.1(b) Complex impedance plots for ZBCM varistor at 50, 155, 190 and 250°C.



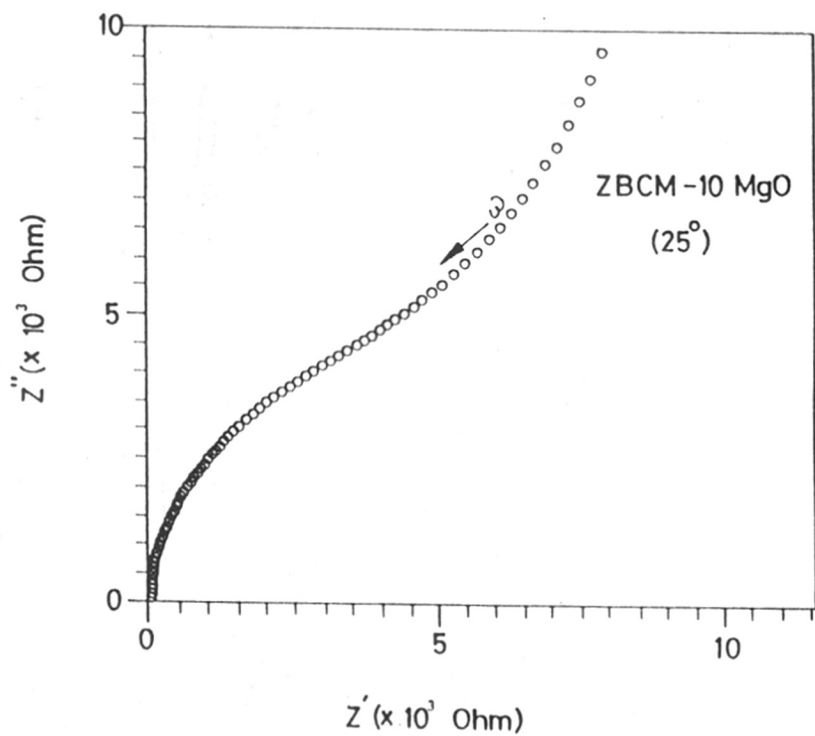


Fig. 4.2(a) Complex impedance plot for ZBCM-10MgO varistor at 25°C.

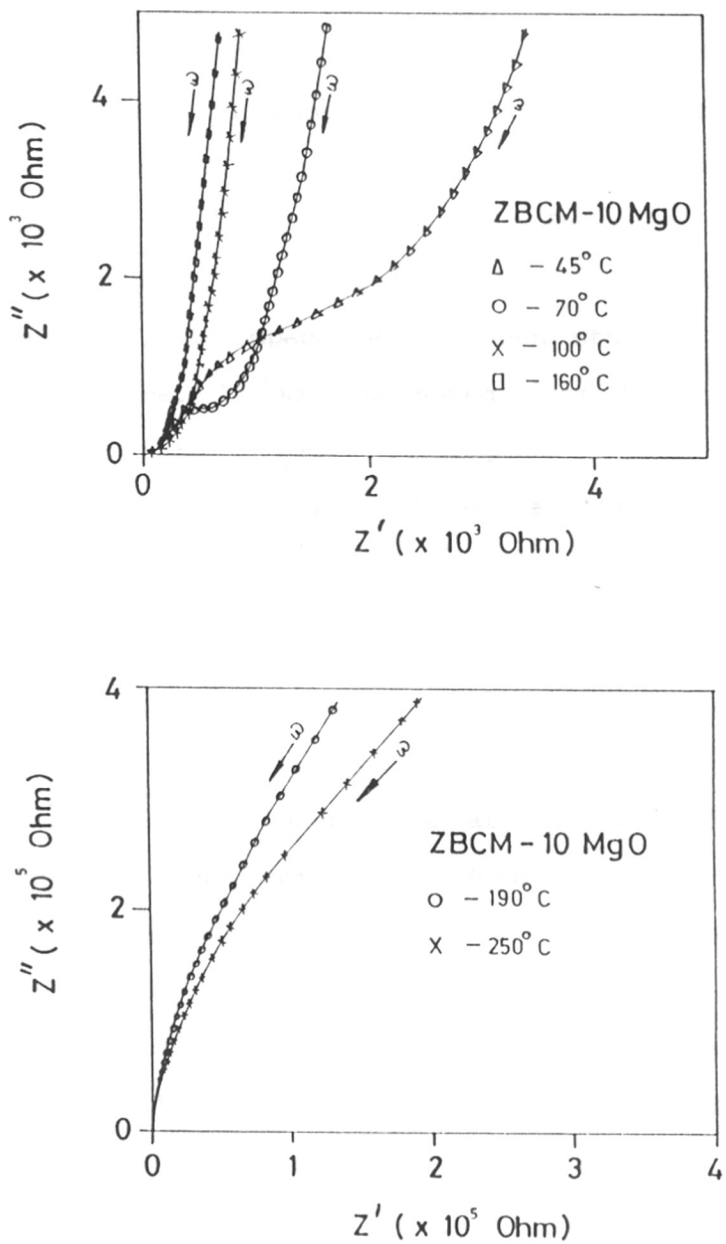


Fig. 4.2(b) Complex impedance plots for ZBCM-10 MgO varistor at 45, 70, 100, 160, 190 and 250°C.

is observed because of high sample impedance and the limits of measuring instruments. The high frequency part of the semicircular arc does not pass through origin indicating the presence of small bulk resistance of the ZnO grain (clearly shown in insert) in the order of 10-20 ohms. Similar values for the bulk ZnO grain resistance have been reported in the literature[34-35]. In order to expand the frequency window and study the other dispersions present in the material, AC impedance has been studied as a function of temperature. It may be noted from Fig.4.1(b) that at room temperature(25°C), only a part of the semicircle is visible. As the temperature increases the imaginary part of the impedance tends to zero at lower frequency, showing that the silver electrodes are nonblocking and the ZnO is an electronic conductor.

At a first glance, there seems to be only one semicircle but a closer look at the high frequency data reveals that the semicircle does not pass through the origin. The observed arc is identified as a grain boundary property since it does not pass through the origin. This observation is supported by the capacitance associated with this arc which is  $\approx 0.50$  nF/cm, typical for grain boundary semicircle.

As the temperature is increased, the semicircle observed at room temperature further resolves into two semicircles with high frequency intercept still showing a nonzero resistance but of lower magnitude. The additional

semicircle has been attributed to the intergranular phase [36]. The magnitude of the capacitance is again of the order of  $\approx$  nf/cm, asserting that it is a grain boundary dispersion. The overall dispersion in the ZBCM varistor system (combining room temperature and high temperature data) includes, (i) pure ZnO (bulk) grain resistance ( $R_{ZnO}$ ), (ii) grain boundary resistance ( $R_{gb}$ ), and; (iii) intergranular phase resistance ( $R_{gi}$ ). The electrical response of this varistor system is described by a series of a parallel combination of the network chain of RC (Resistance-Capacitance) elements. The resultant electrical equivalent circuit is therefore a combination of two parallel RC circuit elements connected in series with a bulk ZnO grain resistance  $R_{ZnO}$ ,  $R_{gb}-C_{gb}$  for grain boundary and  $R_{gi}-C_{gi}$  for grain interface, as shown in the Fig.4.3(a). The complex impedance dispersion of the equivalent circuit is the superposition of semicircles corresponding to the two lumped circuits which satisfies the condition that  $\omega RC \approx 1$ . Similar electrical equivalent circuits are reported for ZnO varistors in the literature[37-40]. The typical values of the lumped immittance parameter are summarised in Table 4.1.

The nF/cm values for the capacitance ( $C_{gb}$  and  $C_{gi}$ ) are typical of grain boundaries and grain interfaces respectively. It can be seen that these RC circuit elements operate at different time constants with reference to the operating frequencies.

**Table-4.1:** Immittance Parameters for ZBCM Varistor

Temp. °C	$R_{ZnO}$ Ohm	$R_{gb}$ X $10^5$ ohm	$C_{gb}$ X nF/cm	$R_{gi}$ X $10^5$ ohm	$C_{gi}$ X nF/cm
50	-	16.0	0.50	-	-
140	7.6	16.5	0.48	-	-
155	4.7	14.0	0.66	-	-
190	3.9	0.50	0.10	2.25	0.46
250	-	0.08	0.51	0.36	0.16

When 10 mol% MgO is doped in a simple ZBCM varistor system, the complex plane plots show an interesting change. It can be seen from Fig.4.2(a)-4.2(b) that the high frequency arc of a semicircle does not pass through the origin implying the presence of small ZnO (bulk) resistance, similar to ZBCM varistors. In this case, there is a small semicircle at intermediate frequency and a big arc at low frequency. The incomplete arc is an indication of very large impedance element. The intercept from the arc is assigned to grain boundary resistance substantiated by the capacitance value observed for it. This grain boundary resistance value is much lower as compared to ZBCM varistor. This is because in the polycrystalline ceramics such lowering of grain boundary resistance has been explained on the basis of stabilization (grain boundary) effect [41]. In other words, the grain boundaries are not

continuous but are discrete. As the temperature is further increased, this low temperature grain boundary semicircle superimposes with low frequency arc and shows a capacitance of  $\approx$  nF/cm, indicating the origin of this dispersion at the intergranular phase. This impedance is so high that it could not be determined even at high temperatures. In the above formulation of ZBCM-10 MgO varistor (grain boundary interface) is represented by a capacitor, which is shunted by a parallel resistor ( $R_{gb}$ ) to account for the leakage current and is connected with another resistor ( $R_{gi}$ ) in series to account for the relaxation time. In this case, there are only two intercepts in the analysis of the electrical behaviour of the material. They are labeled as  $R_{ZnO}$  (ZnO grain resistance) and parallel resistance  $R_{gb}$ . These are obtained by extrapolating the  $z'-z''$  plot towards very high and very low frequencies. The electrical response is described by a series combination of the network chain of RC elements as shown in Fig.4.3(b). The similar behaviour has been observed for Mn-Zn ferrites and well matches with the model proposed by Cheng [42]. The lumped/immittance parameter values for this equivalent circuit are summarised in Table-4.2.

The variation in the electrical equivalent circuit elements [Fig.4.3(a) and Fig.4.3(b)] operating at different time scales, can be easily understood in terms of the changes in the ceramic microstructure. After the addition of 10 mol% MgO it was noticed that (i) the grain growth of

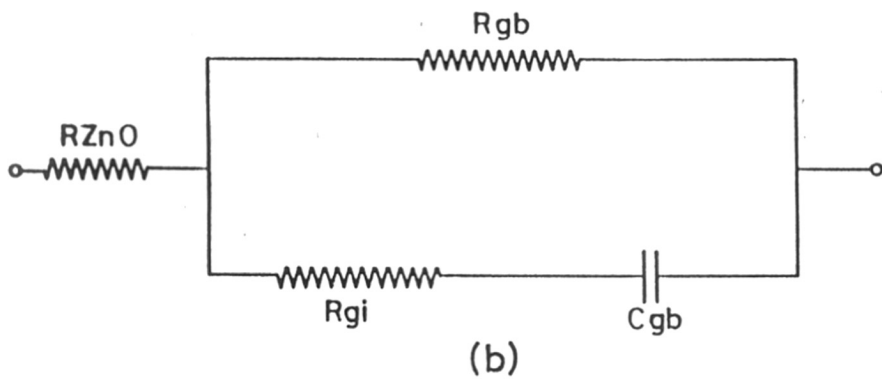
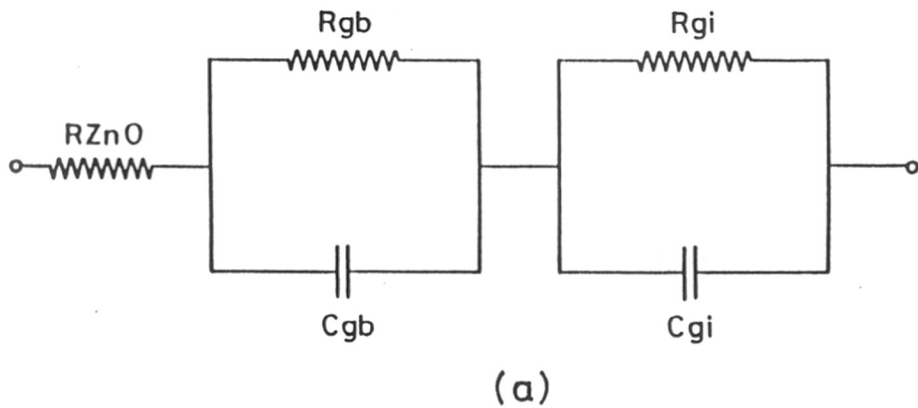


Fig. 4.3 Electrical equivalent circuit for (a) ZBCM and (b) ZBCM-10 MgO varistors.

**Table-4.2:** Immittance Parameters for ZBCM-10MgO varistor

Temp. °C	$R_{ZnO}$ Ohm	$R_{gb}$ X $10^3$	$C_{gb}$ X nF/cm	$R_{gi}$ X $10^5$ ohm	$C_{gi}$ X nF/cm
70	80	1.47	0.30	-	-
100	80	1.00	1.26	-	-
160	50	-	-	6.08	0.09
190	40	-	-	3.16	0.08
250	33	-	-	1.31	0.94

the dense compact of conducting grain is inhibited and; (ii) the number of barriers per unit thickness increased in the sintered compacts [32,43]. Blatter and Greuter [44,45] have carried out a self consistent study of the static and dynamic properties of carrier transport over double Schottky type potential barriers forming at a grain boundaries. In addition, the transport of the majority carriers through an electrically active grain boundary is treated on the basis of the model of electrons trapped at the interface and screened by ionised shallow and deep bulk defects within the two depletion regions. Since there is a clear difference of these defects between ZBCM and ZBCM-10MgO varistor systems, it is therefore expected that the electrical response in the frequency range 1 Hz - 10 MHz will be significantly different. Using their formalism, the



total current transport across the grain boundary is completely governed by the bias, temperature and time dependence of barrier height and is written as

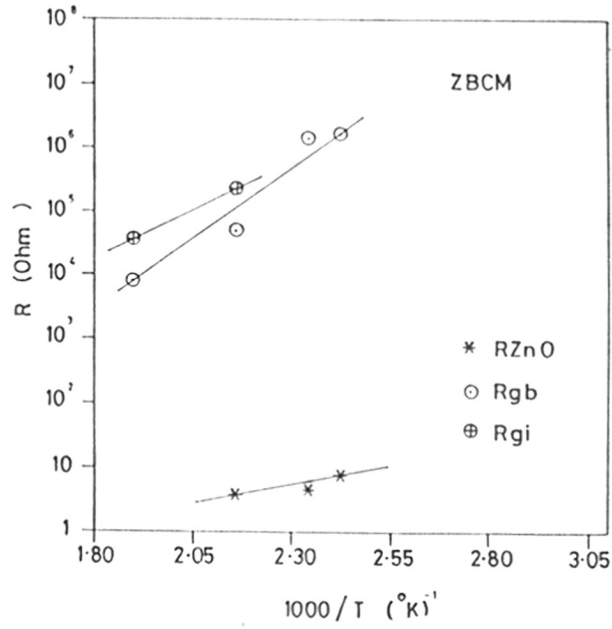
$$j = j_{dc} + j_{ac}$$

where  $j_{ac} = \sigma(V, w, T) \cdot \tilde{V} e^{i\omega t}$ ,  $e\tilde{V} \ll KT$  is exponentially controlled by the time-dependent barrier height  $\Phi_b$  given by

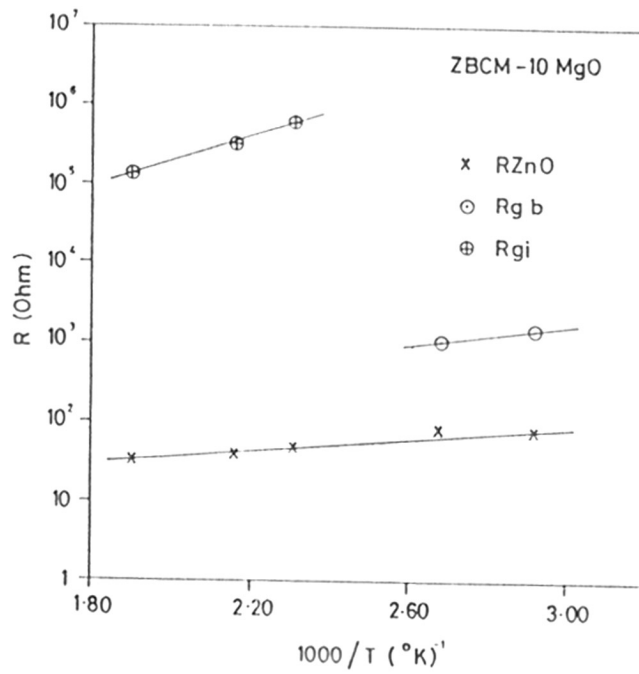
$$\Phi_b(V, w, T) = \Phi_{b0} - \Phi_b \exp(i\omega t)$$

and hence responds very sensitively to any changes in the interface and bulk screening charges. It is also known that the component  $j_{ac}$  is increasingly dominated by the modulation of the total interface charge which results into the complex components of conductivity ( $\sigma$ ). In fact, our observation from the impedance plots of these two varistor compositions agrees qualitatively with the dynamic grain boundary property model proposed by Blatter and Greuter [46].

In view of this changed functional and electrical microstructure, temperature dependence of lumped parameters arising from the bulk, grain boundary and grain interface components were carried out. Fig.4.4(a)-4.4(b) show Arrhenius plots for the temperature dependence of these elements at different temperature (25-250°C). In all the cases, the composition shows a semiconducting behaviour and the resistance is expressed by equation,



(a)



(b)

Fig. 4.4 Arrhenius plot for (a) ZBCM and (b) ZBCM-10 MgO varistors.

$$R = R_0 \cdot \exp \frac{E_a}{KT}$$

where,  $R_0$  - the resistance for  $T \rightarrow \infty$

$E_a$  - the activation energy of the conduction process

$K$  - the Boltzmann constant

$T$  - the absolute temperature.

The activation energies of the electrical conduction across the resistive elements ( $R_{ZnO}$ ,  $R_{gb}$  and  $R_{gi}$ ) were calculated from the different slopes of the Arrhenius plots ( $R$  versus  $1000/T$ ) and are summarised in Table-4.3.

**Table-4.3: Activation Energies Across the Network Elements ( $R_{ZnO}$ ,  $R_{gb}$ ,  $R_{gi}$ ) for ZBCM and ZBCM-10MgO Varistors**

Composition	ZBCM	ZBCM-10MgO
Components	$E_a$ (eV)	$E_a$ (eV)
$R_{ZnO}$	0.10	0.11
$R_{gb}$	0.88	0.14
$R_{gi}$	0.61	0.34

These activation energies have shown considerable difference e.g., 0.10 eV, 0.88 eV and 0.61 eV for ZBCM and 0.11 eV, 0.14 eV and 0.34 eV for ZBCM-10MgO varistors. The noticeable feature is the appreciable reduction in the

activation energies related to the lumped parameter (Network elements)  $R_{gb}$  and  $R_{gi}$ . This is also expected on the basis of the model proposed by Greuter and Blatter[46]. The lowering of activation energies across the  $R_{gb}$  and  $R_{gi}$  components in case of ZBCM-10MgO varistor from 0.88 eV to 0.14 eV and 0.61 eV to 0.34 eV is due to the improved electrical microstructure i.e. the width of the grain boundary is relatively reduced and at the same time the number of grain boundaries, interlinking grain boundaries have considerably increased, which affects indirectly the interfacial charge transport. This agrees with the electronic grain/conduction model proposed by Burton [47]. This clearly indicates that there is considerable difference in the conductivities across each element in case of these varistor systems. Similar values of activation energies have been reported in the literature on the ZnO varistors and other polycrystalline electroceramics [48-53].

In conclusion, the sensitive microstructural changes (on electrical element) taking place due to the doping of 10 mol% MgO and its subsequent controlled processing is directly observed in the complex impedance spectra.

## References

1. Impedance Spectroscopy (edited by J.R. Macdonald), John Wiley and Sons, NY (1987).
2. J.R. Macdonald, J. Chem. Phys. 61, (1974) 3977.
3. J.E. Bauerle, J. Phys. Chem. Solids 30, (1969) 2657.
4. A.D. Franklin, J. Am. Ceram. Soc. 58, (1975) 465.
5. A.K. Jonscher, Dielectric Relaxations in Solids, Chelsea Dielectric Press, London, (1983) pp.63-112.
6. A. Hooper, Solid State Batteries (edited by C.A.C. Sequeira and A. Hooper) pp.260-281, Martinus Nijhoff Publishers, Boston, U.S.A. (1985).
7. B.E. Mellander and A.L. Lunden, Solid State Materials for Batteries (edited by B.V.R. Choudri and S. Radhakrishnan) pp.161-168, World Scientific Publications, Singapore (1986).
8. B.B. Ghatge, Advances in Ceramics, Vol.I: Grain Boundary Phenomena in Electronics Ceramics (edited by L.M. Levinson), pp.447-493, Am. Ceram. Soc. Columbus, Ohio, U.S.A. (1981).
9. R.C. Sundal Jr., B.B. Ghatge, R.J. Holmes and C.E. Pass, Advances in Ceramics, Vol.I: Grain Boundary Phenomena in Electronic Ceramics (edited by L.M. Levinson), pp.502-511, Am. Ceram. Soc. Columbus, Ohio, U.S.A. (1981).
10. J.T.S. Irvine, A. Huanosta, R. Valenzuela and A.R. West, J. Am. Ceram. Soc. 73, (1990) 129.
11. S. Jankowski, J. Am. Ceram. Soc. 71, (1988) C-176.

12. B.M. Kulwicki, *Advances in Ceramics, Vol.I: Grain Boundary Phenomena in Electronic Ceramics* (edited by L.M. Levinson), pp.138-154, Am. Ceram. Soc. Columbus, Ohio, U.S.A. (1981).
13. T.Y. Teseng and S.H. Wang, *Mat. Letters* 9, (1990) 164.
14. P. Blanchart, J. Francois and P. Abelard, *J. Am. Ceram. Soc.* 75, (1992) 1068.
15. G. Godman, *Advances in Ceramics, Vol.I: Grain Boundary Phenomena in Electronic Ceramics*, pp.215-231, Am. Ceram. Soc. Columbus, Ohio, U.S.A. (1981).
16. W.R. Fahrner, D. Baunig, P. Ostrop and S. Ruhl, *J. Appl. Phys.* 71, (1992) 3381.
17. W.R. Fahrner, D. Baunig, P. Ostrop and S. Ruhl, *J. Appl. Phys.* 71, (1992) 3388.
18. *Grain boundaries in semiconductor, Vol.5;* (edited by H.J. Leamy, G.E. Pike and C.H. Seager), North Holland, NY, U.S.A. (1982).
19. G. Hohenberger and G. Tomandi, Ref. 167(b) of Chapter-1.
20. D.K. Kharat, G.S. Dharni and S.K. Date, *Solid State Comm.* 84, (1992) 375.
21. D.K. Kharat, G.S. Dharni, S.K. Date, A.R. Kulkarni and R.D.A. Paulmer, *Solid State Comm.* 85, (1993) 671.
22. T.K. Gupta, Ref. 62 of Chapter-1.
23. M. Matsuoka, Ref. 113 of Chapter-1.
24. L.M. Levinson and H.R. Philipp, Ref. 81 of Chapter-1.
25. K. Eda, Ref. 83 of Chapter-1.
26. *Ceramic Transactions, Vol.3: Advances in Varistor Technology* (edited by L.M. Levinson), Am. Ceram. Soc., U.S.A. (1989).

27. K.A. Abdullah, A. Bui and A. Loubire, J. Appl. Phys. 69, (1991) 4046.
28. M.A. Alim and M.A. Seitz, J. Am. Ceram. Soc. 71, (1988) C-246.
29. M.A. Alim, M.A. Seitz and R.W. Hirthe, J. Appl. Phys. 63, (1988) 2337.
30. Y. Shim and J.F. Cordaro, J. Appl. Phys. 64, (1988) 3994.
31. M.A. Alim, J. Am. Ceram. Soc. 72, (1989) 28.
32. U. Schwing and B. Hoffmann, J. Appl. Phys. 57, (1985) 5372.
33. B.A. Boukamp, Equivalent Circuit Software, Twente University, Netherlands.
34. M.A. Alim, M.A. Seitz and R.W. Hirthe, J. Am. Ceram. Soc. 71, (1988) C-55.
35. T.K. Gupta, Ref. 85 of Chapter-1.
36. A. Smith, J.F. Baumard, P. Abelard and M.F. Denanol, J. Appl. Phys. 65, (1989) 5119.
37. L.M. Levinson and H.R. Philipp, J. Appl. Phys. 47, (1976) 1117.
38. M. Matsura and H. Yamaoki, Jpn. J. Appl. Phys. 16, (1977) 2161.
39. B.S. Chiou and F.W. Hih, Br.Ceram. Trans. J. 85,(1986) 118.
40. M. Kim, J. Koo, M. Oh and C. Kim, J. KIEE, 3, (1990) 20.
41. S.P.S. Badwal, Proceedings of the International Seminar on Solid State Ionic Devices (edited by B.V.R. Chowdari and S. Radhakrishnan), pp. 165-189, World Scientific NJ, USA (1988).
42. H.F. Cheng, J. Appl. Phys. 56, (1984) 1831.

43. A. Smith, G. Gasgnier and P. Abelard, J. Am. Ceram. Soc. 73, (1990) 1098.
44. G. Blatter and F. Greuter, Phys. Rev. B33, (1986) 3952.
45. G. Blatter and F. Greuter, Phys. Rev. B34, (1986) 8555.
46. F. Greuter and G. Blatter, Polycrystalline Semiconductors (edited by J.H. Werner, H.J. Moller and H.P. Strunk, pp. 302-314, Springer-Verlag Berlin, Heidelberg (1989).
47. L.C. Burton, Mat. Res. Soc. Symp. Proc. Vol. 60, pp. 179-189, Material Res. Society, USA (1986).
48. M.A. Kleitz, A. Bernard, E. Fernandez and E. Schouler, Advances in Ceramics Vol.3: Science and Technology of Zirconia (edited by A.H. Hener and L.W. Hobbe) pp.311-336, Am. Ceram. Soc. U.S.A. (1981).
49. F. Greuter, G. Blatter, M. Rossinelli and F. Schmuckle, Defects in Semiconductors, Material Science Forum Vol.10-12 (edited by H.J. Von Bardeleben) pp. 235-240, Trans. Tech. Publications Ltd., Switzerland (1986).
50. L.C. Sletson, M.E. Potter and M.A. Alim, J. Am. Ceram. Soc. 71, (1988) 909.
51. R.F. Ramirez, A. Huanosta, E. Amano, R. Valenzuela and A.R. West, Ferroelectrics, 99, (1989) 195.
52. E.R. Leite, J.A. Varela and E. Longo, J. Appl. Phys., 72, (1992) 147.
53. A.R. Ferreira, C.S. Furtado and J.M. Perdigao, J. Am. Ceram. Soc., 75, (1992) 1708.



## SUMMARY & CONCLUSIONS

Zinc oxide (ZnO) based ceramic sensor belongs to a new class of electronic materials, based on grain boundary properties. Its primary function is to sense and limit transient voltage surges and to do so repeatedly without being destroyed. In particular, sintered zinc oxide ceramics containing a variety of selective additives (dopants such as bismuth oxide and other transition metal oxides) have shown excellent nonlinear current-voltage (I-V) characteristics. These unique electrical properties make them suitable for use as surge arrestors and voltage limitors in electrical/electronic devices. It has been reported from the earlier studies that zinc oxide (ZnO) varistor consists of electrically conducting zinc oxide grains surrounded by electrically insulating barriers at the grain boundaries. These barriers are formed by the addition of bismuth oxide and other transition metal oxides so as to improve the performance properties. The electrical properties of these devices are determined by their detailed "functional microstructure", which develops during the synthesis. Two important performance parameters are, (i) nonlinear coefficient ( $\alpha$ ) and; (ii) breakdown electric field ( $E_b$ ), generally specified at a current density of  $1\text{mA}/\text{cm}^2$ . The value of breakdown electric field can be achieved by either optimising the varistor thickness and the grain size related microstructure of the dense compacts. At present ZnO varistors are dominating large segment of surge protection market, including consumer, military electronics, power transmission and distribution, data processing, communication and variety of industrial systems. The increased

application range of ZnO varistors is reflected by high level of world research and development activities. The intense interest in this electronic ceramics is an indication of the growing range of applications and importance of ZnO varistor technology. It appears that usages of the material will grow and the applications will broaden as the technology continues to mature.

The work incorporated in the thesis is an attempt to develop simple varistor comprising of 97 mol% ZnO and 1 mol% each of  $\text{Bi}_2\text{O}_3$ ,  $\text{Co}_2\text{O}_3$  and  $\text{MnO}_2$ , their synthesis and characterizations etc. Series of experiments were carried out to modify the basic varistor composition with 10 mol% MgO as a grain growth inhibitor. These varistor systems were abbreviated as ZBCM and ZBCM-10MgO. After the confirmation of the varistor properties, MgO concentration was changed from 5, 15 and 20 mol% to see the effect of MgO on the performance properties of the modified varistors. These varistor systems were abbreviated as ZBCM-5MgO, ZBCM-15MgO and ZBCM-20MgO respectively. The varistors were synthesized using conventional solid state (chemical) ceramic route. From the very extensive experimental work done, and its subsequent analysis, important processing parameters such as chemical composition, particle size and its distribution, binder removal and its burnout effect, sintering temperature - time relationship, electrical contents have been meticulously identified and optimised. During the synthesis, active powders were characterized at various stages such as after mixing, pressing and sintering etc.

The current-voltage (I-V) characteristics of these varistor systems were measured at room temperature as a function of sintering temperature and data was plotted in a log-log scale. The values of nonlinearity coefficient and breakdown electric field were calculated using the empirical equation,  $J = (E/C)^\alpha$  where,  $J$  = current density,  $E$  = electric field,  $C$  = constant and  $\alpha$  = nonlinearity coefficient.

It was seen from the results of  $E_b$  and  $\alpha$  that a varistor system modified with 10 mol% MgO gives the higher breakdown electric field with almost same nonlinear coefficient (e.g.  $E_b(\text{ZBCM}) \approx 282$  V/mm,  $\alpha(\text{ZBCM}) \approx 36$  and  $E_b(\text{ZBCM-10MgO}) \approx 1000$  V/mm,  $\alpha(\text{ZBCM-10MgO}) \approx 29$ ) for the pellets sintered at 1050°C/1hr. The improvement in  $E_b$  and  $\alpha$  are most likely due to the improvement in the functional microstructure achieved by controlling the processing parameters. It was predicted that higher values can be obtained by increasing the number of grain boundaries and reducing the grain size. There exist two possibilities for the improvement in the microstructure (i) due to addition of MgO, the grain growth of the dense compacts of highly conducting grains is inhibited which helps in increasing the number of barriers per unit thickness in the sintered compacts and; (ii) the composition may correspond to two phase system containing zincite and a mixture of ZnO and magnesia (ZnO-MgO) which is highly insulating. To understand the relative contributions from these two pathways, extensive physico-chemical characterization of the sintered compacts/powders of ZBCM and ZBCM-10MgO varistor systems were carried out using

density, XRD, SEM, XPS and AC impedance analysis techniques.

Density analysis of these systems have shown that density increases with the increase of sintering temperature over the temperature 900-1300°C and it is maximum when sintered at 1050°C. Thus 1050°C is an optimum temperature at which varistor pellets have shown the high degree of compactness and high values of  $\alpha$ . Beyond 1050°C, between 1100-1300°C the density decreases with increase of sintering temperature due to evaporation of  $\text{Bi}_2\text{O}_3$  and the weight loss of the pellets. At these sintering temperatures, pellets have shown poor I-V performance characteristics.

X-ray diffractogram studies of these systems have shown the similar behaviour e.g. in both the cases, all ZnO characteristic lines are present in physical mixture and powders sintered between 900-1300°C. X-ray diffractograms of physical mixture have shown the visible characteristic lines of  $\alpha\text{-Bi}_2\text{O}_3$  (monoclinic) and  $\gamma\text{-Bi}_2\text{O}_3$  when sintered at 900°C. This shows that  $\text{Bi}_2\text{O}_3$  phase transformation has taken place. In both the X-ray diffractograms,  $\gamma\text{-Bi}_2\text{O}_3$  characteristic lines are visible upto 1050°C and thereafter they start disappearing slowly at higher sintering temperatures (1150-1300°C). This indicates that the evaporation of  $\text{Bi}_2\text{O}_3$  is taking place at higher sintering temperatures. This supports the earlier observation about the decrease in density and poor (I-V) performance at higher sintering temperatures. However, there is no indication of any separate (mixed phase) characteristic lines of MgO ( $2\theta \approx 42.9$ ,

63.3) in the powder X-ray diffractogram of ZBCM-10MgO varistor, which shows that MgO forms a solid solution (ZnO-MgO) with ZnO during sintering. In other words, all characteristic lines of these two phase system (ZnO and ZnO-MgO) are overlapping with each other. We did not attempt to resolve these superimposed pattern to derive finite changes in the lattice parameters of ZnO-MgO solid solutions. This confirms the postulates that the formation of two phase system within the detection limit of powder XRD data.

SEM photomicrographs of these systems have shown that the grain size increases with the increase of sintering temperature. However, in case of ZBCM varistor system the grain size is very high, grains are not closely packed and uniformly distributed. The average grain size for the pellet sintered at 900° is  $\approx 2 \mu\text{m}$  and it increased to  $\approx 47.5 \mu\text{m}$  when sintered at 1300°C. However, in case of ZBCM-10MgO varistor system the average grain size is small, grains are closely packed and uniformly distributed. The average grain size for the pellet sintered at 900°C is  $\approx 1.5 \mu\text{m}$  and it increased to  $\approx 20.0 \mu\text{m}$  when sintered at 1300°C. The microstructure of these varistors shows that ZnO grains are isolated from each other by a continuous network of  $\text{Bi}_2\text{O}_3$  segregation/intergranular layer with some voids and pores.

The pellets of ZBCM-10MgO varistor sintered at 1050°C have shown the difference in microstructure as compared to ZBCM varistor. In case of ZBCM, average grain size is  $\approx 5.3 \mu\text{m}$  and grains are not uniformly distributed. However, in ZBCM-10MgO, average grain size is  $\approx 4 \mu\text{m}$  and grains are uniformly

distributed and closely packed. This increases the number of grains and grain boundaries in a modified varistors with 10mol% MgO, showing that MgO acted as a grain growth inhibitor. Consequently, all these changes in microstructure resulted in different current carrying pathways with different breakdown voltage for each pathways. As the number of current carrying pathways are increased in ZBCM-10MgO varistor microstructure, this leads to the increase of breakdown electric field and the performance, as evident from the I-V, XRD and density results.

The XPS spectra of these varistors have shown that the  $\text{Bi}_2\text{O}_3$  migrates with the increase in sintering temperature from the ZnO grain surface. However, XPS spectra of ZBCM-10MgO varistor system do not show any visible intensity peaks of MgO states. This is mainly because MgO is not migrating on the ZnO grain surface but dissolves during liquid phase sintering and forms ZnO-MgO solid solution with ZnO as predicted from XRD studies.

To find the role of breakdown electric field per barrier, electric field versus the reciprocal of grain size was plotted. It is found that breakdown voltage per barrier for ZBCM is  $V_g(\text{ZBCM}) \approx 1.16$  V/barrier and for ZBCM-10MgO,  $V_g(\text{ZBCM-10MgO}) \approx 3.0$  V/barrier. This shows that the breakdown voltage per barrier in the modified varistor (with 10 mol% MgO) has increased almost three times than the basic ZBCM varistor system.

The above results show that addition of 10 mol% MgO have improved the functional microstructure under controlled

processing conditions. However, XRD and XPS studies on this composition have not shown the presence of any other additional complex (bulk) phases formed during sintering. To resolve this dilemma and to differentiate between varying contributions from grains, grain boundaries/intergranular layers and electrode interfaces, AC impedance spectroscopy was used as an important tool due to high sensitivity microstructural changes. The technique is used successfully over the frequency range of 1Hz-10MHz in the temperature range of 25-250°C. From the complex impedance plots the performance was modeled in a electrical equivalent circuit which leads to the different network elements. To understand the electrical conduction across the grain, grain boundaries and grain interfaces in terms of RC network elements, activation energies associated with these processes were calculated from the Arrhenious plots. The values of activation energies across the network elements  $R_{ZnO}$ ,  $R_{gb}$  and  $R_{gi}$  were found in the range of 0.10, 0.88 and 0.61 eV for ZBCM and 0.11, 0.14 and 0.34 eV for ZBCM-10MgO varistors. The noticeable feature is the appreciable reduction in the activation energies related to the lumped parameters  $R_{gb}$  and  $R_{gi}$  for ZBCM-10MgO varistor. It is confirmed on the basis of the conduction model proposed by Greuter and Blatter that lowering of activation energies across  $R_{gb}$  and  $R_{gi}$  components in case of ZBCM-10MgO varistor from 0.88 eV to 0.14 eV and 0.61 eV to 0.34 eV are due to the improved electrical microstructure i.e., the width of the grain boundary is relatively reduced and at the same time, the number of grain boundaries interlinking grain



boundaries have considerably increased which affects indirectly the interfacial charge transport. This is again proved on the basis of grain/conduction model proposed by Burton. All these changes in the microstructure lead to the improvement in the performance parameters of ZBCM-10MgO varistor in comparison with ZBCM varistor.

It is hoped that in the coming years the research efforts in this area are likely to have a path breaking impacts in the design and development of better devices produced by controlling structure-property correlations, so as to make them most cost effective and challenging in the field of SMART sensor technology.

### List of Publications

1. ZnO varistors: Synthesis, characterization and applications, D.K. Kharat, G.S. Dhami, S.R. Sainkar and S.K. Date, J. Sci. Ind. Res. 50, 596 (1991).
2. Improvement in the performance parameters of ZnO based varistors with 10 mol% MgO, D.K. Kharat, G.S. Dhami and S.K. Date, Sol. State Commn. 84(3), 375 (1992).
3. AC impedance spectroscopic characterization of 10 mol% MgO doped ZnO varistors, D.K. Kharat, G.S. Dhami, S.K. Date, A.R. Kulkarni and R.D.A. Paulamer, Sol. State Commn. 85(8), 671 (1993).
4. Electrical characterization of 10 mol% MgO doped ZnO based varistors by impedance spectroscopy, D.K. Kharat, G.S. Dhami, S.K. Date, A.R. Kulkarni and R.D.A. Paulamar (Communicated).

## ACKNOWLEDGEMENT

I am deeply indebted to Dr. S.K. Date, Scientist 'F', Deputy Director, National Chemical Laboratory, Pune for suggesting this interesting research problem and for his inspiring guidance during the course of this investigation. I am fortunate, to have a guide like Dr. S.K. Date, who has induced in me an aptitude for research, analytical thinking and ambition to excel in this field. During the course of this investigation, I found in him a researcher who, through his own example, inspired me with devotion towards a common goal.

I am grateful to the Scientific Adviser to the Minister of Defence and D.G.R&D, Defence R&D Organisation (DRDO), Govt. of India, New Delhi and the Director, Armament R&D Estt., Pune for their kind permission to join Ph.D. research programme at NCL and to the Director, National Chemical Laboratory, Pune for his kind permission to work as a guest worker during the course of research work.

I express my sincere thanks to Shri G.S. Dhami, Joint Director, ARDE for illuminating discussions and encouragement during the course of this investigation.

Physico-chemical characterization was one of the important aspects of this investigation. The work would not have been completed without the active support from Shri M.V. Kuber (XRD), Dr.(Mrs.) A. Mitra (SEM), and Dr. S.R. Sainkar (XPS) from Special Instruments Lab. I am thankful to these researchers for

their friendly help and useful suggestions.

AC impedance measurement and analysis was the gray area in this investigation. Prof.(Dr.) Ajit Kulkarni of Material Science Center , I.I.T., Bombay, was kind enough to extend this facility. His generous hospitality and cooperation to carry out these measurements are invaluable for me. I am thankful to him and Mr. R.D.A. Paulamer for their friendly help.

Special thanks are due to Dr. H.S. Potdar, Dr. S.B. Deshpande, Mr. P.D. Godbole, Dr. C.E. Deshpande, Mrs. J.J. Shrotri, Dr.(Mrs.) S.D. Kulkarni and Mr. A.G. Bagul of Electronic Ceramic Group and Dr. V.P. Shiralkar and Dr. A.N. Kotasthane of Catalysis Group for their help, advice and suggestions during the present investigation.

I would like to express my thanks to Shri S.G. Tatake, Dy. Director, ARDE for continuous encouragements.

I am thankful to my colleagues of APT Group and Mr. M.P.S. Nambooderi of PZT-PP Group for their cooperation during the work.

Last but not at all the least, let me thank my wife Madhavi, who has not only offered all possible help but has also shared my feelings and aspirations and has induced in me the patience and courage to face all odds which are inevitable in a research career. Thanks are also due to my in laws and parents for their help and support.

Timely completion of any project also requires the cooperative efforts of the people outside the laboratory. I thank administrative and library staff of ARDE, NCL and Poona University for their cooperation during the work.

I would like to record my appreciation for the reprographic supports from Mr. C.M. Lonkar, Mr. A.M. Rokade and Mr. A.K. Gangopadhyay for the completion of the manuscript.

I am grateful to the Director, NCL for allowing me to submit this work in the form of a Ph.D. thesis to the University of Poona.

I trust that I have made due and full acknowledgement and apologise for any accidental omissions.

  
26.7.93  
(D.K. Kharat)